TUMOR GLYCOLYSIS IS A MECHANISM OF IMMUNE EXCLUSION FROM SOLID TUMORS

By

Ivan Jose Cohen

A Dissertation presented to the

Faculty of the Louis V. Gerstner, Jr.

Graduate School of Biomedical Sciences

Memorial Sloan Kettering Cancer Center

in partial fulfillment of the requirements for the

degree of Doctor of Philosophy

New York, NY

August 2019

_____ _____

Ronald G. Blasberg, MD Date
Dissertation Mentor

DEDICATION

To my family, for their continuous support.

ABSTRACT

Immune infiltration has been recognized as critical for long-term survival dating back to the 1920's. More recently, given the advent of immunotherapy and how it is revolutionizing cancer care across disciplines, a mechanistic understanding of immune infiltration and exclusion is of paramount importance. This is especially so since patients with immune-infiltrated tumors tend to have much better responses to immune checkpoint blockade with anti-CTLA4 or anti-PD1 therapy. An abundance of literature shows that lactic acid is highly immune suppressive in tumors and affects multiple immune cell types, including T-cells, NK cells, MDSC's, dendritic cells and macrophages. In this work, we tested the hypothesis that increased tumor glycolysis may contribute to exclusion of immune cells from solid tumors, due to the increased accumulation of lactic acid in the extracellular milieu. We tested this hypothesis - first by *in-vitro* and *in-vivo* approaches involving animal models of cancer, and then by a bioinformatics and *in-situ* approach in multiple human solid tumor types. We found, both *in-vitro* and *in-vivo*, that increased tumor glycolysis leads to increased accumulation of lactic acid and decreased immune function. We further found that increased expression of tumor glycolysis markers was associated with decreased immune infiltration in many solid tumor types.

ACKNOWLEDGEMENTS

I would like to thank my mentor, Dr. Ronald Blasberg, and members of the Blasberg laboratory for their help and support in this work. I would also like to extend my great appreciation to the many incredible scientists with whom I've collaborated during my thesis, and without him this work wouldn't have been possible.

TABLE OF CONTENTS

LIST OF TABLES

LIST OF FIGURES

LIST OF ABBREVIATIONS

CTLs: Cytotoxic lymphocytes
APCs: Antigen-presenting cells
MHC: Major histocompatibility complex
TCR: T-cell receptor
NK: Natural killer cells
DC: Dendritic cells
MDSC: Myeloid-derived suppressor cells
TAM: Tumor-associated macrophages
ICB: Immune checkpoint blockade
OS: Overall survival
RFS: Recurrence-free survival
ORR: Objective response rate
CR: Complete response
PR: Partial response
SD: Stable disease
PD: Progressive disease
MSI: Microsatellite instability
TIL: Tumor-infiltrating lymphocyte
ER: Estrogen receptor
PR: Progesterone receptor
HR: Hormone receptor; Hazard ratio
pCR: Pathological complete response
TNBC: Triple-negative breast cancer
HER2: Human epidermal growth factor 2
NAC: Neo-adjuvant chemotherapy
FDA: Food and drug administration
IHC: Immunohistochemistry
RT-PCR: Real-time polymerase chain reaction
RNA: Ribonucleic acid
DNA: Deoxy-ribonucleic acid
mRNA: Messenger RNA
ATP: Adenosine tri-phosphate
TME: Tumor microenvironment
FDG-PET: Fluoro-deoxy-glucose positron emission tomography
HATs: Histone acetyltransferases
DMEM: Dulbecco’s modified eagle medium
FCS: Fetal calf serum
CFSE: carboxyfluorescein succinimidyl ester
shRNA: small-hairpin RNA
FACS: Fluorescence-activated cell sorting
LDHA: Lactate dehydrogenase A
NCBI: National center for biotechnology information
gRNA/sgRNA: guide RNA/small guide RNA
2-DG: 2-deoxy-glucose

FCCP: carbonyl cyanide p-trifluoromethoxy-phenylhydrazone
glycoPER: glycolytic proton efflux rate
NMR: Nuclear magnetic resonance
PSMA: Prostate-specific membrane antigen
CAR T-cell: Chimeric antigen-receptor T-cell
BLI: Bioluminescence imaging
GSEA: Gene set enrichment analysis
MRI: Magnetic resonance imaging
ECAR: Extracellular acidification rate
OCR: Oxygen consumption rate
DMSO: Dimethyl sulfoxide
GFP: Green fluorescent protein
RFP: Red fluorescent protein
CBR Luc: Click beetle red luciferase
H-Score: Histological score
TCGA: The cancer genome atlas
CPTAC: Clinical proteomic tumor analysis consortium
SUV: Standardized uptake value
BLCA: Bladder cancer
BRCA: Breast cancer
COAD: Colon adenocarcinoma
CESC: Cervical squamous carcinoma
ESCA: Esophageal carcinoma
HNSC: Head and neck cancer
LIHC: Liver hepatocellular carcinoma
LUAD: Lung adenocarcinoma
LUSC: Lung squamous carcinoma
RCC: Renal clear cell carcinoma
READ: Rectal adenocarcinoma
SKCM: Skin cutaneous melanoma
STAD: Stomach adenocarcinoma

CHAPTER 1

INTRODUCTION

1.1 Basic mechanisms of a successful anti-tumor immune response

Immunotherapy has dramatically expanded patient's lives in melanoma (1), and has given hope for a new generation of patients to dramatically improve survival without going through the side effects of traditional chemotherapy. A successful anti-tumor immune response involves many components of the immune system. The adaptive immune system is highly complex and relies on educating cytotoxic lymphocytes (CTLs) to recognize modified or mutated antigens and eliminating malignant cells that express them. This process begins with Antigen Presenting Cells (APCs; typically dendritic cells or macrophages) which can internalize dead tumor cells, digest them into small peptides and present these at the cell surface in either Class II Major Histocompatibilty Complex (MHC-II) ('classical' antigen presentation), or Class I MHC ('cross-priming') (2, 3). T-cells continuously interact with APCs (typically within the spleen or peripheral lymph nodes) and scan peptides bound to MHC-I or MHC-II in a highly sequence-specific manner. Successful engagement of a TCR with its specific/cognate peptide-MHC complex on an APC leads to a biochemical signaling cascade that culminates in T-cells undergoing an activation/differentiation and proliferation/expansion program. This leads to a large number of antigen-specific activated CD4+ Helper T (Th) cells and CD8+ Cytotoxic T cells primed for effector functions that survey virtually all cells within the organism for expression of the specific antigen.

All nucleated cells process their intracellular protein contents through the proteasome system, and the MHC-I complex presents the degraded peptide fragments (epitopes) on the cell surface. In this manner, all nucleated cells in the human body present their intracellular contents to surveying lymphocytes. Thus, if a circulating activated T-cell recognizes an antigen within a peptide-MHC-I complex, it will either kill the target cell or produce inflammatory cytokines, depending on the type of lymphocyte (4). After recognizing an antigen on a malignant cell, CD4+ T Helper cells can secrete pro-inflammatory cytokines to recruit other immune cell types and mount an immune response, and CD8+ cytotoxic T cells can directly kill tumor cells by secretion of cytotoxic molecules such as Perforin and Granzymes, which leads to apoptosis of the target cell.

Thus, a successful anti-tumor immune response requires several key steps: (i) capturing of tumor antigens by APCs; (ii) presentation of tumor antigens to lymphocytes (typically in spleen and/or tumor-draining lymph nodes); (iii) activation and expansion of CD4+ and/or CD8+ lymphocytes; (iv) direct cell-cell contacts between activated lymphocytes and tumor cells (at primary or metastatic tumor sites); (v) production of inflammatory cytokines (CD4+) and killing of tumor cells (CD8+); as well as other mechanisms involving B, NK cells and macrophages, reviewed elsewhere (5-7).

1.2 Immunotherapy in the clinic

Immunotherapy is revolutionizing cancer care. While dramatic benefits have been observed in hematologic cancers, progress has been slower in solid

tumors. Immune checkpoint blockade (ICB) with PD1/PDL1-, or CTLA4-blocking antibodies has shown to be effective in many cancers, whether as a monotherapy or as combination therapy with multiple checkpoint inhibitors or with standard chemotherapies. As a monotherapy, some of the best responses were seen in high-mutation burden tumors. Merkel cell carcinoma, which is characterized by a high mutation burden or Polyoma virus infection, showed a remarkable 56% objective response rate (ORR) and a 64% 3-year overall survival (OS) rate, compared to an historical 10% 3-year OS (8). In a phase II trial of 86 patients with microsatellite instability-high (MSI-h) tumors of various histologies, pembrolizumab resulted in a 53% ORR and 21% complete response (CR) (9). The 1 year overall survival (OS) rate was 72%, compared with 24% in a similar cohort of patients in 2013 treated with placebo or an experimental drug, regorafenib (10). In melanoma and non-small cell lung cancer (NSCLC), the objective response rates following pembrolizumab therapy were reported to be 45% and 36%, respectively (11, 12). Combination of anti-PD1 and anti-CTLA4 therapies are showing even higher response rates and durability of responses (13, 14). A combination of ipilimumab (anti-CTLA4) and nivolumab (anti-PD1) in Stage III/IV melanoma showed a 58% ORR and a 53% 4-year overall survival rate (15). This is a great difference compared to the ~15% 2-year OS reported for chemotherapy in 2011 (16), or the 17% 4-year OS reported with vemurafenib (BRAF V600E inhibitor) in 2012 (17). Immune checkpoint blockade is also generating improved responses in combination with standard chemotherapies, most notably in lung and breast cancer. Multiple studies, including patients with

metastatic non-small cell lung cancer (NSCLC) and SCLC, showed significant improvements in PFS and OS in the ICB + chemotherapy combination, with one study with long-term survival data showing a 63% vs. 44% overall survival rate at 2 years in the pembrolizumab- vs. placebo-containing populations (18-21). It should be noted, however, that a large fraction of solid tumors do not respond to checkpoint or other immune-based therapies (Table 1).

1.3 Immune responses to tumor-associated antigens in breast cancer

The study of anti-tumor immune responses in breast cancer began in the early 1990's with the discovery that CTLs obtained from tumor-draining lymph nodes of breast cancer patients could specifically recognize and kill breast tumor cell lines in culture (but not normal breast epithelial cell lines). This response was mediated through the immune recognition of the glycoprotein Mucin (MUC-1). Although MUC-1 was expressed in both breast cancer and normal epithelial cell lines, this study showed that it was under-glycosylated in tumor cells, leading to the exposure of a hidden epitope that could be recognized by CTLs (22). Thus, a 'self' antigen was shown to be aberrantly expressed and modified to trigger an immune response. Later studies showed that very low levels of MUC-1-specific T-cells could be detected in peripheral blood and bone marrow of both breast cancer patients and healthy subjects, but with a significantly higher percentage of these T-cells in breast cancer patients (23, 24). Along similar lines, flow cytometric analysis of tumor cells and TILs obtained after surgical resection of breast tumors in 31 patients showed that the expression of MHC-I on tumor cells was strongly associated with infiltration of both CD4+ and CD8+ cells into the

tumors (25). Further, by studying the levels of MUC-1-specific IgG antibodies (which are typically secreted by effector B-cells) in the serum of non-metastatic breast cancer patients, two separate studies (a combined total of 442 patients) showed that increased

	n	ORR (%)	Drug
NSCLC	6632	34	P, N, At, D
Melanoma	4127	33.2	P, I, N, N+I
Urothelial	3432	19	P, N, At, Av, D
RCC	821	25	N, N+I
Head and Neck	724	16	P, N
Hepatocellular	262	20	N
Gastric	259	11.6	P
CRC	256	39	N, N+I
SCLC	216	23	N+I
Merkel Cell	153	41	P, Av
Cervical	98	13.3	P
Total	**16980**	**25**	

Table 1. FDA-approved immunotherapies.

Abbreviations: P = pembrolizumab. N = nivolumab. I = ipilimumab. At = Atezolizumab. D = durvalumab. Av = avelumab.

NSCLC: Non-small cell lung cancer
RCC: Renal cell carcinoma
CRC: Colorectal carcinoma
SCLC: Small-cell lung cancer

MUC-1-specific antibodies were significantly correlated with improved disease-free and overall survival (26, 27).

Similar to MUC-1, HER-2 was also found to be immunogenic, although its overexpression in tumor cells seems to be responsible for its immunogenicity rather than uncovering of hidden epitopes. In a study of 104 patients with variable expression of HER2 on primary tumors, HER2 expression was significantly correlated with both HER2-specific IgG antibodies in serum, as well as with HER2-specific T-cells in blood (28). Furthermore, in a study analyzing the sera of over 500 breast cancer patients, those with HER2-specific antibodies above the median had a significantly improved recurrence-free survival after surgery compared with patients with low antibody levels (29). These studies demonstrate that innate immunity develops in some patients with breast cancer and has an impact on the patient's clinical course.

1.4 Tumor Infiltrating Lymphocytes (TILs) in breast cancer

The above studies established that immune responses (B- and T-cell mediated) are sometimes successful in mounting an anti-tumor immune response. An important factor determining immune control of tumors is the ability of T lymphocytes to infiltrate tumors. The importance of TILs in breast cancer was noted as early as 1922, when lymphocytic infiltration was correlated with improved survival in a cohort of 218 breast cancer patients (30). More recent studies have confirmed these findings in other cancer types (31), including breast cancer. A study of over 1000 patients found that lymphocytic infiltration (as

measured by IHC staining of lymphocytes, as well as quantification of mRNA abundance of immune-related transcripts by RT-PCR), showed a clear and significant correlation between immune infiltration and pathologic complete response (pCR) to neoadjuvant chemotherapy (40% vs. 7% pCR in highly immune infiltrated tumor vs. tumors without immune infiltration) (32). This trend was also observed in a study of 180 patients, where high TIL scores were associated with a better pCR (34% pCR in TIL-high patients vs. 10% pCR in TIL-low patients). Interestingly, the difference in pCR between TIL high vs. low was only significant in Hormone Receptor (HR)-negative patients (TNBC or HER2+), but not HR+ patients (ER+ or PR+) (33). In a meta-analysis of 13 studies including 3,251 patients, Mao et. al., found that the presence of TILs in pre-treatment biopsies was associated with a better pCR rate; interestingly, there was an approximately 4-fold better pCR specifically in TNBC and HER2+, but not in HR+ patients (confirming the above observations) (34). Focusing specifically on ~500 patients with TNBC, Adams, et. al., found that the percentage of stromal TILs had a significant effect on overall survival, with the 10-year overall survival probability of ~90% for patients with the highest stromal TIL score vs. ~65% for those with no stromal TIL ($p = 0.02$) (35). Similar results were obtained in a 2013 study of 2,000 pre-treatment breast tumor samples, where the authors found that lymphocytic infiltration improved survival in TNBC, with a 5-year survival rate of 92% for patients with high TIL scores vs. 71% for those with low TIL scores.(36) Thus, a picture emerges in breast cancer where, despite being more aggressive, HR-negative tumors are typically more immune-infiltrated, and the subset of

patients with high TILs within this subtype respond better to neoadjuvant chemotherapy (NAC). Since immune infiltration is associated with improved response to NAC and overall survival in HR-negative breast cancer patients, new avenues of treatments that boost immune infiltration for these highly-aggressive tumors should be explored. Namely, to study the mechanisms that restrict TIL entry into TNBC and HER2+ breast tumors that show little or no immune reactivity.

1.5 Breast cancer immunotherapy in the clinic

The excitement of immunotherapy has translated to breast cancer in recent years, and a number of clinical trials have recently reported encouraging results. Most of these studies focused on the PD-L1-positive population, as PD-L1 positivity has been associated with improved response to immune checkpoint blockade in other cancers (see Patel et. al.) (37). In contrast to the very limited or modest responses in HR-positive disease (38, 39), clinical trials in HR-negative patients show some promising initial results. A study of 111 TNBC patients reported that 59% of patients were PD-L1-positive by IHC; of these PD-L1+ TNBC patients, 32 patients with relapsed or metastatic disease were enrolled in a Phase Ib study of pembrolizumab (anti PD-1). Of these, 27 were eligible for efficacy analysis (Observed Response Rate or ORR) and an 18.5% response rate was observed (40). In another phase I trial of atezolizumab (an anti-PD-L1 antibody), 21 PD-L1-positive metastatic TNBC were tested and reported a similar ORR of 19% (41).

Given the limited success of single-agent immunotherapies in breast cancer, there are many on-going attempts to create a more immune-friendly microenvironment with other therapies, in combination with checkpoint blockade. These include studies testing combinations of exemestane + anti-CTLA4,(42) cryoablation of primary tumors + anti-CTLA4,(43, 44) and HER2-directed vaccines + immune checkpoint blockade.(45, 46). Furthermore, since patients with high TIL have better responses to conventional therapies in breast cancer (discussed above), combinations of immune checkpoint blockade with conventional chemotherapies are also being investigated. The I-SPY 2 trial is testing the addition of pembrolizumab to standard neoadjuvant chemotherapy regimens in HER2-negative locally-advanced BC. Recently reported results showed that the combination of pembrolizumab + chemotherapy led to an impressive almost three-fold increase in response rates (pCR) compared with chemotherapy alone in TNBC and HR-positive/HER2-negative patients. (J Clin Oncol 35, 2017 (suppl; abstr 506)).

Lastly, in patients with metastatic triple-negative breast cancer (TNBC), the addition of anti-PDL1 antibody atezolizumab to nab-paclitaxel led to a 2-year OS rate of 54%, compared with 37% in the placebo + nab-paclitaxel group. The FDA has now approved this treatment for metastatic TNBC (47).

1.6 Summary of immunotherapy in the clinic

The above description highlights the paradigm shift currently underway in cancer care. While the initial FDA approvals for checkpoint immunotherapy were

granted mostly in melanoma and lung cancers up to 2016, many different tumor types have garnered FDA-approved immunotherapies since then (48). These include head and neck cancers, renal, hepatocellular, colorectal, urothelial, gastric, cervical, breast and Merkel cell carcinomas. In addition, the FDA recently granted approval for pembrolizumab for MSI-h patients, regardless of their tumor type.

While an unprecedented number and percentage of patients are responding to these novel immunotherapies (in terms of their response rates and long-term survival), the majority of patients treated with immune checkpoint blockade fail to respond to therapy (Table 1). The biomarkers that best predict response to immunotherapy thus far are (i) the presence of existing inflammation in the tumor (49); (ii) a high tumor mutation burden (50, 51); and (iii) increased PDL-1 expression. (Table 1)

1.7 Barriers to efficacy of immunotherapy

Although the presence of TILs in breast tumors leads to improved prognosis in patients, immune cells must overcome many challenges before they are able to directly interact with tumor cells and exert their anti-tumor effector function. Tumors are known to exhibit numerous mechanisms that lead to an immune-suppressive microenvironment, where immune cells are restricted from entering the tumor, become inactivated within the tumor, or even promote further immune-suppression (52).

1.8 Lactic acid regulates immune-cell function within the tumor microenvironment (TME)

Tumors have been observed to have increased rates of glycolysis since 1927, when Otto Warburg published his original seminal study (53). Since then, and especially within the last two decades, the importance of tumor metabolism for fueling rapid cell proliferation has been increasingly appreciated. It is now recognized that both glucose and other nutrients (lipids, amino acids) are critical not only for energy (ATP) production, but more importantly for providing the molecular building blocks required for cell proliferation, such as proteins, nucleotides and plasma membranes (54). Not surprisingly, oncogenic pathways involved in malignant transformation have been shown to upregulate expression of glycolytic genes to fuel cell growth. For example, Myc was shown to up-regulate LDHA in 1997 and has been shown to upregulate many other glycolytic genes since then (55, 56). The PI3K/Akt/mTOR pathway was known to be involved in physiological glucose homeostasis (57), and in 2004 it was shown that Akt could directly upregulate glucose uptake in cancer cells (58), an effect that was later found to rely on upregulation of the glucose transporter and several other glycolytic enzymes (59, 60). Mutation or loss of p53 was also shown to lead to decreased oxidative phosphorylation and increased lactate production through enhanced glycolysis (61), an effect thought to be mediated mostly via TIGAR (62). Similarly, BRAF was recently shown to upregulate expression of a number of glycolytic genes, and glycolysis was found to be critical for the resistance to BRAF inhibition in a melanoma cell line (63). Furthermore, hypoxia in the tumor

microenvironment can lead to stabilization of Hypoxia Inducible Factors (HIFs), which have been show to upregulate expression of glycolytic genes (64, 65). Thus, pathways that promote cell proliferation and malignant transformation are tightly associated with increased rates of glycolysis, and thus, secretion of lactic acid within the tumor microenvironment. This metabolic sequence leads to an acidic microenvironment with a low extracellular pH (pHe) ranging from 6.5-7.25 in human breast tumors (66, 67). Importantly, lactic acid accumulation within primary tumors has been linked to poor prognosis in a variety of cancer types (68-71).

Tumor-derived lactic acid has been shown to have many pro-tumorigenic effects, including promotion of angiogenesis (72, 73), increased cancer cell migration (74), fueling oxidative cancer cells ('reverse Warburg' effect) (75, 76), and contributes to an overall immune-suppressive tumor microenvironment (TME). Many excellent reviews have been written on the effects of lactic acid on tumor cells and infiltrating immune cells (77, 78); the following is a brief composite overview of the immune-suppressive effects of lactate.

As mentioned above, anti-tumor immune responses require many steps to be successful, and lactate has been shown to inhibit many of these key steps. Lactate was shown to inhibit TNF-a production from human monocytes, and although extracellular pH (pHe) contributed to this effect, pHe alone did not fully recapitulate the effects of lactic acid (79). Further, a study on dendritic cells (DCs) found that lactate inhibited endocytosis (necessary for antigen capture), cytokine production, T-cell activation potential, as well as expression of the DC-

specific markers CD1a and CD209 in a dose-dependent manner (80). Similar studies on DCs showed that lactic acid dramatically reduced CD1a expression during DC differentiation while and acidic pHe (6.0) had a minimal effect. In addition, conditioned media from 3D melanoma cell cultures were found to significantly inhibit DC-specific CD1a expression that could be rescued by addition of oxamate (an LDH inhibitor) to the 3D tumor cell cultures (81). An important cell type mediating immune suppression are Myeloid Derived Suppressive Cells (MDSCs), which are a very heterogeneous population of myeloid cells that include myeloid progenitor cells, immature dendritic cells and granulocytes (82). Lactate was shown to enhance generation of MDSCs from the bone marrow of mice, and these MDSCs were then shown to potently inhibit CD4+, CD8+ and NK cell proliferation and cytotoxic capacity. Lactate not only enhanced the number of MDSCs formed, but it also enhanced their immune-suppressive capacity (83). Lactate was also recently found to polarize tumor-associated macrophages (TAMs) towards the pro-tumorigenic M2 phenotype. Lactate was shown to stabilize HIF1a within TAMs and led to increased VEGF and Arginase-1 production, contributing to an immune-suppressive TME (84). Recent studies also showed an inhibitory effect of lactate on NK cells, where addition of lactic acid inhibited NK activation markers, cytokine production, and cytotoxic capacity (83, 85). Furthermore, lactic acid has been shown to inhibit T-cell activation, cytokine production, cytotoxic capacity, and to induce cell death in a manner that was not fully recapitulated merely by acidic pH (86). In 2011, the same group demonstrated that stimulation of TCR signaling led to a rapid (1-

15min) activation of the MAPK, ERK and Akt pathways, and found that the presence of lactic acid specifically prevented the phosphorylation of key members of the MAPK pathway, but not those of the ERK or Akt pathway (87). These observations point to the importance of these signaling pathways for T-cell activation, and illuminate the mechanism responsible for lactate's immune-inhibitory effects. Importantly, these rapid inhibitory effects of lactic acid were not observed with an acidic pH alone. Along similar lines, Haas et. al., showed that lactic acid could directly inhibit chemokine-dependent T-cell motility, mediated through the lactate transporters SLC16A1 (MCT1) and SLC25A2 (SMCT2) (88). Interestingly, clinical trials of immune checkpoint inhibition in melanoma (89) and breast cancer (40) show that increased serum LDH levels correlate with lack of response. Whether increased serum LDH is merely a measure of tumor burden, or whether it reflects the metabolic activity of tumors and the resulting levels of lactic acid within the TME, is something that will need to be studied in more detail. Thus, modulating tumor metabolism may be an important adjuvant approach to improve responses to immunotherapy.

High rates of glycolysis by tumor cells can lead to the accumulation of lactic acid and contribute to creating an immune-suppressive TME, as described above. However, high rates of tumor glycolysis and lactate production also reflect high rates of glucose consumption, as shown by FDG-PET scans. Glycolysis has been known to be a critical step during T-cell activation, and recently competition for glucose within the TME was described as a key factor in promoting T-cell exhaustion (90). Furthermore, the glycolytic metabolite Phosphoenolpyruvate

(PEP) was recently described to be critical for Ca^{2+} influx and NFAT nuclear translocation during T-cell stimulation in both CD4+ and CD8+ T-cells, providing a mechanism for the requirement of glycolysis for T-cell activation (91). An additional role for glycolysis is also emerging in controlling epigenetic mechanisms of tumor and immune cell phenotypes, which is thought to be mediated by production of acetyl-CoA from glucose-derived pyruvate. Acetyl-CoA can be used by Histone Acetyltransferases (HATs) to modify histones throughout the genome and modify cancer and immune cell gene expression (92, 93). Thus, glycolysis has been clearly established to be a critical regulator within the TME that can affect both tumor and immune cell phenotypes.

While immunotherapy is revolutionizing cancer care, the majority of immunotherapy-treated patients still fail to respond to therapy. The best predictor for response to immunotherapy is pre-existing inflammation within tumors. Tumor cell-mediated glucose depletion and lactic acid accumulation have been shown to promote immune exclusion from tumors and resistance to immunotherapy using *in-vitro* and *in-vivo* models of the tumor-immune cell interactions. However, a large scale/extensive interrogation into the role of tumor glycolysis in promoting immune exclusion from human tumors has not been reported.

1.9 Objectives

In this study, we proposed to examine the role of tumor glycolysis in promoting immune exclusion across a panel of different cancer types, with a focus on those cancer types with FDA-approved immunotherapies. Pre-clinical

studies (Chapter 3) show that lactic acid has a strong immune suppressive effects on T-cell proliferation, phenotype and function, and that inhibition of tumor glycolysis (or lactate transport) improved the efficacy of immunotherapy in mouse models of breast and prostate cancer. We found that increased tumor glycolysis (as measured by gene expression of glycolytic genes) was associated with decreased immune infiltration across multiple cancer types (Chapter 4). We validated these findings by IHC staining of primary breast tumors with glycolytic and immune markers, and by culturing T-cells in the presence of lactic acid *in-vitro*.

CHAPTER 2

MATERIALS AND METHODS

2.1 Cells

4T1 cells were derived from a spontaneous breast tumor in a Balb/C mouse, and were provided by Dr. Fred Miller, Karmanos Cancer Institute (94). All cells derived from this cell line were grown in DMEM + 10% FCS supplemented to a total of 25mM glucose, 6mM glutamine. The Firefly-luciferase reporter was developed as previously described by retroviral transduction of dual reporter gene expressing RFP and Firefly luciferase (95). The MycCAP cell line was derived from a c-Myc transgenic mouse with prostate cancer, and was provided by Dr. Charles Sawyers (96). These cells were cultured in DMEM + 10% FCS and supplemented to 25mM glucose. MycCAP cells were retrovirally transduced with vectors to express (i) human PSMA, and (ii) a dual reporter gene expressing GFP and Renilla luciferase, as previously described (96).

2.2 T-cell isolation and phenotypic assays

Spleen-derived T-cells were isolated using CD5 microbeads (Miltenyi Biotec; #130-049-301). For T-cell proliferation assays, isolated T-cells were incubated with 5 uM carboxyfluorescein succinimidyl ester (CFSE) for 10 min. CFSE was then washed out of the media and T-cells were incubated for 48hrs. The percentage of proliferating T-cells was calculated by gating for cells with low intracellular CFSE (i.e., CFSE dye was diluted during cell doubling). T-cell death was assessed by incubating T-cells with the eFluor 506 Fixable Viability Dye (Life

Technologies; #65-0866-14). To measure cytokine secretion, media was collected following 48 hr incubation and assayed with the Luminex-based bead immunoassay. *All T-cell assays and FACS in this study were performed by Dr. Roberta Zappasodi in the laboratory of Dr. Jedd Wolchok.*

2.3 shRNA-mediated depletion of LDHA

4T1 and MycCAP cell lines were transfected with SureSilencing shRNA plasmids targeting mouse *LDHA* as previously described (95). To select for Puromycin resistant cells, cells were cultured with Puromycin at 4ug/ml (4T1) or 6ug/mL (MycCAP). To select for highly LDHA-depleted cell lines, we developed single-cell populations from our LDHA KD bulk cell lines. Thus, “A2-KD”, “A3-KD”, and “LDHA-KD” refer to single cell clones for our 4T1 and MycCAP LDHA KD cell lines, unless otherwise indicated. Scrambled shRNA controls were used as negative controls, and these are referred to as either “A5-NC” or “NC”, for 4T1 and MycCAP, respectively. *The development and in-vitro validation of the 4T1 LDHA KD cell lines was performed by the author of this work (Ivan Cohen), with initial mentoring provided by Dr. Inna Serganova, a Senior Scientist in the Blasberg lab. The development and validation of the B16 LDHA KD cell line was performed by the author. The development and in-vitro and in-vivo validation of the MycCAP LDHA KD cell lines was performed by an undergraduate intern (Avi Albeg) under the direct supervision of the author (IC).*

2.4 Western Blot and antibodies

Cells were grown to about 80% confluence, trypsinized, spun down, pelleted and resuspended in RIPA Lysis buffer (Thermo Fisher Scientific). Protein concentrations were determined using the Pierce BCA Protein Assay (Thermo Fisher Scientific). 10ug of protein was loaded into either 10-well or 17-well 4-12% SDS PAGE gels from Life Technologies. Gels were run at 100-150V for 1-2hrs depending on the molecular weight of the protein of interest. Protein was transferred to nitrocellulose membranes at 25V for 30mins using a semi-dry system. Primary antibodies against LDHA (Cell Signaling Technologies; #2012S) and beta-actin (Sigma Aldrich; #A2228) were incubated overnight. Western blots were developed by a 1hr incubation with an HRP-labeled secondary antibody.

2.5 LDH Activity Assays

Cells were grown to about 80% confluence, trypsinized, counted, and 10,000 cells per well were added to a 96-well plate. Immediately after plating, cells were lysed and LDH activity measured using the Roche Cytotoxicity Detection Assay (Sigma Aldrich; # 11644793001).

2.6 Growth Assays

100K cells were plated on Day 0, and media was replenished on Day 2 of the experiment. Cells were counted on the indicated day.

2.7 CRISPR/Cas9 KO of LDHA

The mRNA sequence was obtained from the NCBI (Ref. Seq: NM_001136069.2). The genomic DNA sequence of LDHA was obtained from the UCSC Genome

Browser (chr7:46845856-46851945). Previous gRNAs in the lab targeted only Isoform 1 of LDHA ("C1-KO"). New sgRNAs designed in this study targeted Isoforms 1 and 2 of LDHA. Plasmids containing sgRNA and the Cas9 gene were co-transfected with a Puromycin-resistance gene. Puromycin-resistant cells were selected by long-term culture with Puromycin (4ug/ml), and resistant cells were tested for their LDHA expression by Western blot. The selected clone was obtained with the following sgRNA: 5'-CACCGCGGGGGCCCGTCAGCAAGAG-3' targeting Exon 4 of LDHA ("C2-KO", a single-cell population clone). Sanger sequencing of the specific LDHA regions was performed by the Integrated Genomics Operations (IGO) core at MSKCC. *The design of initial sgRNAs targeting Isoform 1 of LDHA was performed by the RNAi Core Facility (headed by Dr. Ralph Garippa). The design of the second generation sgRNAs (targeting Isoforms 1 and 2) was performed by the author. All work regarding CRISPR-mediated KO of LDHA shown in this work was performed by the author.*

2.8 SURVEYOR Assay

Cells were pelleted, and genomic DNA collected using QuickExtract and SURVEYOR nucleases from Integrated DNA Technologies. Briefly, genomic DNA was collected, the region targeted by the sgRNA was amplified and the PCR reaction was directly incubated with the components of the SURVEYOR assay (without DNA purification, as this resulted in loss of DNA). DNA was then incubated at 95C for 10 minutes, and then very slowly cooled to 25C. Finally, the annealed DNA was incubated with the SURVEYOR nuclease at 42C for 1hr, and

the samples were run on a 1.5% agarose gel for 15-30 minutes and imaged. *This work was performed entirely by the author.*

2.9 Reverse-Transcriptase PCR (RT-PCR)

Cells were pelleted, and RNA was extracted using the RNeasy Mini Kit (Qiagen; # 74104). A region of LDHA Exon 5 was amplified by PCR using the following FWD and REV primers: 5'-CTGGGGGTTCACGCGCTGA-3' and 5'-ATCTCACTCCCCACAGCTCT-3'. PCR was run for 25-32 cycles, and the products were run on a 1% agarose gel. *This was performed entirely by the author.*

2.10 Seahorse Extracellular Flux Analyzer

25,000 control (NC) or 30,000 LDHA-KD cells were plated a Seahorse XF96 Extracellular Flux Analyzer (Agilent Seahorse XF Technology, MA). Different cell numbers were used to account for differences in cell proliferation overnight. On the day of the assay, Seahorse Assay Media was prepared by adding glucose to 5mM, glutamine to 2mM, and pyruvate to 1mM. Where indicated, Rotenone (0.5 uM), Antimycin (0.5 uM), 2-DG (10 mM) and FCCP (0.5 uM) were injected by the Seahorse instrument. For each well, virtually simultaneous measurements of media acidification (glycolytic Proton Efflux Rate, glycoPER) and Oxygen Consumption Rate (OCR) were performed. Rates of glycoPER and OCR were measured and quantified for individual segments of the experimental timeline: 'Basal' measurements include time points before any injection, and 'Compensatory Glycolysis' refers to the measurements performed

after injection of Rotenone/Antimycin (to stimulate glycolysis) and before injection of 2-DG (which shuts down glycolysis). *Seahorse experiments for NGY-066 were performed by the author. The specific representative Seahorse experiments shown in this work (Figure 3.5) for the comparison of NC vs. LDHA KD 4T1 and MycCAP were performed by Kiran Vemuri (4T1) and Jenny Ijoma (MycCAP).*

2.11 Lactate quantification in extracellular media

Tumor-cell conditioned media (or fresh media as control) was quantified using either the Lactate Colorimetric/Fluorometric Assay Kit (Biovision; #K607) or the Lactate-Glo Assay (Promega; # J5021). Absolute lactate concentrations were calculated using standards of known lactate concentrations. *The work in Figure 3.5C-left (4T1) was performed by Roberta Zappasodi. The work in Figure 3.5C-right (MycCAP) was performed by Jenny Ijoma.*

2.12 NGY inhibitors of MCT1/4

Lyophilized NGY-008 (MCT4 inhibitor) and NGY-066 (MCT1/4 dual inhibitor) were received from Nirogyone Therapeutics, Inc (100 Barber Ave, Worcester, MA). For *in-vitro* studies, compounds were dissolved in pure DMSO and used at a final concentration of 10uM, unless otherwise indicated. For *in-vivo* studies, NGY-008 was diluted to 10mg/kg in a solution 5% DMSO, 10% Solutol, and 85 of 10% Hydroxy-propyl-beta-cyclodextrin (HPBCD, in saline). For NGY-066, the compound was diluted in 950uL of 10% HPBCD (in saline), 20uL Tween 80, and 50uL DMSO. The solution was vortexed and sonicated for 45-60 minutes at room temperature. The solution was then centrifuged at maximum speed for

10 min and the supernatant was filtered and collected for injection. Mice were injected IP twice daily with the appropriate vehicle controls or active compounds at 10mg/kg. *The contact with this company was initiated by the author. Initial in-vitro testing of the compounds' effect on tumor cell phenotype and proliferation were performed by the author. Seahorse experiments with these compounds were performed by the author. Following this initial validation, the in-vitro experiments with T-cell mono-culture or co-culture were performed by Roberta Zappasodi. The lactate/glucose ratios in Figure 3.9C were measured by Dr. Avigdor Leftin in the laboratory of Dr. Jason Koutcher. During the in-vivo experiment combining NGY-066 + immune checkpoint blockade, 4T1 tumors were inoculated by Dr. Inna Serganova, and tumor volume measurements were performed by the author. NGY compounds were prepared and injected twice daily for a week by the author. Immune checkpoint blockade was injected on Days 3, 6, and 9 by Dr. Roberta Zappasodi. Surgery was performed by Dr. Masahiro Shindo on Day 10. BLI imaging and quantification, as well as survival follow-up and survival analysis was performed by the author.*

2.13 Quantification of glucose and lactate by NMR Spectroscopy

Tumor-cell conditioned media was collected and 500uL were loaded into a spin tube and analyzed by ^{1}H-NMR Spectroscopy. Area under the curve (AUC) for glucose (3.22 ppm) and lactate (1.31 ppm) peaks were calculated. *This analysis was performed by Dr. Avigdor Leftin.*

2.14 Anti-PSMA CAR T-cells and chromium release assay

Anti-human-PSMA CAR T-cells were generated as previously reported a collaboration with the Vladimir Ponomarev lab (96). Briefly, monocyte-depleted PBMCs were activated and transduced with two different vectors: (i) a second-generation CAR construct against human PSMA; and (ii) a dual reporter gene that drives expression of RFP and Click Beetle Red (CBR) luciferase. *All CAR T-cells in this work were kindly provided by the Ponomarev lab.*

To assess CAR T-cell cytotoxicity against MycCAP tumor cells, we performed (i) 48 hr co-culture assays and (ii) chromium release assays. During co-culture assays 30,000 MycCAP NC or LDHA KD tumor cells were plated overnight. 150,000 CAR T-cells were then co-cultured with tumor target cells. After 48 hr, all cells were collected and stained for Annexin V and 7-AAD. MycCAP cells were identified by their GFP expression, and T-cells by their RFP expression. Cells were considered apoptotic if they were Annexin-V single-positive, and they were considered to be undergoing the late stages of cell death if they were Annexin-V and 7-AAD double-positive. *This experiment was conceived and designed by the author. MycCAP tumor cells were provided to Dr. Maxim Moroz and Juan Zurita (Ponomarev lab) who performed the co-culture and FACS. The resulting FACS data was analyzed by Dr. Moroz and the author.*

To assess CAR T-cell cytotoxicity, a chromium release assay was performed, as previously described (96). Briefly, target tumor cells were loaded with 100 uCi of ^{51}Cr for 1 hr. Then, 10,000 target cells were incubated with CAR T-cells in different ratios, as indicated, and the ^{51}Cr release into the media was

quantified compared to controls. *Chromium release assays were performed entirely by Dr. Larissa Shenker from the Ponomarev lab.*

2.15 In-vivo models – 4T1 and MycCAP

4T1 tumor cells ($1x10^6$) were diluted in their appropriate media described above (DMEM) and injected into the mammary fat pad of Balb/C mice. MycCAP tumor cells ($1x10^6$) were diluted in a solution of 50% DMEM and 50% Matrigel, and injected into the right flank of SCID mice. Both 4T1 and MycCAP cells used in this study expressed luciferase reporters to allow for non-invasive tracking of tumor growth *in-vivo* (95, 96). 4T1 cells carried a constitutive Firefly luciferase vector, and MycCAP cells carried a constitutive Renilla luciferase vector. *4T1 tumor inoculations were performed by Dr. Inna Serganova. MycCAP tumor inoculations were performed by Avi Albeg.*

To image 4T1 primary tumors, mice were injected IP with 50uL of a 30 mg/ml Luciferin solution. To image metastatic growth, mice inoculated with 4T1 cells were injected IP with 100uL of a 30 mg/ml Luciferin solution. To image primary MycCAP tumors, mice were injected retro-orbitally with 50 uL of a 1 mg/ml Coelentrazine solution. To quantify the degree of metastatic burden in mice, an ROI was drawn either in the thoracic area, or over the entire mouse (as indicated) and BLI intensity quantified. *Imaging in this work was performed collaboratively with Inna Serganova, Dr. Mayuresh Mane, Avi Albeg and Kiran Vemuri. Retro-orbital injections were performed by Avi Albeg. Quantification of signal intensities shown in this work was performed by the author.*

For the ‘4T1 Surgical Model’ (which replicates the clinical treatment of breast cancer), tumors were surgically resected by two highly skilled surgeons in the lab (either Dr. Masahiro Shindo, or Dr. Masatomo Maeda) when they reached 100-200mm^3. Typically, 4T1 NC tumors were resected on Day 10, and 4T1 A2-KD on Day 13 of tumor growth. Following surgery, mice were imaged weekly or bi-weekly to follow metastatic outgrowth, and their overall survival was calculated.

For the CAR T-cell treatment of PSMA-positive MycCAP tumors (NC vs. LDHA KD), tumor cells were injected as above. When tumors reached 50-100mm^3 (approximately Day 7 for NC, and Day 9-10 for LDHA KD), mice were injected IV with 10x10^6 CAR T-cells. CAR T-cells expressed a constitutive Firefly luciferase reporter. To determine T-cell trafficking and persistence *in-vivo*, we injected mice IP with a 100uL of 30 mg/ml Luciferin solution. To identify the location of MycCAP tumors, BLI for Renilla luciferase was performed prior to CAR T-cell injection. Following CAR T-cell injections, quantification of CAR T-cells trafficking to the tumors was determined by Firefly luciferase BLI and an ROI drawn over the location of the tumor, as previously determined by the prior Renilla luciferase BLI study. To determine CAR T-cell trafficking to tumors ex-vivo, tumors were excised on Day 6 after CAR T-cell injection, and a single-cell suspension obtained using Roche Liberase TL (Sigma Aldrich; #5401020001). MycCAP tumors cells were identified by their expression of GFP, and CAR T-cells by their expression of RFP. *CAR T-cell experiments in this study were a major collaboration between the Blasberg and Ponomarev laboratories. The*

detailed experimental design of the initial in-vivo experiments shown in this work was performed by the author. MycCAP tumor-cell inoculations were performed by Avi Albeg. Tumor measurements were initially performed by the author. BLI imaging was performed by the author in collaboration with Mayuresh Mane and Avi Albeg. CAR T-cells were prepared and validated by Juan Zurita and Dr. Anna Moroz (Ponomarev lab). CAR T-cells were injected IV by Anna Moroz. Quantification of CAR T-cell intensities in-vivo in the specific experiments shown in this work was performed by the author. Tumor extractions and preparation of single-cell suspensions were performed by the author, and these were provided to Juan Zurita and Anna Moroz for FACS analysis. The resulting FACS data was analyzed by Dr. Anna Moroz and the author.

2.16 Immunostaining and quantification

Tumors were placed in 4% PFA overnight and then washed with ethanol (3 times x 30 mins) and water (1 x 6 hr). H&E and immunofluorescence staining was performed by the Molecular Cytology Core Facility (MCCF) at MSKCC, and analysis was performed in MetaMorph (Molecular Devices) and ImageJ. To quantify the vascularity of tumors, a threshold for CD31-positive pixels was manually selected and applied to all images. The percentage of CD31-positive pixels divided by the total tumor area is reported (%). To quantify immune-cell infiltration into tumors, a threshold for the indicated marker (CD3, CD4, CD8, F4/80) was manually selected, and the number of marker-positive cells divided by total tumor area is reported (# of positive cells / mm^2 of tumor). To quantify necrosis, H&E images were scanned and necrotic areas were manually

delineated by an observer blinded to the origin of tumors (NC vs. KD). The number of necrotic pixels were divided by the total tumor area and reported (%). *Tissue processing and sectioning onto slides was performed by Dr. Ning Fan (MCCF). Immunofluorescence staining was performed by Dr. Dimitry Yarilin (MCCF). Images were digitized in the MCCF. Quantification of necrosis area was performed by Avi Kerendian, an undergraduate intern, under the direct supervision of the author. TAM Density was quantified by Dr. Mayuresh Mane under the supervision of the author. All other image analysis (CD31, CD3, CD4) was performed by the author.*

To quantify the degree of T-cell infiltration in the periphery and interior of tumors, multiple small ROI's were consecutively drawn starting from the tumor periphery and into the tumor core. The number of CD3-positive pixels per ROI were divided by the total number of pixels in that ROI to obtain a percentage of CD3-positive pixels in multiple ROIs at different lengths from the tumor periphery. The average CD3-positive area (%) was averaged across multiple regions of the tumor, and further averaged for the NC and LDHA KD tumors. *This work was performed by the author, with significant guidance from Dr. Sho Fujisawa from MCCF.*

To quantify the CD31-positive area and CD3-positive area, tumors were divided into small ROIs, and thresholds for CD31 and CD31 manually selected and applied across all ROIs and tumors. *This work was performed by the author.*

2.17 Bioinformatic data download and processing

Gene expression data was downloaded from all 33 cancer types in the TCGA PanCancer Atlas cohort from www.cbioportal.org, except Acute Myeloid Leukemia (LAML), Thymoma (THYM) and Diffuse Large B Cell Lymphoma (DLBC), since we focused on solid tumors. The RSEM expression values from the cBioPortal were then transformed to log2 values, and further transformed by scaling gene-wise to a Z-score centered around 0 for each of the 30 cancer types. Z-scaling was performed individually per tumor type. Unless otherwise noted, all gene expression data presented in this study is the Z-score of the log2 RSEM expression values. For development of gene expression signature (GlyScore, ImmScore, APCScore), we used the entire cohort of 30 tumor types. To study the relationships between GlyScore and ImmScore, we focused our analysis on solid tumor types which currently have FDA-approved immunotherapies: melanoma (SKCM), lung (LUAD, LUSC), urothelial (BLCA), renal (RCC), head and neck (HNSC), hepatocellular (LIHC), gastric (stomach (STAD), esophageal (ESCA)), colorectal (COAD, READ), breast (BRCA), cervical (CESC).

2.18 Development of gene signatures

To develop gene signatures that would serve as a surrogate for immune infiltration (ImmScore), we plotted the cross-correlation of several immune-related genes and found that they all showed high degrees of positive correlation (Pearson coefficients ranging from 0.75-0.95, data not shown). Thus, we decided to take only genes that would serve as a surrogate specifically for T-cell abundance within tumors and we selected (CD3D, CD3E, CD8A, LCK). To

develop gene signatures that would serve as a surrogate for glycolytic activity and potential (GlyScore) and antigen processing and presentation capacity (APCScore), we first downloaded gene sets from the Broad Molecular Signature Database (MSigDB) from the Gene Ontology (GO), REACTOME, or KEGG groups. For GlyScore, we selected gene sets (pathways) that contained the terms “glycolysis” or “glucose catabol” (to ensure inclusion of “catabolic”, and “catabolism”), resulting in a list of 75 unique genes involved in this process. We plotted the cross-correlation of these 75 genes across the entire cohort of 9,715 tumor samples (direct Z-scale of the RSEM values) ordered by the first principal component (using the corrplot package) and selected the genes mentioned in the main text. As a surrogate for antigen processing and presentation capacity (APCScore), due to the redundancy of many pathways, we manually selected the following 5 pathways: “antigen processing and presentation of peptide antigen via MHC class I” (GO), “antigen processing and presentation of endogenous antigen” (GO), “antigen presentation folding assembly and peptide loading of class I MHC” (REACTOME), “antigen processing and presentation via MHC class Ib” (GO), and “antigen processing and presentation of endogenous peptide antigen” (GO). This resulted in a list of 101 unique genes. We plotted the cross-correlation of these genes, ordered them by hierarchical clustering, and found a cluster containing many genes widely involved in antigen processing and presentation showing high degrees of cross-correlation to each other, so we selected this cluster as our APCScore. Cytolytic score was computed by taking the mean of Granzyme A (GZMA) and Perforin (PRF1), as previously described

(97). Tumor Inflammation Score (TIS) was obtained by calculating the mean of the genes previously described (115).

2.19 Mononuclear cell quantification in TNBC

Data containing histological quantification of mononuclear cell infiltration was downloaded from Lehmann, et. al.(98), and plotted against ImmScore.

2.20 Associations between GlyScore and ImmScore

To determine the linear associations between GlyScore and ImmScore, these values were plotted for each tumor and a summary Pearson and Spearman correlation was calculated for each disease type, shown in the summary plot in Fig 2A. To test for mutual exclusivity, the Z-scaled RSEM values (not the Z-scale log2 RSEM) were plotted. As a threshold for determining overexpression of either signature, we chose a cutoff of 0.5 standard deviations above the mean to indicate “glycolytic” or “robustly infiltrated” tumors for GlyScore and ImmScore, respectively. This value, which tended to fall near a Z-scaled value of 0.5, roughly separated samples into “top third” vs. “bottom two thirds” and provided for sufficient numbers of samples in each group to allow meaningful statistical comparisons. To test for mutual exclusivity between GlyScore and ImmScore, we calculated the Odds Ratio for a sample being both high glycolytic (expression > 0.5 SD above the mean for GlyScore) and robustly infiltrated (expression > 0.5 SD above the mean for ImmScore).

2.21 Unbiased gene expression and network analysis

To determine gene expression patterns enriched in the immune-depleted phenotype, differential gene expression analysis was performed between the 'Immune-depleted' vs. 'Immune-enriched' phenotypes in Figure 2A individually for each tumor type. This was followed by Gene Set Enrichment Analysis (GSEA) with pathways downloaded from the Broad MSigDB. Only gene sets ('pathways') from GO, KEGG and Reactome were used. The p-values for each gene set in the resulting GSEA tables from each tumor type was combined by using Fisher's method, resulting in a single table of gene sets enriched in the 'Depleted' phenotype (typically with 200-500 significantly enriched gene sets). To reduce the dimensionality of this large table, and taking into account the redundancy of multiple gene sets, these gene sets were combined into biological networks by calculating the degree of overlap of genes within 2 gene sets (i.e., the number of genes in common / the number of genes in the smallest of the 2 gene sets). Gene sets were considered to be in the same network if their degree of overlap was higher than 37.5%. Networks were labeled according to the frequency of individual terms in the names of gene sets within each network, or according to the frequency of individual genes within each network.

2.22 Cases

Following institutional review board approval (Protocol # 17-236A), cases were retrieved from the Pathology archives of Memorial Sloan-Kettering Cancer Center (MSKCC). Patient consents were obtained as required. 49 cases were reviewed by two pathologists (Drs. Fresia Pareja and Jorge Reis-Filho) and classified according to the definitions of the World Health Organization. Tumors

were graded according to the Nottingham grading system (99). ER and HER2 status were determined by immunohistochemistry and/or fluorescence in situ hybridization (FISH), following the American Society of Clinical Oncology/College of American Pathologists (100, 101). The extent of tumor infiltrating lymphocytes was evaluated following the recommendation put forward by the International TILs Working Group 2016 (102). *Institutional Review Board documents were written by the author, with significant guidance from Dr. Elizabeth Sutton. Large databases containing patient information (tumor type, treatments (chemotherapy, radiation, surgery), imaging (MRI and PET)) were kindly provided by Danny Martinez from the Sutton group. These multiple databases of thousands of patients were merged by the author, and patients meeting the study requirements (primary, untreated, ER-negative breast cancer, preferably with imaging prior to mastectomy), were selected by the author.*

2.23 Immunohistochemistry and pathology

Representative sections from the 49 formalin-fixed paraffin-embedded whole tissue sections were stained for 30 min with the anti-CD3 antibody (Leica Biosystems, Clone LN10) at a 1:200 dilution; and anti-CD8 antibody (Dako Omnis, Clone C8/144B) at a 1:100 dilution; and anti-LDHA antibody (Cell Signaling, Clone C4B5; #3582) at a 1:300 dilution; and anti-GLUT1 (Polyclonal from AbCam) antibody at a 1:400 dilution, all with a 30 min ER2 pre-treatment (Bond) on a Leica Bond RX platform, followed by Bond Poymer Refine Detection (Leica Biosystems; #DS9800). *IHC staining of tumor samples was performed by Drs. Irina Linkov and Marina Asher from the Pathology Department at MSKCC.*

Immunohistohemical expression of LDHA and GLUT1 was assessed using the H-score, a semi-quantitative approach based on the sum of individual scores for each intensity (0, negative; 1+, weak; 2+, moderate; 3+, strong) and the percentage of tumor cells displaying a particular expression intensity. The final score is computed with the formula: [1x(%cells 1+) +2 x(%cells 2+) +3x (% cells 3+)] and ranges from 0 to 300. Immunohistochemical assessment of CD3 and CD8 expression in TILs was recorded as the % of TILs displaying immunoreactivity for these markers. *Histological quantification of markers was performed by Dr. Fresia Pareja. Comparative analysis of this data was performed by the author.*

Note: all bioinformatics work in this study (Chapter 4) was performed with critical advice and guidance from Drs. Nicholas Socci, Raya Khanin (Bioinformatics Core) and Jorge Reis-Filho (Department of Pathology).

CHAPTER 3

In-vitro and *in-vivo* assessment of immune-suppressive effects of lactic acid

3.1 Introduction

An abundance of literature has shown that lactic acid is highly immune suppressive by acting on multiple cell types, as described in Section 1.2.2 of this work. In this chapter, we set out to further explore the hypothesis that lactic acid can have direct suppressive effects on T-cells. We also tested the hypothesis that inhibiting lactate transport across the plasma membrane by using inhibitors of Monocarboxylate Transporters 1 and 4 (MCT1/4) would inhibit the secretion of lactic acid from tumor cells and thus may enhance immune cell function in co-culture experiments.

3.2 Results

3.2.1 Lactic acid inhibits T-cell proliferation and induces apoptosis

We cultured bone-marrow derived mouse T-cells in the presence of increasing amounts of lactic acid (0.01 – 20mM) and measured the percentage of proliferating or dying cells (**Figure 3.1**). We found that around 6-20mM, CD4+ and CD8+ T-cells showed a dramatically reduced proliferation rate (as measured by the percentage of CFSE-low T-cells) and a dramatic increase in the percentage of dying cells (as measured by the eFluor 506 viability dye).

To determine how lactic acid may affect T-cell phenotype, we cultured CD4+ and CD8+ T-cells in the presence of increasing amounts of lactic acid (0, 2.5 and 10mM) for 48 hrs, and measured the expression levels of the activation markers CD25 (IL2 receptor) and PD1 (**Figure 3.2**). The addition of lactic acid to the media resulted in decreased T-cell proliferation and expression of the activation markers CD25 and PD1, and increased cell death, as determined by both the percentage of CD25+ cells and by the mean fluorescence intensity of CD25 or PD1 in individual T-cells.

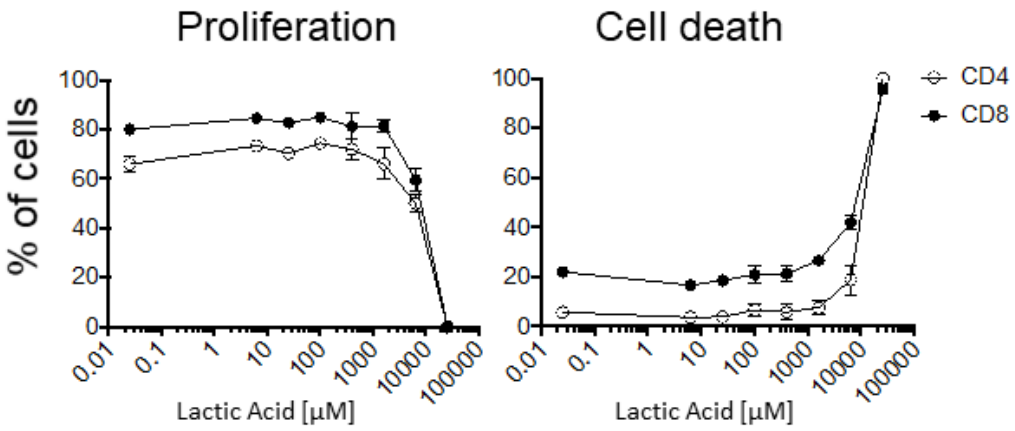

Figure 3.1. Effects of lactic acid on T-cell proliferation and apoptosis. Bone-marrow derived T-cells were isolated and incubated for 48 hrs in the indicated concentrations of lactic acid. Proliferation (CFSElow) and cell death (eFluore 506 Viability Dye) were then measured by FACS. *This unpublished experiment was performed entirely by R. Zappasodi*.

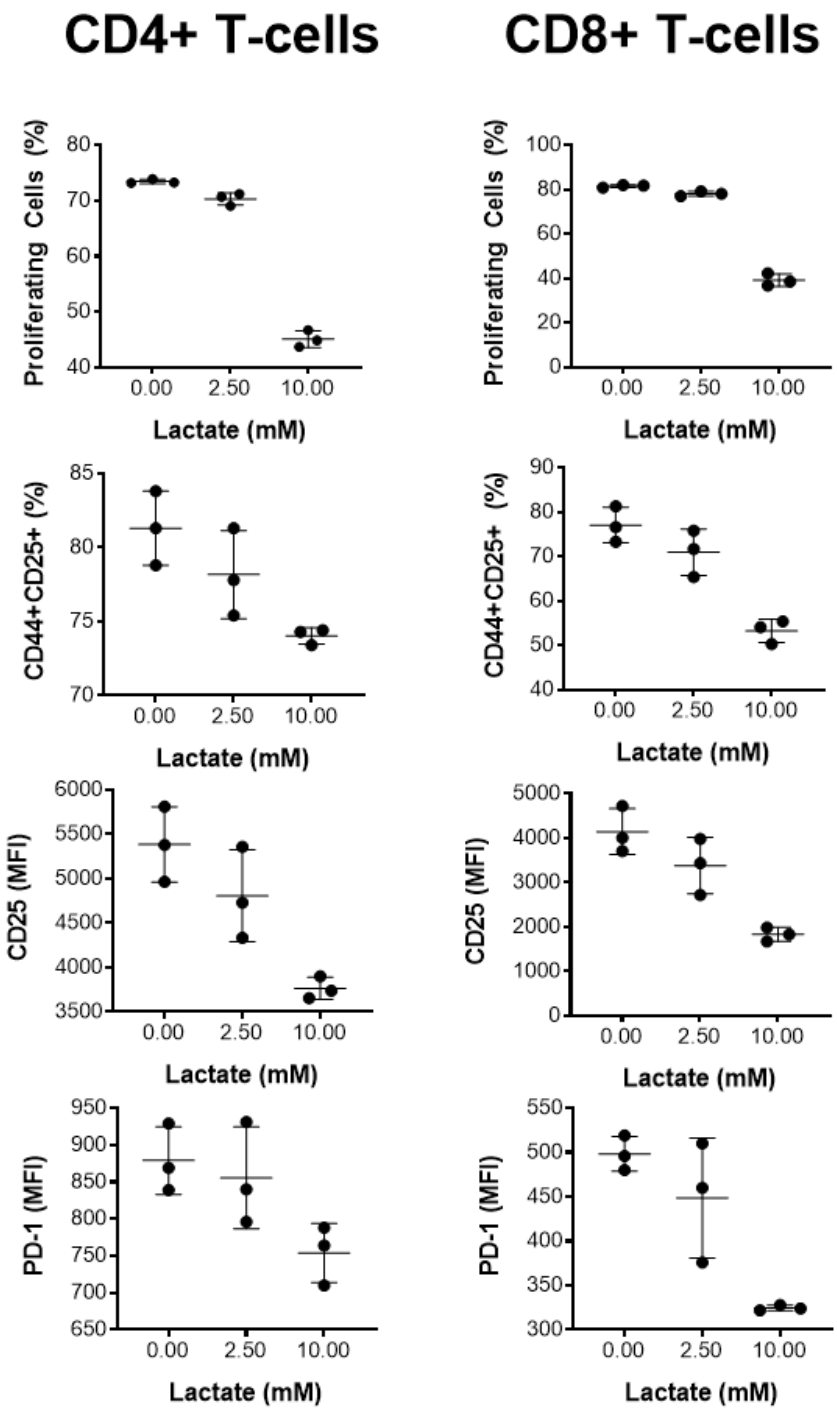

Figure 3.2. Effects of lactic acid on T-cell phenotype. Bone-marrow derived T-cells were isolated and incubated for 48 hrs in the indicated concentrations of lactic acid. Cells were then stained and their proliferation, death, and activation status as indicated. CD44+CD25+ refers to the percentage of CD44+CD25+ cells as a percentage of the total number of CD4 or CD8 T-cells as indicated. *This unpublished experiment was performed entirely by R. Zappasodi*.

3.2.2 Development of LDHA-depleted 4T1, B16 and MycCAP murine cancer cell lines

To test our hypothesis in a setting that resembled the tumor cell-immune cell crosstalk present within tumors, we developed tumor cell lines with depletion of the glycolytic enzyme LDHA. LDHA catalyzes the conversion of pyruvate to lactate in the last step of glycolysis, and its reduction has been shown to lead to decreased lactate levels within tumors (103). We developed LDHA-depleted 4T1, B16 and MycCap tumor cell lines, which are commonly used murine models of breast, skin, and prostate cancer, respectively. We transfected cell lines with multiple LDHA-targeted shRNAs (LDHA KD) as well as a scrambled shRNA negative control (NC), both of which included a Puromycin resistance gene. After appropriate culture under Puromycin selection (4ug/ml), we obtained a number of clones which showed efficient LDHA depletion by Western blot and LDH activity assays (with a reduction in LDHA expression of 60-95%) (**Figure 3.3**).

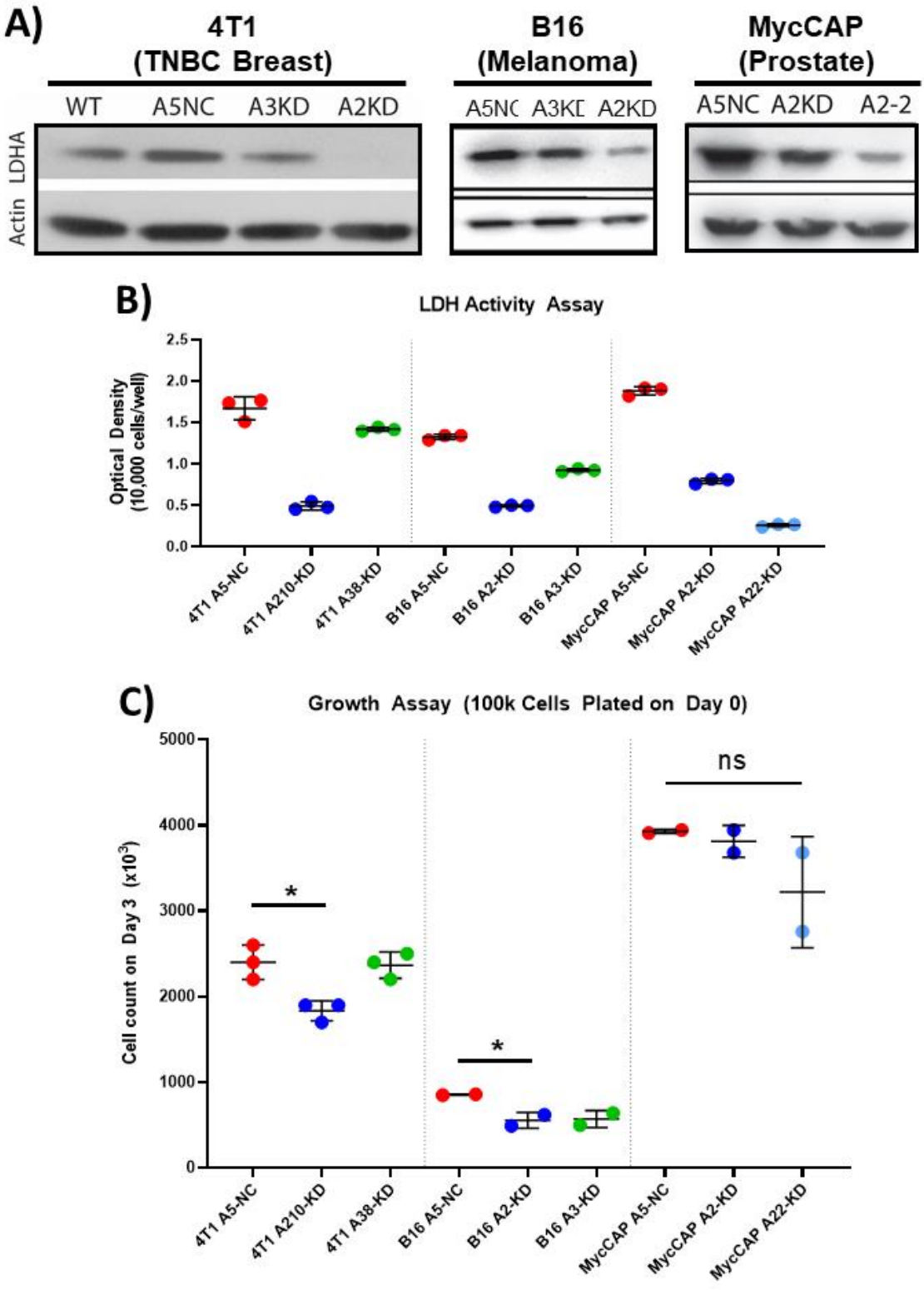
A)
4T1
(TNBC Breast)
B16
(Melanoma)
MycCAP
(Prostate)
WT
A5NC
A3KD
A2KD
A5NC
A3KD
A2KD
A5NC
A2KD
A2-2
LDHA
Actin
B)
LDH Activity Assay
Optical Density
(10,000 cells/well)
2.5
2.0
1.5
1.0
0.5
0.0
4T1 A5-NC
4T1 A210-KD
4T1 A38-KD
B16 A5-NC
B16 A2-KD
B16 A3-KD
MycCAP A5-NC
MycCAP A2-KD
MycCAP A22-KD
C)
Growth Assay (100k Cells Plated on Day 0)
Cell count on Day 3 (x10³)
5000
4000
3000
2000
1000
0
*
*
ns
4T1 A5-NC
4T1 A210-KD
4T1 A38-KD
B16 A5-NC
B16 A2-KD
B16 A3-KD
MycCAP A5-NC
MycCAP A2-KD
MycCAP A22-KD

Figure 3.3. Development and validation of shRNA-mediated depletion of LDHA in multiple cancer cell lines. A) 4T1, B16 and MycCAP murine cancer cell lines were transfected with 4 different LDHA-targeting shRNAs (A1-A4) and a scrambled control (A5). Cells were collected during optimal growth conditions and their LDHA expression assessed by Western Blot. B16 A2KD and A3KD refer to bulk populations, not single-cell populations. Similarly, A2KD MycCAP cells are a bulk population, while A22 is a single-cell clone. **B)** 10,000 cells were plated in a 96-well plate and their LDH activity measured using a Roche Cytotoxicity Detection Kit, which measures LDH activity. **C)** 100k cells were plated in a 6-well plate, and the number of cells 72hrs later was assessed using a Countess Cell Counter.

3.2.3 CRISPR-mediated LDHA KO in 4T1 cell lines

While shRNA-mediated LDHA depletion provided us with an efficient knock-down of LDHA protein, enzyme activity, and decreased tumor cell proliferation (Figure 3), this method has 2 limiting caveats: (i) we still observed some remaining LDHA expression in our LDHA KD cells; and (ii) given that Puromycin would be absent during *in-vivo* tumor growth, we feared that LDHA may become upregulated *in-vivo* during the 10-30 days of tumor growth. To address these issues, we developed a CRISPR/Cas9-mediated knock-out of LDHA by transfecting 4T1 cells with Cas9 and guide RNAs (gRNAs) targeting LDHA (**Figure 3.4A**). Initial efforts using an initial gRNA (gRNA1) that targeted only 1 isoform of LDHA yielded a positive mutation (as measured by the SURVEYOR assay, and by Sanger sequencing; Figure 3.4B, C). Further, when compared with a scrambled gRNA control (C8-KO), this clone (C1-KO) also showed decreased LDHA mRNA and protein levels as measured by Real-Time PCR, Western blot, and the LDH activity assay, respectively (Figure 3.4E, F, G). However, we noticed that there was still significant LDHA expression in the C1 LDHA KO cell line as measured by Western blot. Thus, we designed new gRNAs to target both main LDHA isoforms (gRNA2, Figure 3.4A). This strategy also yielded positive mutation results as per Sanger sequencing (Figure 3.4D), and it also showed decreased LDHA mRNA and protein levels, as well as a significant reduction in LDH enzyme activity. Importantly, the levels of LDHA protein and LDH enzyme activity were significantly lower in the C2-KO clone (using gRNA2) compared to C1-KO clone (using the original gRNA1). Notwithstanding the

increased efficacy of LDHA KO in the C2-KO cell line (Fig. 3.4F-G), both C1-KO and C2-KO showed a similar decrease in proliferation compared to the C8-KO control (Fig. 3.4H).

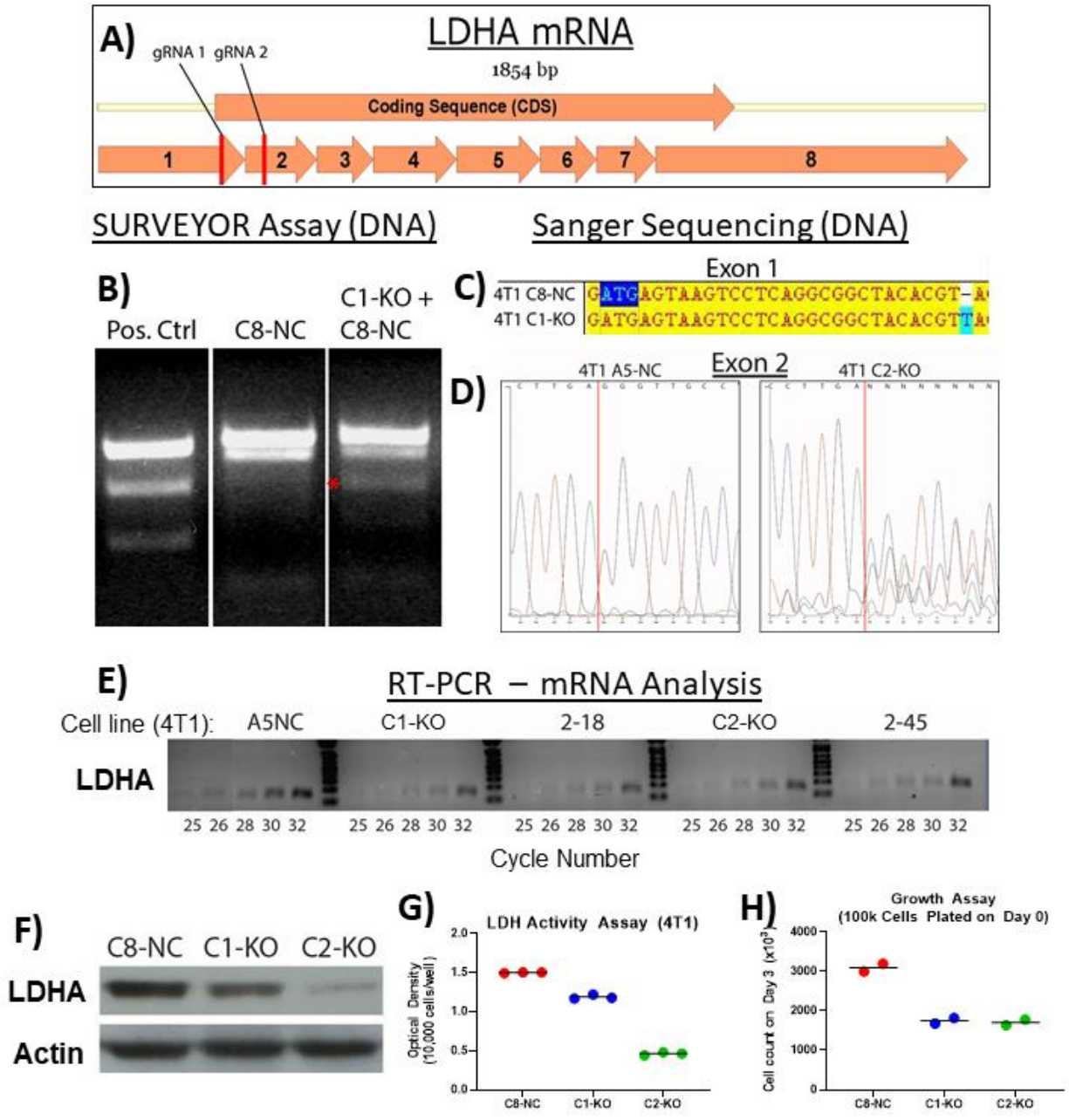
A)
LDHA mRNA
1854 bp
gRNA 1
gRNA 2
Coding Sequence (CDS)
1
2
3
4
5
6
7
8
SURVEYOR Assay (DNA)
Sanger Sequencing (DNA)
B)
Pos. Ctrl
C8-NC
C1-KO + C8-NC
C)
Exon 1
4T1 C8-NC
4T1 C1-KO
D)
Exon 2
4T1 A5-NC
4T1 C2-KO
E)
RT-PCR – mRNA Analysis
Cell line (4T1):
A5NC
C1-KO
2-18
C2-KO
2-45
LDHA
25 26 28 30 32
Cycle Number
F)
C8-NC
C1-KO
C2-KO
LDHA
Actin
G)
LDH Activity Assay (4T1)
Optical Density (10,000 cells/well)
H)
Growth Assay
(100k Cells Plated on Day 0)
Cell count on Day 3 (x10³)

Figure 3.4. Analysis of CRISPR-Cas9-mediated LDHA KO in 4T1 cells. A) LDHA mRNA structure. **B)** SURVEYOR assay of a control sample with a known DNA mismatch (*left*), a sample with C8-NC LDHA DNA only (*middle*), and a mixture of LDHA DNA from C8-NC and the C1-KO clone (*right*). DNA cleavage (marked by a red asterisk) indicates that C1-KO has a mutated LDHA gene, which is confirmed by sequencing (**C**). **D)** C2-KO was obtained by targeting both LDHA isoforms, and sequencing of C2-KO DNA also shows mutations in the LDHA gene. E) RNA was purified from control or different LDHA KO single cell clone populations, and real-time PCR was performed to assess LDHA mRNA levels. **F)** Cell lysates of the indicated cell lines were processed for Western blot analysis and stained for LDHA and Actin. **G)** 10k of the indicated cell lines were plated on a 96-well plate and LDH activity assay was performed. **H)** 100k cells of the indicated cell lines were plated on a 6-well plate, and the number of living cells was counted 72hrs later.

We found that these LDHA-depleted cells also consumed less glucose and produced less lactate compared to controls (**Figure 3.5**). Furthermore, we studied the real-time secretion of lactic acid by performing extracellular acidification rate experiments with the Seahorse XF Extracellular Flux Analyzer in our 4T1 and MycCAP NC and LDHA KD cell lines (Figure 3.5A-B). We found that 4T1 LDHA KD cell lines exhibited similar glycolytic proton efflux rate (glycoPER) in the baseline setting, but their glycoPER was significantly reduced compared to NC controls under conditions of 'compensatory glycolysis' (i.e., when oxidative phosphorylation is shut down and cells switch to their maximal glycolytic capacity). In contrast, MycCAP LDHA KD cells exhibited dramatically reduced glycoPER in both the baseline and compensatory conditions. Furthermore, both 4T1 and MycCAP LDHA KD cell lines showed increased mitochondrial oxidative phosphorylation compared to NC controls, as evidenced by their increased oxygen consumption rate (OCR). Finally, we cultured 4T1 and MycCAP NC and LDHA KD cell lines for 24 and 72 hrs, respectively, and measured the amount of lactate secreted into the extracellular media (Figure 3.5C). We found that both LDHA-depleted cell lines secreted significantly less lactate to the media compared to the scrambled shRNA negative controls (A5-NC). Based on these results, we concluded that 4T1 and MycCAP NC and LDHA KD cell lines exhibited different metabolic profiles, and that they show decreased glycolytic rates and lactate secretion compared to controls.

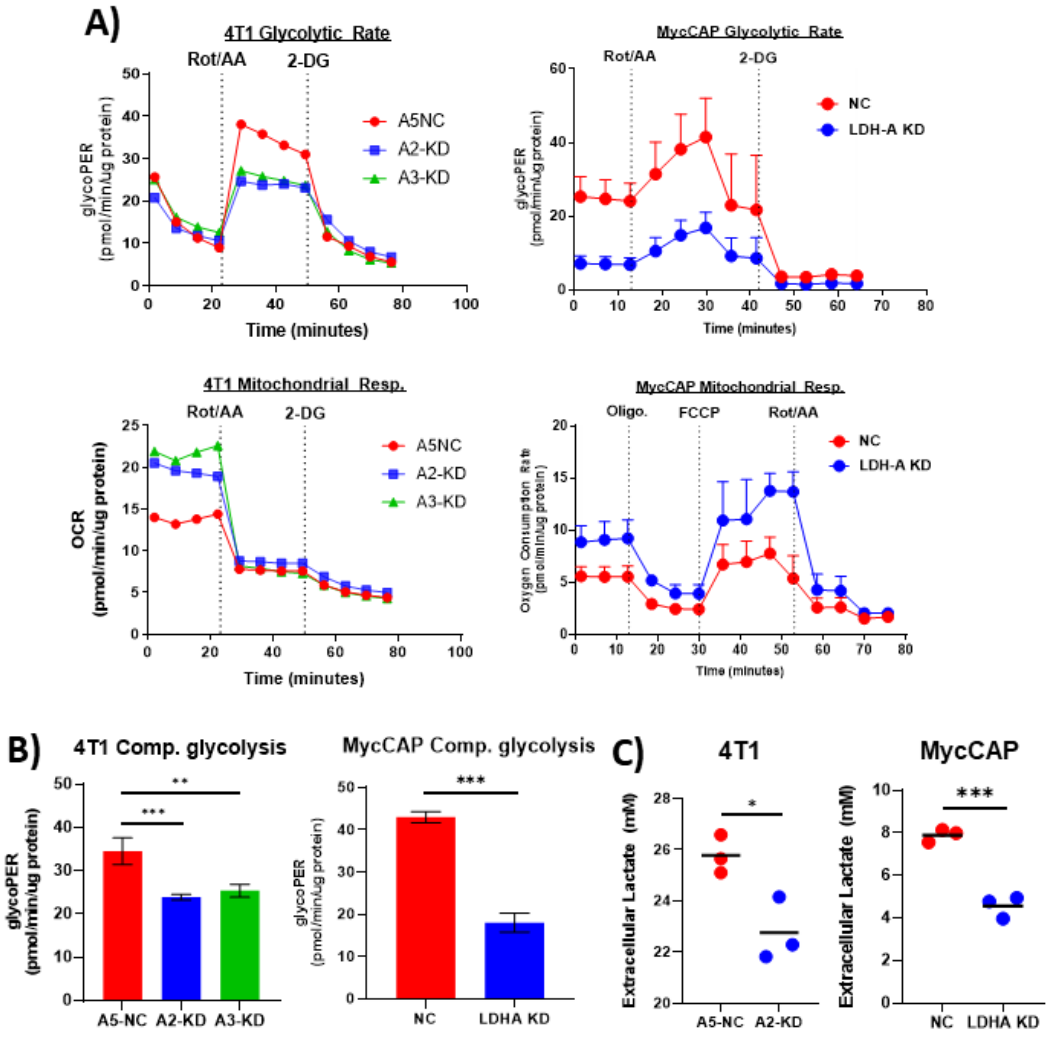

Figure 3.5. LDHA depletion leads to reduced glycolytic rate, lactate secretion, and increased mitochondrial respiration *in-vitro*. A) 4T1 (*left*) or MycCAP (*right*) NC or LDHA-depleted cells were plated and allowed to rest overnight. Cells were then incubated under serum-free conditions for 1hr prior to beginning of the Seahorse Extracellular Flux Analyzer assay. Glycolytic Proton Efflux Rate (glycoPER) and Oxygen Consumption Rate (OCR) was measured. **B)** Compensatory glycolysis (time points between Rot/AA and 2DG injections) was quantified and plotted for 4T1 and MycCAP cell lines. **C)** 4T1 or MycCAP NC or LDHA KD cells were plated and the extracellular lactate was quantified after 24 hrs (4T1, left) and 72 hrs (MycCAP, right). *A portion of this work is from Serganova et. al (95).*

3.2.4 *In-vivo* effects of LDHA depletion on tumor growth

The Blasberg laboratory had shown that 4T1 NC and LDHA KD tumors could grow in immune-compromised (nude) or immune-competent (Balb/C) mice ((103) and **Figure 3.6A**, respectively). These tumors grew rapidly in the mammary fat pad, followed by quick metastatic progression to the lungs, as detected by expression of Firefly luciferase (Fluc) and bioluminescence imaging (BLI) (Figure 3.6B). LDHA depletion (by shRNA) led to significantly reduced primary and metastatic tumor growth. In nude mice, if primary tumors were allowed to grow, these tumors (NC and LDHA KD) quickly reached 1000-2000mm^3 and had to be sacrificed within 21-28 days after tumor inoculation. In contrast, if primary tumors were resected at an early stage (when tumors reached 100-200 mm^3), mice showed extended survival, but eventually all mice succumbed to metastatic disease. Although LDHA KD primary and metastastic tumors grew slower than controls, all mice that initially harbored NC or LDHA KD tumors eventually died, with a survival difference of 2 weeks between mice in the NC vs. LDHA KD groups ((103) and Figure 3.6C).

While initially performed in immuno-compromised nude mice, follow-up experiments in the laboratory were performed in WT immuno-competent Balb/C mice. As before, 4T1 NC and LDHA KD tumor cells were implanted orthotopically in the mammary fat pad, and tumors were surgically resected when they reached approximately 200mm^3. After surgery, weekly BLI was performed to determine metastatic spread (Figure 3.6D). In this setting, all mice that initially harbored 4T1 NC tumors quickly developed metastasis and eventually died of their disease, as

in the immuno-compromised setting (Figure 3.6E). In contrast, in Balb/C mice that were inoculated with 4T1 LDHA KD tumors, followed by surgical resection of primary tumors, 40% of mice never developed any metastasis and were effectively cured of their highly aggressive disease (Figure 3.6D-E). This difference in survival benefit of LDHA depletion specifically in Balb/C mice, but not in nude mice, supported our hypothesis that LDHA depletion in tumor cells may create a less hostile TME, which may allow immune cells to better infiltrate these solid tumors and better control tumor growth.

To study how tumor-cell LDHA depletion affected the tumor microenvironment (TME), we stained the tumors that were surgically resected in the experiment described above and stained them for a number of markers (**Figure 3.7**). We found that 4T1 LDHA KD tumors showed significantly reduced angiogenesis and vascularity (as marked by CD31), reduced necrosis, and reduced TAM density compared to controls (Figure 3.7A-B). Further, while 4T1 NC tumors generally showed a large accumulation of T-cells (CD3- and CD4-positive) in their periphery, the interior core of NC control tumors showed very few CD3/CD4-positive T-cells. In contrast, LDHA KD tumors showed a high density of T-cells both in the tumor margin and the interior core (Figure 3.7C-E). Lastly, we found a strong and significant negative correlation between the levels of angiogenesis and the density of T-cells within individual regions of tumors (Figure 3.7F), in agreement with the known role for lactate in both upregulating VEGF expression (104) and inhibiting T-cell function and viability (Section 1.2.2).

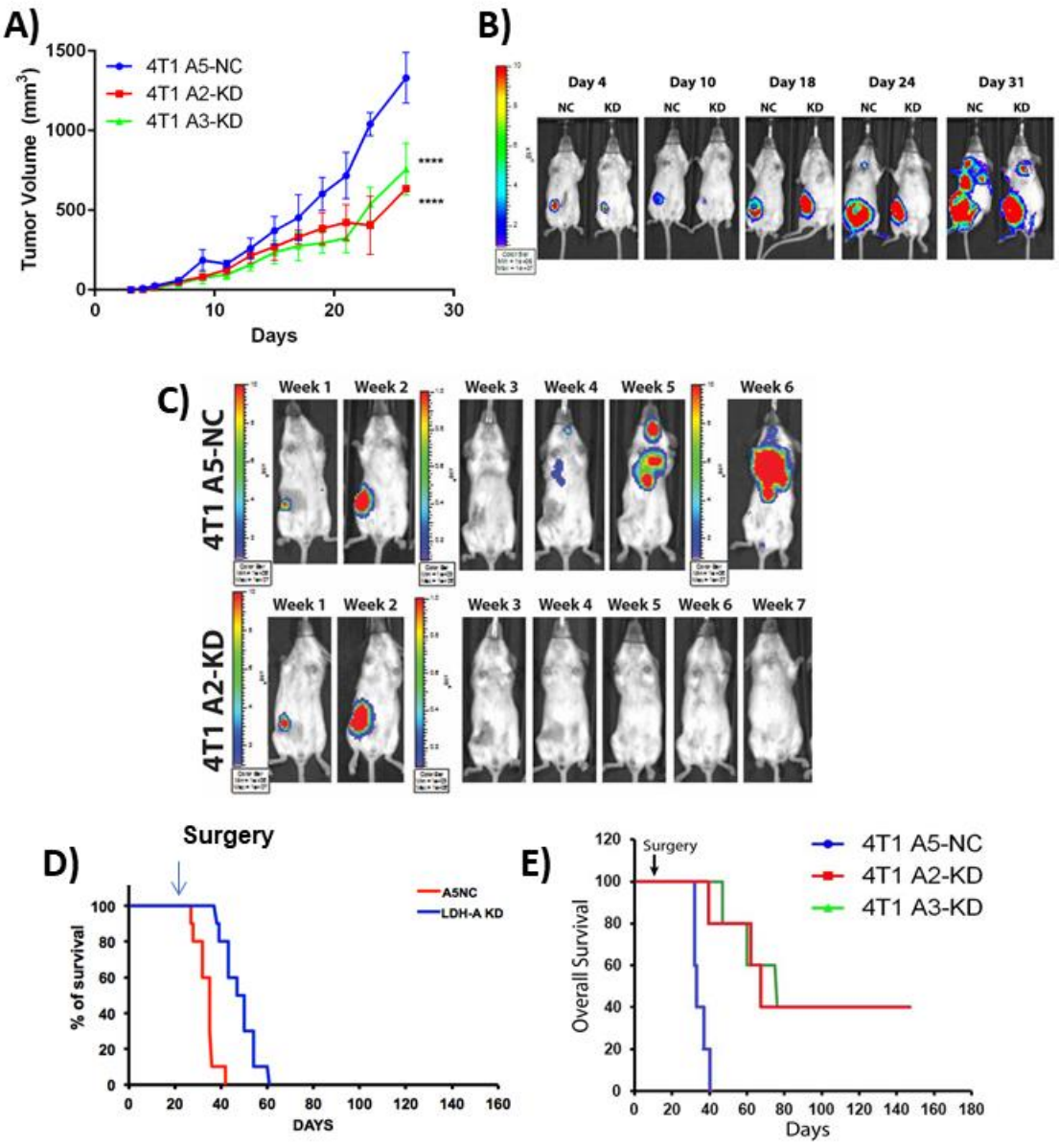
A)
Tumor Volume (mm3)
1500
1000
500
0
0
10
20
30
Days
4T1 A5-NC
4T1 A2-KD
4T1 A3-KD
****
****
B)
Day 4
Day 10
Day 18
Day 24
Day 31
NC
KD
C)
4T1 A5-NC
Week 1
Week 2
Week 3
Week 4
Week 5
Week 6
4T1 A2-KD
Week 1
Week 2
Week 3
Week 4
Week 5
Week 6
Week 7
D)
Surgery
% of survival
100
80
60
40
20
0
0
20
40
60
80
100
120
140
160
DAYS
A5NC
LDH-A KD
E)
Surgery
Overall Survival
120
100
80
60
40
20
0
0
20
40
60
80
100
120
140
160
180
Days
4T1 A5-NC
4T1 A2-KD
4T1 A3-KD

Figure 3.6. LDHA depletion in-vivo leads to decreased primary and metastatic tumor growth. A) $1x10^6$ Firefly luciferase-expressing 4T1 control (A5-NC) or LDHA KD (A2-KD, A3-KD) cells were injected orthotopically in the mammary fat pad of Balb/C mice, and primary tumor growth was measured by caliper. **B)** Mice from A) were imaged weekly for up to 8 weeks with bioluminescence imaging to detect their primary and metastatic tumor growth. **C)** BLI imaging of the 4T1 surgical model. Primary tumors were surgically resected on Day 10-13 (Week 2) of tumor growth, and mice were imaged weekly to observe the development of metastatic outgrowths. **D-E)** Overall survival of mice in the 4T1 surgical model in immuno-compromised nude mice (D) and in immuno-competent Balb/C mice (E). *This work was performed in the Blasberg laboratory by Dr. Inna Serganova (see 95, 103).*

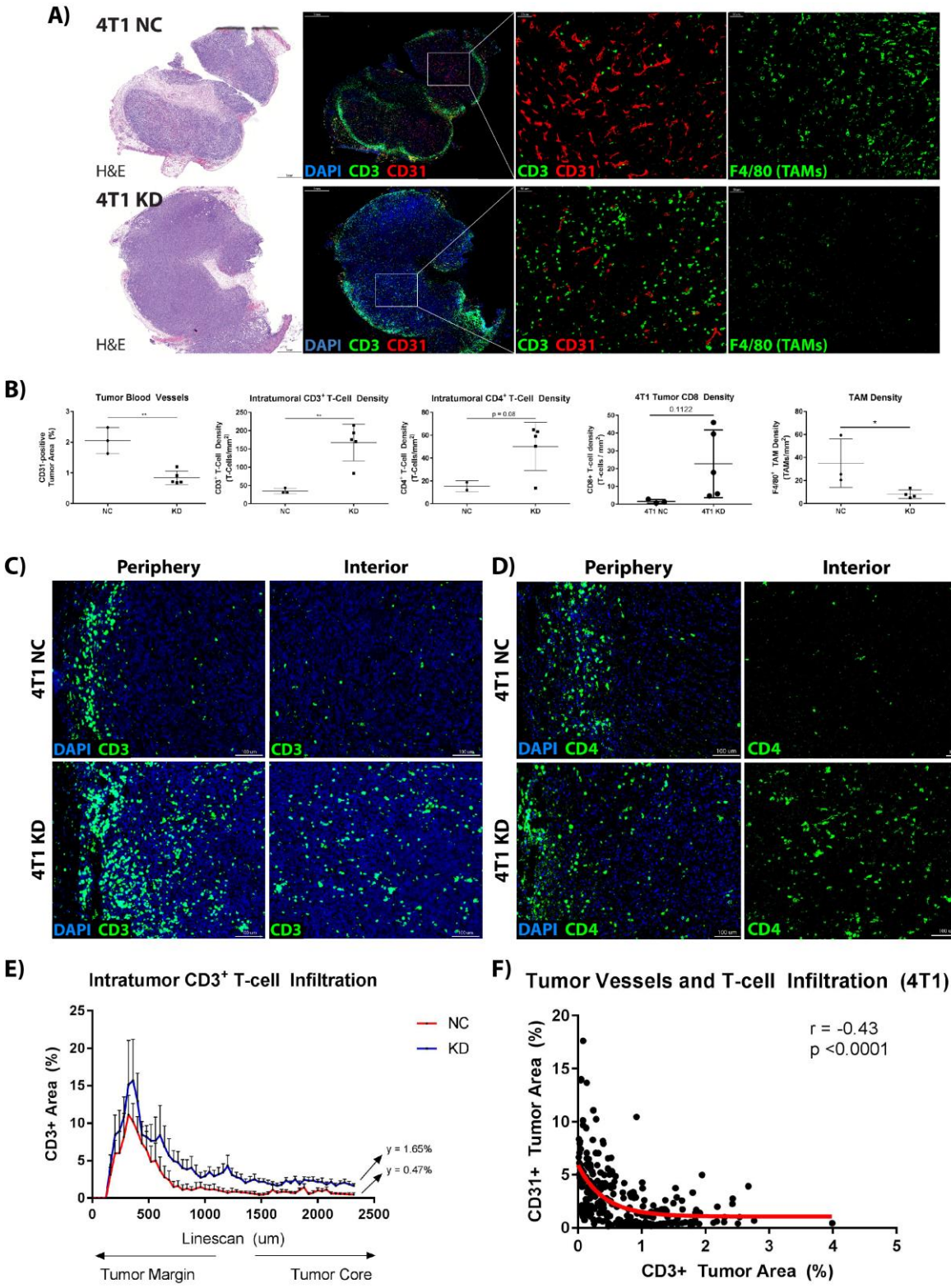
A)
4T1 NC
H&E
DAPI CD3 CD31
CD3 CD31
F4/80 (TAMs)
4T1 KD
H&E
DAPI CD3 CD31
CD3 CD31
F4/80 (TAMs)
B)
Tumor Blood Vessels
Intratumoral CD3+ T-Cell Density
Intratumoral CD4+ T-Cell Density
4T1 Tumor CD8 Density
TAM Density
NC
KD
C)
Periphery
Interior
4T1 NC
4T1 KD
DAPI CD3
CD3
D)
Periphery
Interior
4T1 NC
4T1 KD
DAPI CD4
CD4
E)
Intratumor CD3+ T-cell Infiltration
CD3+ Area (%)
NC
KD
y = 1.65%
y = 0.47%
Linescan (um)
Tumor Margin
Tumor Core
F)
Tumor Vessels and T-cell Infiltration (4T1)
r = -0.43
p <0.0001
CD31+ Tumor Area (%)
CD3+ Tumor Area (%)

Figure 3.7. Depletion of LDHA in 4T1 tumor cells alters the tumor microenvironment. A-B) Tumors that were resected in the 4T1 surgical model experiments (Figure 3.6) were stained for H&E and the indicated markers, and then quantified. **C-D)** Representative images of 4T1 NC and KD tumors stained for CD3 (C) and CD4 (D), showing the differences in T-cell accumulation in the tumor periphery vs. interior core. **E)** Quantification of CD3+ T-cell infiltration into tumor cores in NC and KD tumors, from C). **F)** Quantification of the relationship between tumor angiogenesis (CD31) and T-cell infiltration (CD3) in multiple ROIs from multiple tumors. *This work was performed in the Blasberg laboratory largely by Dr. Inna Serganova (see 95).*

3.2.5 Immune checkpoint blockade in the control vs. LDHA-depleted tumors

Having discovered that LDHA depletion in tumor cells leads to a more hospitable TME for infiltrating T-cells, we further hypothesized that combination of LDHA depletion in tumor cells, in addition to immune checkpoint blockade, may result in increased survival and the number of cures in our 4T1 model. To test this hypothesis, we followed a similar experimental plan as described above, but with the addition of treatment of mice with control IgG antibodies, or with anti-CTLA4 antibodies. Initial experiments revealed that anti-CTLA4 treatment reduced primary tumor growth in the NC but not the KD setting (**Figure 3.8A**), but the metastatic progression to the lungs was robustly reduced in mice bearing LDHA KD tumors + anti-CTLA4 treatment (Figure 3.8B-C). In further experiments, we followed our more clinically-relevant model of surgical resection of primary tumors, and found that the metastasis-free and overall survival of mice in the LDHA KD + anti-CTLA4 combination treatment was dramatically improved compared with either LDHA KD or anti-CTLA4 alone, with 75% of mice initially bearing KD tumors showing long term survival, compared to 33% of mice in the NC group (Figure 3.8D).

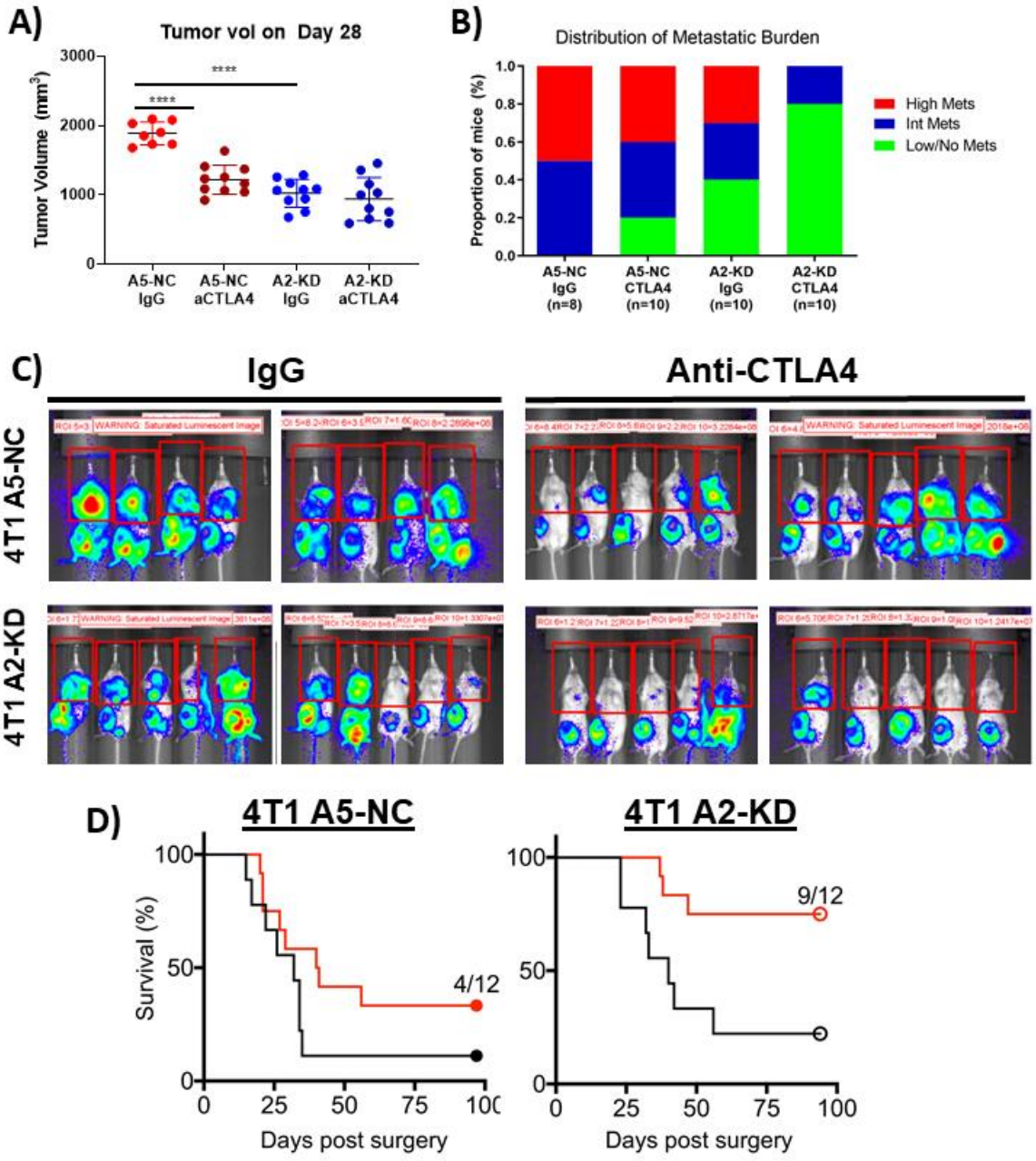

Figure 3.8. LDHA depletion improves the efficacy of immune checkpoint blockade. A) 4T1 NC or KD were injected orthotopically into Balb/C mice and treated with IgG or anti-CTLA4 therapy on Days 3, 6 and 9. Tumor volumes on Day 28 are shown. **B-C)** Quantification (B) and visualization (C) of metastatic tumor growth in the thorax of mice from A). **D**) In the surgical resection 4T1 model, mice were inoculated and treated as in A), but primary tumors were resected on Day 10 (NC) and Day 13 (KD), when tumors were approximately 200mm3. The survival of mice was followed for up to 100 days after surgery. *Black* is IgG- and *red* is anti-CTLA4-treated group. *This work was a major collaboration between the Blasberg and Wolchok laboratories (unpublished data).*

3.2.6 *In-vitro* MCT1/4 inhibition inhibits tumor glycolysis and improves T-cell function in the presence of lactate

To attempt to develop a more clinically translatable approach, we wanted to use small molecule inhibitors to target lactate synthesis or export from tumor cells into the extracellular compartment. To achieve this, we tested 2 compounds from Nirogyone Therapeutics, NGY-008 and NGY-066, which require DMSO for aqueous solubilization. These compounds are used as inhibitors of MCT1 (NGY-008) and dual MCT1/MCT4 inhibitors (NGY-066) (**Figure 3.9A**). We tested the effects of these compounds in our 4T1 cell line and found that while they only slightly inhibited cell proliferation *in-vitro* (Figure 3.9B), they strongly inhibited the secretion of lactate from tumor cells. We incubated 4T1 cells with DMSO or the NGY small molecules inhibitors and measured extracellular glucose and lactate by NMR spectroscopy. This revealed a highly altered lactate/glucose ratio in NGY-treated cells (Figure 3.9C). Further, treatment with these compounds over 72hrs led to a robust inhibition of extracellular acidification in Seahorse experiments, especially with NGY-066 (Figure 3.9D). This is especially interesting given that NGY-066 had little effect on 4T1 tumor cell proliferation in similar conditions. This suggests that 4T1 cells are highly plastic in their metabolism and can adapt to different metabolic phenotypes to sustain cell proliferation when blocking lactate export.

To determine if NGY treatment could rescue the effects of extracellular lactic acid on T-cell function, we cultured T-cells in the presence of increasing amounts of lactic acid (as in Figure 3.2), and in the presence of DMSO or the

NGY inhibitors (10uM). We cultured T-cells in this manner for 48 hrs and performed FACS to determine their activation status. We found that addition of lactic acid to the media resulted in significantly reduced T-cell proliferation and expression of activation markers (CD25 and PD-1), as before (**Figure 3.10A**). Addition of NGY inhibitors to the media did not increase T-cell proliferation when compared to DMSO controls, but it robustly increased the expression levels of activation markers in the presence of lactic acid, in comparison to DMSO-treated cells. This data suggests that inhibition of MCT1/4 on T-cells may protect against the immune-suppressive effects of lactic acid.

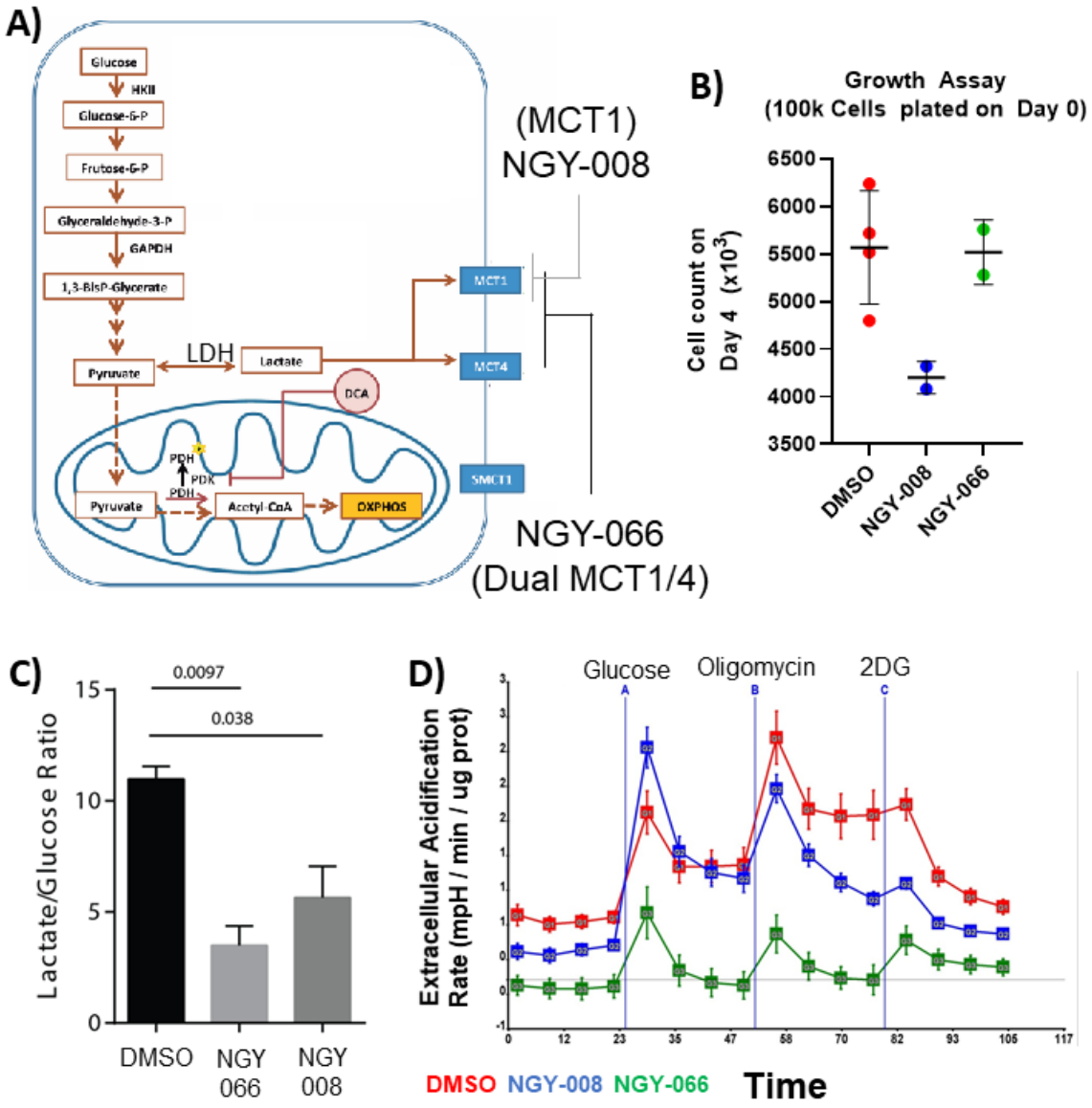
A)
Glucose
HKII
Glucose-6-P
Fructose-6-P
Glyceraldehyde-3-P
GAPDH
1,3-BisP-Glycerate
LDH
Lactate
Pyruvate
DCA
PDH
PDK
PDH
Pyruvate
Acetyl-CoA
OXPHOS
MCT1
MCT4
SMCT1
(MCT1)
NGY-008
NGY-066
(Dual MCT1/4)
B)
Growth Assay
(100k Cells plated on Day 0)
Cell count on Day 4 (x10^3)
6500
6000
5500
5000
4500
4000
3500
DMSO
NGY-008
NGY-066
C)
Lactate/Glucose Ratio
0.0097
0.038
15
10
5
0
DMSO
NGY 066
NGY 008
D)
Glucose
Oligomycin
2DG
A
B
C
Extracellular Acidification Rate (mpH / min / ug prot)
0
12
23
35
47
58
70
82
93
105
117
DMSO NGY-008 NGY-066
Time

Figure 3.9. MCT1/4 inhibition in tumor cells decreases extracellular lactate. A) Schematic of the glycolytic pathway with an emphasis in the last step; i.e., lactate export catalyzed by either MCT1 or MCT4. NGYs are small molecule inhibitors that target one or both MCT transporters. **B)** 100k 4T1 cells were plated on Day 0 in a 6-well plate, and cells were allowed to attach and rest for 24hrs. Then, on Day 1, 10uM of NGY-008 or NGY-066 (or DMSO) was added to cells. Media with DMSO or NGY small molecules was replenished on Day 3, and the number of living cells were counted on Day 4 (72hrs of drug incubation). **C)** In a separate experiment, 3,000 4T1 cells were plated in a 96-well plate on Day 0 and allowed to rest for 24hrs. This was followed by a 72hr incubation with the indicated compounds (10uM) or DMSO. The extracellular media was analyzed by NMR spectroscopy and the ratio of lactate/glucose is reported, indicating a decrease in lactate with both NGY compounds. **D)** 25,000 4T1 cells were plated in a 96-well plate on Day 0. On Day 1, DMSO or NGY small molecules were added to the cells, and Seahorse Extracellular Flux Analysis was performed 72hrs later.

To more accurately reflect the conditions found in tumors, we co-cultured T-cells with 4T1 A5NC cells for 48 hrs and measured T-cell proliferation and cytokine release. We found that addition of 4T1 tumor cells to the culture strongly reduced T-cell proliferation and release of the inflammatory cytokines IFNg and TNFa (Figure 3.10B, C). To determine whether NGY treatment could rescue the immune-suppressive effects of 4T1 cells during co-culture experiments with T-cells, we cultured T-cells alone or in co-culture with 4T1 cells, in the presence DMSO (control) or NGY-008 or NGY-066 (10 uM). The addition of 4T1 cells to the T-cell culture leads to a sharp decrease in T-cell proliferation (Figure 3.10B), likely due to the high metabolic rate of 4T1 cells that may lead to glucose depletion as well as lactate accumulation, among other possible factors. Interestingly, addition of NGY-066 to the co-culture media partially rescued this effect, with T-cells showing a significantly increased proliferation in this condition. To further assess the potential for MCT1/4 inhibition on improving T-cell function, we also measured the amount of secreted inflammatory cytokines (IFNg and TNFa) at the end of the 48hr co-culture experiment described (Figure 3.10C). We found that while treatment with the NGY inhibitors led to a modest but significant decrease in cytokine production when T-cells were cultured alone, these inhibitors partially or completely rescued the immune-suppressive effects of co-culture with 4T1 cells.

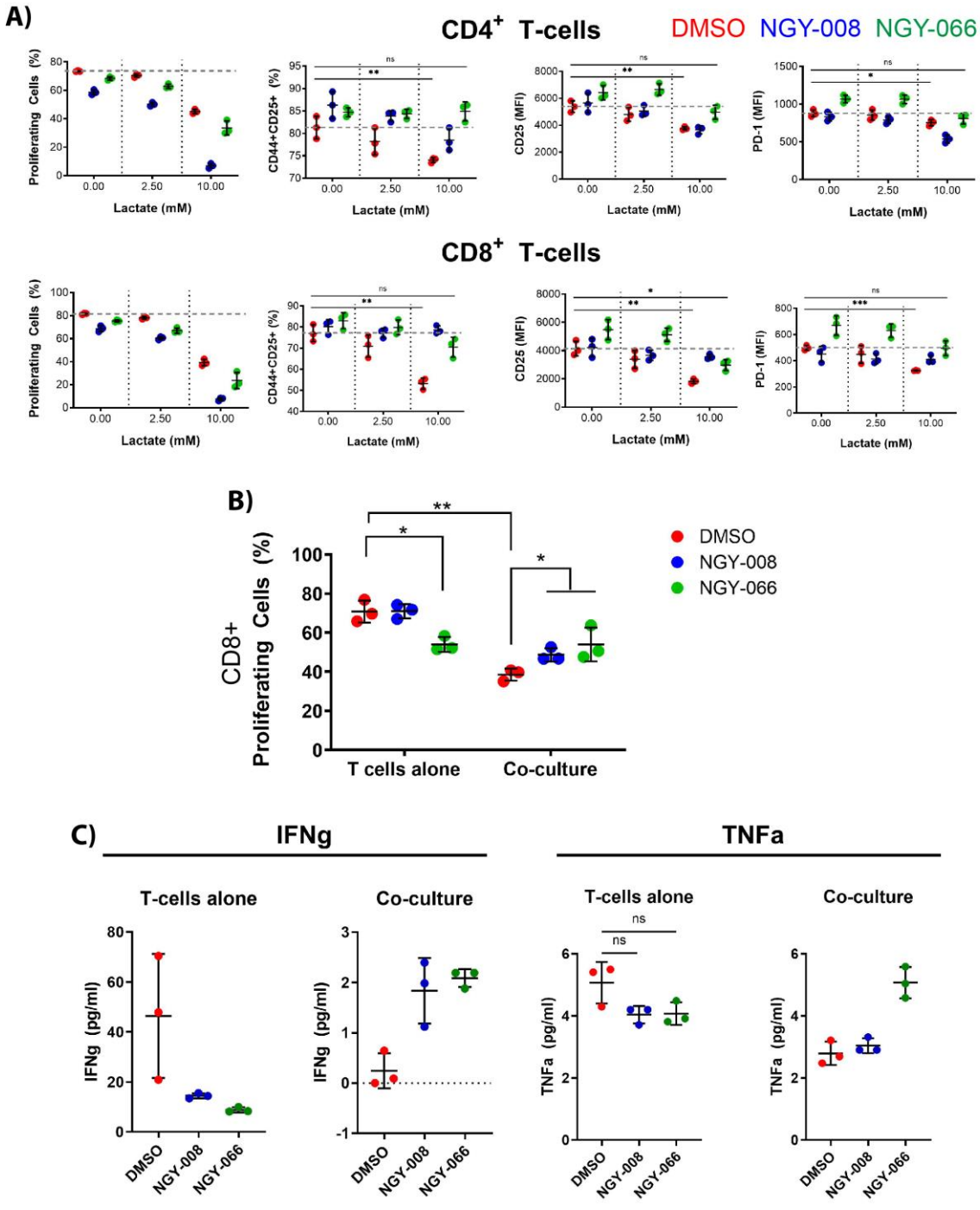
A)
CD4+ T-cells
DMSO NGY-008 NGY-066
Proliferating Cells (%)
CD44+CD25+ (%)
CD25 (MFI)
PD-1 (MFI)
Lactate (mM)
CD8+ T-cells
B)
CD8+ Proliferating Cells (%)
DMSO
NGY-008
NGY-066
T cells alone
Co-culture
C)
IFNg
TNFa
T-cells alone
Co-culture
IFNg (pg/ml)
TNFa (pg/ml)
ns

Figure 3.10. MCT1/4 Inhibition rescues the immune-suppressive effects of lactic acid. A) T-cells were incubated in increasing concentrations of lactic acid (0-10 mM), in addition to either DMSO or the NGY inhibitors (at 10uM) for 48 hrs, and analyzed by FACS. Horizontal grey dotted bar shows the mean of the DMSO-No lactate group, as a reference throughout the graphs. Results of t-tests for “DMSO-No Lac” vs. “DMSO-10mM Lac”, and “DMSO-No Lac” vs. “NGY-066-10mM Lac” are shown. **B)** T-cells were cultured alone or in co-culture with 4T1 A5NC cells, and treated with control (DMSO) or NGY inhibitors for 48hrs. The percentage of proliferating T-cells cells was quantified by FACS by selecting CFSElow T-cells. **C)** Supernatant from the co-culture experiments was analyzed by Luminex for the specified inflammatory cytokines. *This unpublished experiment was performed entirely by R. Zappasodi*.

3.2.7 Combination of immune checkpoint blockade with MCT1/4 inhibition *in-vivo*

Having shown that decreasing tumor-cell LDHA *in-vivo* can provide a strong benefit to immunotherapies *in-vivo*, we tested the hypothesis that inhibition of lactate transport across plasma membranes may improve the efficacy of immune checkpoint blockade. To test this hypothesis, we used our 4T1 model and our MCT inhibitors described above. We first determined whether treatment with either NGY-008 or NGY-066 (both at 10mg/kg) had any effect of primary tumor growth. We achieved this by injecting 4T1 A5-NC cells into the mammary fat pat of Balb/C mice, and starting treatment with Vehicle or NGY-008 or NGY-066 on Day 9, when tumors reached approximately $100mm^3$. We treated mice twice daily (due to instability of the compounds) until Day 18, and we found these compounds had no effect on primary tumor growth (**Figure 3.11A**). Given that NGY-066 almost completely blunted extracellular acidification of 4T1 tumor cells *in-vitro*, while NGY-008 did not show such a strong effect (Figure 3.9D), and that preliminary studies with NGY-008 *in-vivo* showed that NGY-008 may have pro-tumorigenic effects (data not shown), we selected NGY-066 (dual MCT1/4 inhibitor) for future *in-vivo* studies. Given our observation that LDHA depletion by shRNA from tumor cells led to a robust improvement in the efficacy of immune checkpoint blockade in our 4T1 model (Figure 3.8), we wanted to determine whether inhibiting lactate transport (via MCT1/4 inhibition) could also serve to boost the efficacy of immune checkpoint blockade. Following our 4T1 surgical resection model, we injected 4T1 A5-NC cells as before, and we treated with either Vehicle or NGY-066 twice daily on Days 3-9. Additionally, we also treated

with either IgG, anti-CTLA4 or anti-PD1 antibodies on Days 3, 6 and 9. On Day 10, when tumors were around 100-200mm^3, we surgically resected primary tumors and performed weekly BLI to detect metastatic progression and also observed mice for long-term survival. We found that treatment with NGY-066 alone provided a modest but short-term protection against metastasis formation (as indicated by decreased metastasis formation at Day 29; Figure 3.11B, C). However, NGY-066 alone did not provide long-term survival benefit to the mice (Figure 3.11D). Further, we found that treatment with immune checkpoint blockade alone also yielded small benefits on short-term metastasis formation and long-term survival. However, combination of NGY-066 plus anti-CTLA4 or anti-PD1 treatment provided both an initial benefit in terms of reduced metastasis burden (Figure 3.11B, C), as well as a modest improvement in the long-term survival of mice (Figure 3.11D). In fact, of the 60 mice in this experiment, the only 2 mice showing long-term survival were those treated with NGY-066 and immune checkpoint blockade. Thus, although all treatment was stopped at Day 9, this may have been enough the immune system to mount a system anti-tumor immune response.

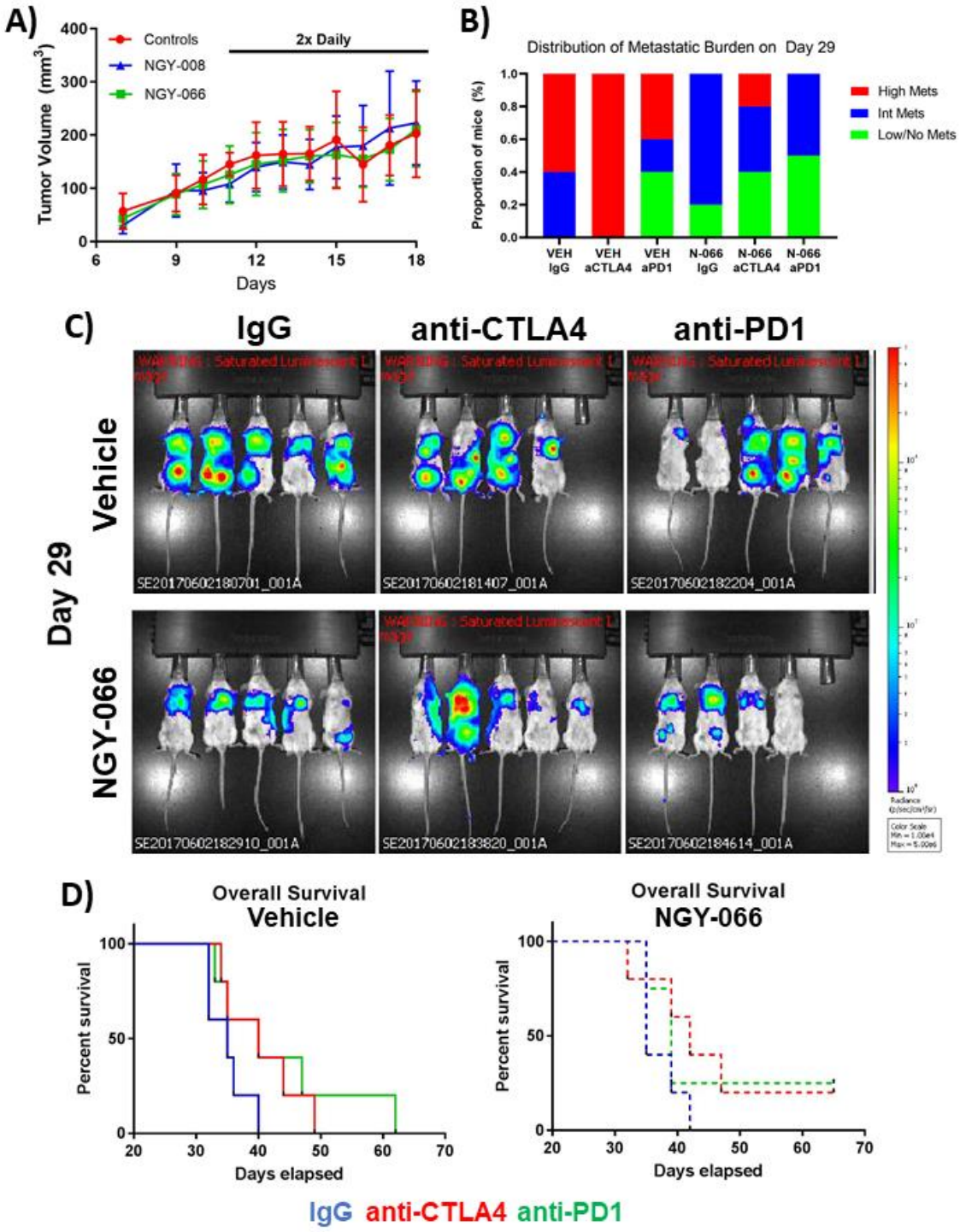
A)
Controls
NGY-008
NGY-066
2x Daily
Tumor Volume (mm3)
Days
B)
Distribution of Metastatic Burden on Day 29
Proportion of mice (%)
High Mets
Int Mets
Low/No Mets
VEH IgG
VEH aCTLA4
VEH aPD1
N-066 IgG
N-066 aCTLA4
N-066 aPD1
C)
IgG
anti-CTLA4
anti-PD1
Day 29
Vehicle
NGY-066
SE20170602180701_001A
SE20170602181407_001A
SE20170602182204_001A
SE20170602182910_001A
SE20170602183820_001A
SE20170602184614_001A
D)
Overall Survival
Vehicle
Overall Survival
NGY-066
Percent survival
Days elapsed
IgG anti-CTLA4 anti-PD1

Figure 3.11. MCT1/4 inhibition may improve the efficacy of immune checkpoint blockade. A) 1x10^6 4T1 A5-NC cells were injected into the mammary fat pad of Balb/C mice. Treatment with either Vehicle, or with NGY-008 or NGY-066 was performed twice daily on Days 11-18, and tumor volumes were measured by caliper. **B-C)** 4T1 A5-NC were injected as in A), mice were treated with either Vehicle or NGY-066 twice daily on Days 3-9, and additionally treated with either IgG, anti-CLTA4 or anti-PD1 antibodies on Days 3, 6 and 9. On Day 10, all primary tumors were surgically resected and BLI imaging was performed and thoracic tumor burden was quantified as shown, as per our '4T1 surgical resection model' (n = 5 mice per group). **D)** The overall survival of mice from B-C) was quantified and plotted. *This work was a collaboration between R. Zappasodi and I. Cohen (unpublished data).*

3.2.8 MCT1/4 inhibition during co-culture experiments enhances efficacy of CAR T-cells

The results above suggest that decreasing the amount of lactic acid in the extracellular environment can improve T-cell function. In order to determine whether this was true in other models of immunotherapy, we used the prostate cancer MycCAP model that was genetically modified to overexpres human PSMA (96). We cultured MycCAP PSMA+ NC or LDHA KD cells in the presence or absence of anti-PSMA CAR T-cells for 48hrs, and measured tumor cell death by staining for Annexin V and 7-AAD (**Figure 3.12**). We found that there was a modest increase in the percentage of apoptotic and dead cells when CAR T-cells were co-cultured with LDHA KD tumor cells vs. control tumor cells (66% increase in the percentage of dying cells in co-culture vs. mono-culture for A22-KD, vs a 32% difference in A5-NC; Figure 3.12A); however this did not reach statistical significance at alpha = 0.05. Furthermore, addition of NGY-066 during co-culture showed a significant increase in tumor cell killing compared to DMSO, and this effect was much stronger in the A5-NC setting compared to the A22-KD setting (2.87x fold increase in apoptotic/dead cells in the NGY-066 vs. DMSO conditions for A5-NC, compared to a 1.62x fold increase in the A22-KD setting). To further asses how LDHA depletion affects PSMA+ MycCAP tumor cell killing mediated by CAR T-cells, we performed a chromium release assay with MycCAP WT (PSMA-negative), and PSMA-positive A5-NC and A22-KD cells. After a 4hr incubation with CAR T-cells, we found that MycCAP WT cells showed minimal cell lysis, as expected. Further, at the highest effector (CAR T-cell) to target

(MycCAP tumor cells) ratio, we found a significant increase in cell lysis of MycCAP A22-KD cells compared to the A5-NC tumor cells (Figure 3.12B). These results suggest that decreasing lactate levels in the extracellular environment, either by depletion of LDHA or inhibition of lactate transporters, is an attractive strategy for improving the efficacy of CAR T-cells.

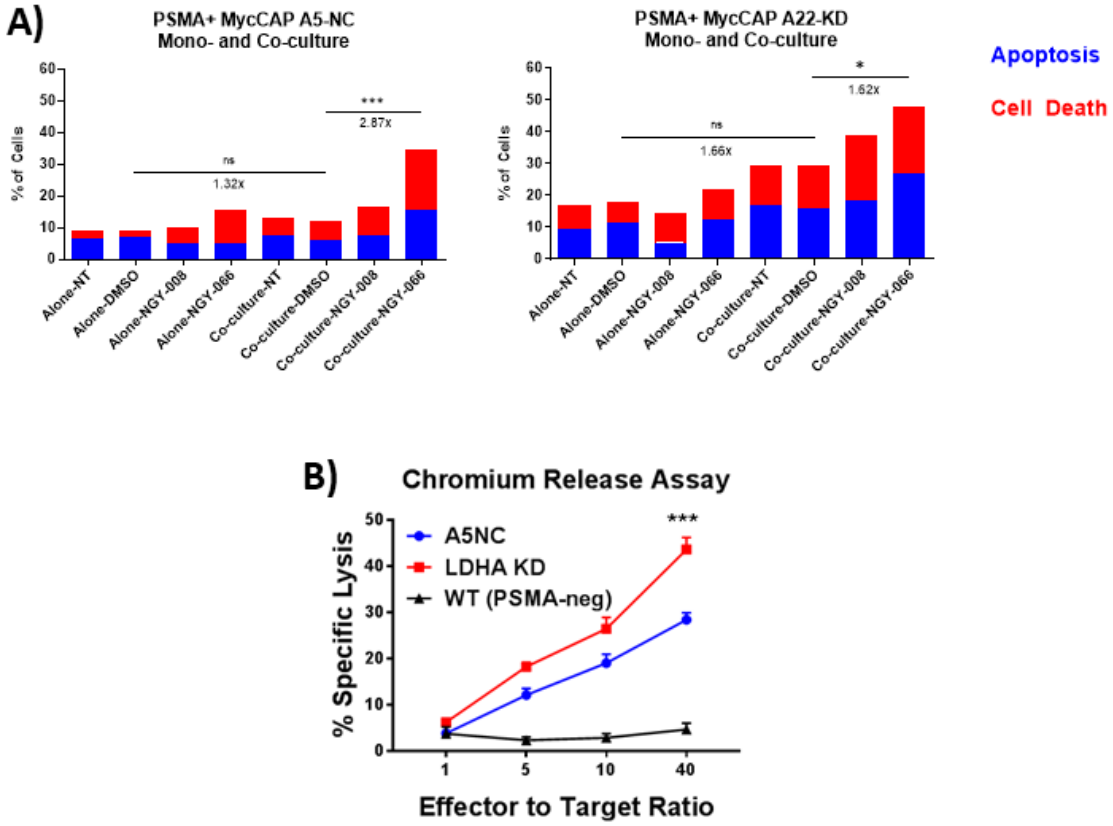

Figure 3.12. PSMA-targeted CAR T-cell killing is enhanced in the LDHA-depleted and MCT1/4-inhibited setting. A) PSMA-positive A5-NC or A22-KD MycCAP tumor cells were cultured alone or co-cultured with anti-PSMA CAR T-cells for 48hrs in the presence or absence of NGY inhibitors (10uM). Negative controls include Not-treated (NT) or DMSO-treated conditions. Apoptosis and tumor cell death was assessed by Annexin-V/7AAD staining. **B)** PSMA-positive (A5-NC, A22-KD) or –negative (WT) MycCAP cells were incubated for 4hrs with anti-PSMA CAR T-cells at different effector to target ratios (T-cell:Tumor cell ratio), and chromium release from tumor cells was measured as a measure of cytotoxicity. *This work was a major collaboration between the Blasberg and Ponomarev laboratories (unpublished data).*

3.2.9 Efficacy of CAR T-cell therapy in control vs. LDHA-depleted tumors

To determine if depletion of LDHA from tumor cells could improve other forms of immunotherapy, we turned to the MycCAP prostate cancer model that we developed. Having observed modestly improved killing of tumor cells that were depleted of LDHA *in-vitro* (Figure 3.12), we tested the hypothesis that LDHA depletion form tumor cells *in-vivo* would improve the efficacy of anti-PSMA CAR T-cell therapy. To test this hypothesis, we grew MycCAP NC or LDHA KD tumors into SCID mice, as before (96). Once tumors reached around 50-100mm^3, we injected anti-PSMA CAR-Tcells and observed their trafficking and efficacy. In two initial experiments, we found that (i) CAR T-cells had a prolonged persistence in mice bearing LDHA KD mice, as evidenced by the increased BLI intensity of these mice (**Figure 3.13A, B, D**); (ii) CAR T-cells showed increased trafficking to LDHA KD tumors, as evidenced by *ex-vivo* BLI imaging of CAR T-cells (Renilla) (Figure 3.13B-C) and by *ex-vivo* flow cytometry (Figure 3.13E); and (iii) that while CAR T-cell therapy had little effect on the rate of tumor growth in the NC setting, LDHA KD tumors treated with CAR T-cells had a modest but significant decrease in their tumor growth compared to un-treated controls (Figure 3.13F). Although we obtained initially promising results, these experiments have been hard to replicate, possibly due to changes in PSMA expression over time, or due to antigen downregulation in LDHA KD cells and tumors.

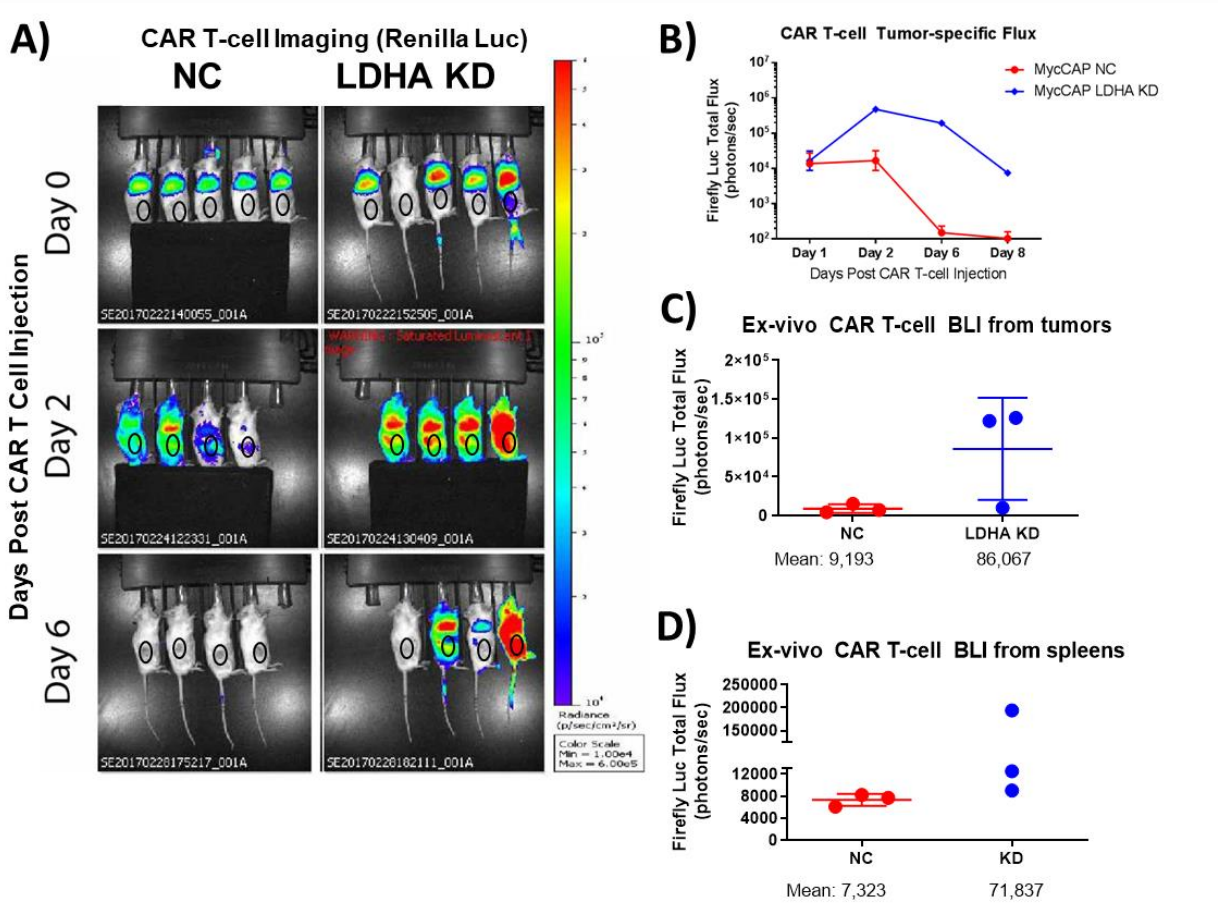
A)
CAR T-cell Imaging (Renilla Luc)
NC
LDHA KD
Days Post CAR T Cell Injection
Day 0
Day 2
Day 6
B)
CAR T-cell Tumor-specific Flux
MycCAP NC
MycCAP LDHA KD
Firefly Luc Total Flux (photons/sec)
Day 1
Day 2
Day 6
Day 8
Days Post CAR T-cell Injection
C)
Ex-vivo CAR T-cell BLI from tumors
Firefly Luc Total Flux (photons/sec)
NC
LDHA KD
Mean: 9,193
86,067
D)
Ex-vivo CAR T-cell BLI from spleens
Firefly Luc Total Flux (photons/sec)
NC
KD
Mean: 7,323
71,837
E)
MycCAP NC Tumor
MycCAP LDHA KD Tumor
RFP (T-cells)
GFP (Tumor cells)
0.50%
13.37%
4.65%
81.48%
11.12%
14.57%
8.45%
65.86%
% CAR T Cells
**
NC + CAR T Cells
LDH-A KD + CAR T Cells
F)
MycCAP Prostate Tumor Growth
Tumor Volume (mm3)
Days Post Tumor Cell Injection
MycCAP NC
MycCAP NC + CAR T-cells
MycCAP LDHA KD
MycCAP LDHA KD + CAR T-cells

Figure 3.13. LDHA depletion modestly improves the efficacy of anti-PSMA CAR T-cell therapy. A-B) $1x10^6$ MycCAP NC or LDHA KD tumor cells (carrying a GFP-Renilla Luc reporter) were inoculated in the right flank of SCID mice. After 7 days, $10x10^6$ anti-PSMA CAR T-cells (carrying an RFP-Firefly Luc reporter) were injected via the tail vein. BLI imaging was performed: (i) for tumor cells (Ren Luc) one day prior to CAR T-cell injection to localize the tumor area (black ovals), and (ii) at the indicated time points to visualize CAR T-cell (CBR Luc) trafficking and persistence over time (A). **B)** Quantification of the CAR T-cell localization to the tumor sites from the mice in (A). **C-D)** On Day 6 after CAR T-cell injection, a portion of mice were sacrificed, tumors extracted and the CAR T-cell BLI intensity was measured ex-vivo in tumors (C) and spleen (D). **E**) In a separate, but similar experiment, tumors were extracted on Day 6, and the number of GFP+ tumor cells and RFP+ CAR T-cells was quantified by flow cytometry (quantification in the *right* panel). This is quantified in the right panel. **F)** Tumor growth profiles of the mice from (A). *This work was a major collaboration between the Blasberg and Ponomarev laboratories (unpublished data).*

3.3 Summary

Chapter 3 of this study shows the clear direct effects of the inhibitory effect of lactic acid on T-cell function. We show that addition of lactic acid to T-cells inhibits their proliferation, activation, cytokine secretion and killing capacity. We also show that inhibition of tumor-cell derived lactate secretion, via either LDHA depletion or MCT1/4 inhibition, can enhance T-cell function in multiple in-vitro assays. We further demonstrate this effect *in-vivo*, with experiments showing that LDHA-depleted tumors are 5-10 fold more infiltrated by T-cells compared to controls (endogenous and CAR T-cells). LDHA-depleted tumors also respond significantly better to immune checkpoint blockade, and slightly better to CAR T-cell therapy. Lastly, MCT1/4 inhibition led to similar increase in T-cell function *in-vitro* and *in-vivo*, suggesting that this may be an attractive strategy for metabolic inhibition in the clinic.

CHAPTER 4

Inverse correlations between expression of glycolytic and immune-related markers in human tumors

4.1 Introduction

In Chapter 3, we demonstrated the causal relationship between lactate accumulation and immune suppression in-vitro. We also showed that LDHA depletion in tumors led to a robust increase in T-cell infiltration into solid murine breast cancer tumors, and that different types of immunotherapy had improved efficacy when LDHA was depleted from tumor cells in-vivo. In Chapter 4, we set out to determine whether the inverse relationships between tumor glycolysis and immune infiltration were also true in human tumors. While a limited number of published studies have addressed this question in a small number of tumor types using relatively small datasets, no extensive characterization of the relationship between tumor glycolysis and immune infiltration of solid tumors has been performed to the best of our knowledge. In this chapter, an initial analysis showed that there was an inverse correlation between tumor glycolysis and immune infiltration in breast cancer, and we then set out to characterize this relationship further in other solid tumor types.

4.2 Results

4.2.1 ImmScore, the immune signature

To determine whether increased tumor glycolysis results in immune exclusion in solid tumors, we conducted the reanalysis of gene expression and downloaded the entire Pan Cancer Atlas TCGA mRNA expression data set from the cBioPortal (www.cbioportal.org), consisting of more than 10,000 samples and 33 cancer types. We used this resource for analyzing gene expression (mRNA) and genomic mutations (DNA). We also downloaded all data from the Immune Landscape of cancer article from Thorsson, et. al.(53) This article separated all ~10,000 tumors into 6 discrete immune clusters associated with different immune-related phenomena, and it further provided measures of immune content and infiltration (by measuring leukocyte fraction via methylation analysis, and immune infiltration by image analysis of H&E-stained slides. Given our interest in lactic acid accumulation within the TME and the role this may play in regulating immune infiltration, we excluded leukemias and lymphomas (L-AML, THYM (thymoma), and DLBC (diffuse large B-cell lymphoma)), and further focused our study on tumor types with currently FDA-approved immunotherapies: melanoma (SKCM), lung (LUAD, LUSC), urothelial (BLCA), renal (RCC), head and neck (HNSC), hepatocellular (LIHC), gastric (stomach (STAD), esophageal (ESCA)), colorectal (COAD, READ), breast (BRCA), and cervical (CESC) cancers.

To obtain a measure of T-cell infiltration of solid tumors from gene expression data, we selected 4 classical genes that identify T-cells: CD3D, CD3E, CD8A, and LCK. We expected that mRNA abundance of these transcripts would be a measure of the T-cell infiltration of tumors. We tested this by plotting the correlation of our ImmScore with the Cytolytic Score (47) and Tumor

Inflammation Score (TIS) (54) and found a positive Pearson correlation of 0.89 and 0.92, respectively (**Figure 4.1A, B**). ImmScore also correlated well with the Leukocyte Fraction (calculated from methylation patterns) (53), to a similar extent as TIS and Cytolytic Score (**Figure 4.2A-C**), as well as with tumor-infiltrating lymphocyte counts as measured by pathologist scoring of H&E-stained slides (Figure 4.1C) (48). Further, Saltz, et. al. used artificial intelligence to analyze more than 5,000 H&E slides from TCGA patients and divided patients into different categories depending on the pattern of immune infiltration (55). ImmScore was significantly higher in the tumors infiltrated 'briskly' and 'diffusely' throughout the tumors, in comparison to those that were infiltrated 'non-briskly' and only 'focally' (Figure 4.1D).

4.2.2 The glycolysis signature GlyScore correlates with tumor metabolic activity

We sought to develop a gene signature that would serve as an indicator of the glycolytic potential of tumors. To develop a glycolysis signature, biological pathways from the Gene Ontology (GO), Reactome (RT), KEGG (KG) and Pathway Interactive Database (PID) that contained the phrases "glucose catabolism" or "glycolysis" in their name were chosen, and all the genes within these pathways were plotted to observe their correlation with each other (Figure 4.2D). Given that expression of 10/11 classical genes involved in the stepwise enzymatic breakdown of glucose to lactate (GPI, PFK, ALDOA, TPI, GAPDH, PGK, PGAM, ENO, PKM and LDHA; not HK2) highly correlated with each other, we included all these genes in a glycolysis signature, GlyScore (Figure 4.1E). To determine whether mRNA expression of GlyScore was associated with increased

protein expression of the selected genes, we additionally accessed the Clinical Proteomics Tumor Analysis Consortium (CPTAC) dataset within the cBioPortal for the available cancer type (breast, colonrectal and ovarian cancer). We plotted the correlation between mRNA and protein expression across all available tumors (n = 260) and found an overall significantly positive correlation between mRNA and protein expression, especially within breast and ovarian carcinoma samples (**Figure 4.3**).

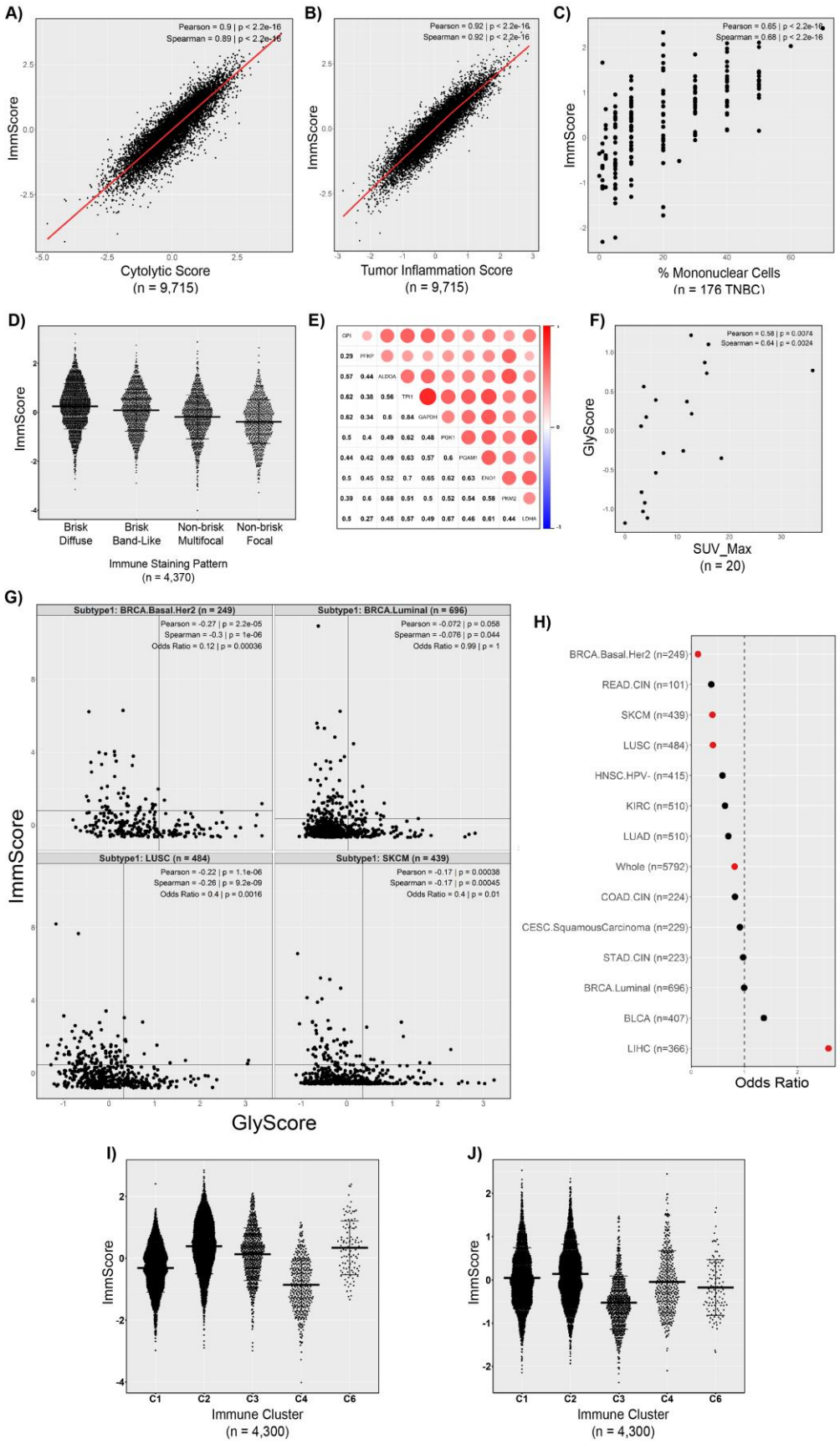
A)
Pearson = 0.9 | p < 2.2e-16
Spearman = 0.89 | p < 2.2e-16
ImmScore
Cytolytic Score
(n = 9,715)
B)
Pearson = 0.92 | p < 2.2e-16
Spearman = 0.92 | p < 2.2e-16
ImmScore
Tumor Inflammation Score
(n = 9,715)
C)
Pearson = 0.65 | p < 2.2e-16
Spearman = 0.68 | p < 2.2e-16
ImmScore
% Mononuclear Cells
(n = 176 TNBC)
D)
ImmScore
Brisk Diffuse
Brisk Band-Like
Non-brisk Multifocal
Non-brisk Focal
Immune Staining Pattern
(n = 4,370)
E)
GPI
PFKP
ALDOA
TPI1
GAPDH
PGK1
PGAM1
ENO1
PKM2
LDHA
F)
Pearson = 0.58 | p = 0.0074
Spearman = 0.64 | p = 0.0024
GlyScore
SUV_Max
(n = 20)
G)
Subtype1: BRCA.Basal.Her2 (n = 249)
Pearson = -0.27 | p = 2.2e-05
Spearman = -0.3 | p = 1e-06
Odds Ratio = 0.12 | p = 0.00036
Subtype1: BRCA.Luminal (n = 696)
Pearson = -0.072 | p = 0.058
Spearman = -0.076 | p = 0.044
Odds Ratio = 0.99 | p = 1
Subtype1: LUSC (n = 484)
Pearson = -0.22 | p = 1.1e-06
Spearman = -0.26 | p = 9.2e-09
Odds Ratio = 0.4 | p = 0.0016
Subtype1: SKCM (n = 439)
Pearson = -0.17 | p = 0.00038
Spearman = -0.17 | p = 0.00045
Odds Ratio = 0.4 | p = 0.01
ImmScore
GlyScore
H)
BRCA.Basal.Her2 (n=249)
READ.CIN (n=101)
SKCM (n=439)
LUSC (n=484)
HNSC.HPV- (n=415)
KIRC (n=510)
LUAD (n=510)
Whole (n=5792)
COAD.CIN (n=224)
CESC.SquamousCarcinoma (n=229)
STAD.CIN (n=223)
BRCA.Luminal (n=696)
BLCA (n=407)
LIHC (n=366)
Odds Ratio
I)
ImmScore
C1
C2
C3
C4
C6
Immune Cluster
(n = 4,300)
J)
ImmScore
C1
C2
C3
C4
C6
Immune Cluster
(n = 4,300)

Figure 4.1. Development and validation of ImmScore and GlyScore. **A, B)** We compared the expression of our ImmScore signature vs. the established Cytolytic signature (A) and Tumor Inflammation Score signature (TIS; B). **C)** ImmScore expression was plotted against the percentage of mononuclear cells (MN_Cells) in a subset of 181 TNBC tumors. **D)** ImmScore expression was plotted against the machine learning-derived immune staining patterns of more than 4,000 tumors. **E)** Cross-correlation plot of the glycolysis signature GlyScore across all 9,715 patients in our TCGA dataset. The bottom part shows the Pearson correlation coefficient and the top part shows color- and size-coded symobols reflecting the degree of correlation. **F)** In 20 primary breast cancer patients, GlyScore expression was plotted against each tumor's FDG-PET uptake. **G)** Mutual exclusiavity analysis between GlyScore and ImmScore was run for all cancer subtypes and the Odds Ratio (OR) is shown for each subtype. Significant results ($p < 0.05$) shown in red. **H)** Expression of GlyScore and ImmScore is shown (not log-scaled, for easier visualization) for selected cancer types that show significant mutual exclusivity between these signatures, as well as for Luminal breast cancer, which doesn't show significant exclusivity or co-occurrence. **I, J)** Expression of ImmScore (E) and GlyScore (F) across the 5 immune clusters described in Larsson, et al. Data from KIRC was excluded since it was an outlier.

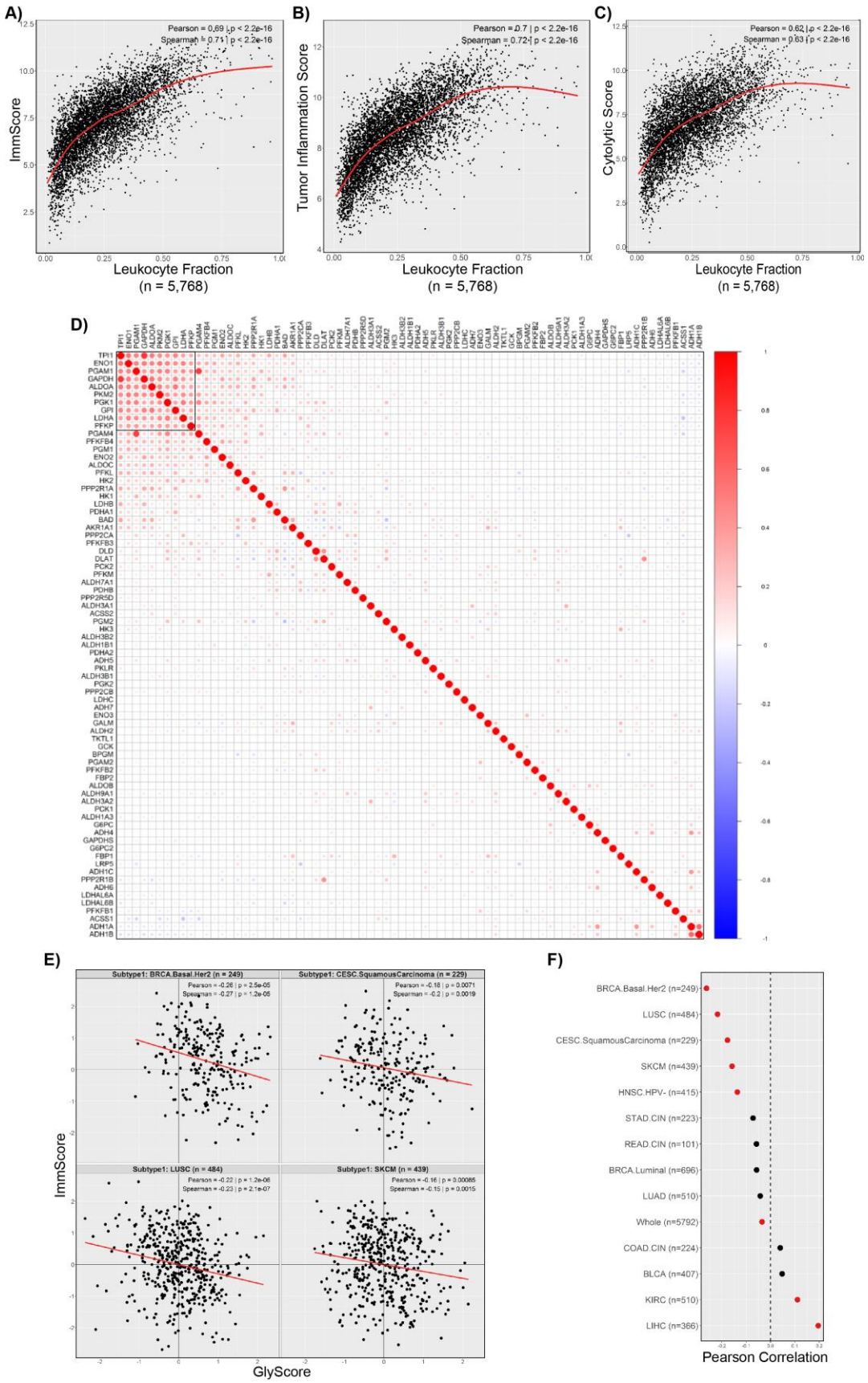
A)
Pearson = 0.69 | p < 2.2e-16
Spearman = 0.71 | p < 2.2e-16
ImmScore
Leukocyte Fraction
(n = 5,768)
B)
Pearson = 0.7 | p < 2.2e-16
Spearman = 0.72 | p < 2.2e-16
Tumor Inflammation Score
Leukocyte Fraction
(n = 5,768)
C)
Pearson = 0.62 | p < 2.2e-16
Spearman = 0.63 | p < 2.2e-16
Cytolytic Score
Leukocyte Fraction
(n = 5,768)
D)
E)
Subtype1: BRCA.Basal.Her2 (n = 249)
Pearson = -0.26 | p = 2.5e-05
Spearman = -0.27 | p = 1.2e-05
Subtype1: CESC.SquamousCarcinoma (n = 229)
Pearson = -0.18 | p = 0.0071
Spearman = -0.2 | p = 0.0019
Subtype1: LUSC (n = 484)
Pearson = -0.22 | p = 1.2e-06
Spearman = -0.23 | p = 2.1e-07
Subtype1: SKCM (n = 439)
Pearson = -0.16 | p = 0.00085
Spearman = -0.15 | p = 0.0015
ImmScore
GlyScore
F)
BRCA.Basal.Her2 (n=249)
LUSC (n=484)
CESC.SquamousCarcinoma (n=229)
SKCM (n=439)
HNSC.HPV- (n=415)
STAD.CIN (n=223)
READ.CIN (n=101)
BRCA.Luminal (n=696)
LUAD (n=510)
Whole (n=5792)
COAD.CIN (n=224)
BLCA (n=407)
KIRC (n=510)
LIHC (n=366)
Pearson Correlation

Figure 4.2. Further development and validation of ImmScore and GlyScore. A-C) We compared the expression of our ImmScore signature (A), TIS (B), and Cytolytic Score (C) against the leukocyte fraction estimation based on methylation analysis. **D)** Cross correlation plot (Pearson) from all 9,715 tumors in our dataset, with all genes from pathways relating to glucose catabolism and glycolysis. The top left corner (box) shows high degree of cross-correlation between 9/10 classical glycolytic genes. **E, F)** Linear correlations between GlyScore and ImmScore were calculated for individual cancer subtypes, and the Pearson coefficient is shown. Significant results ($p < 0.05$) shown in red.

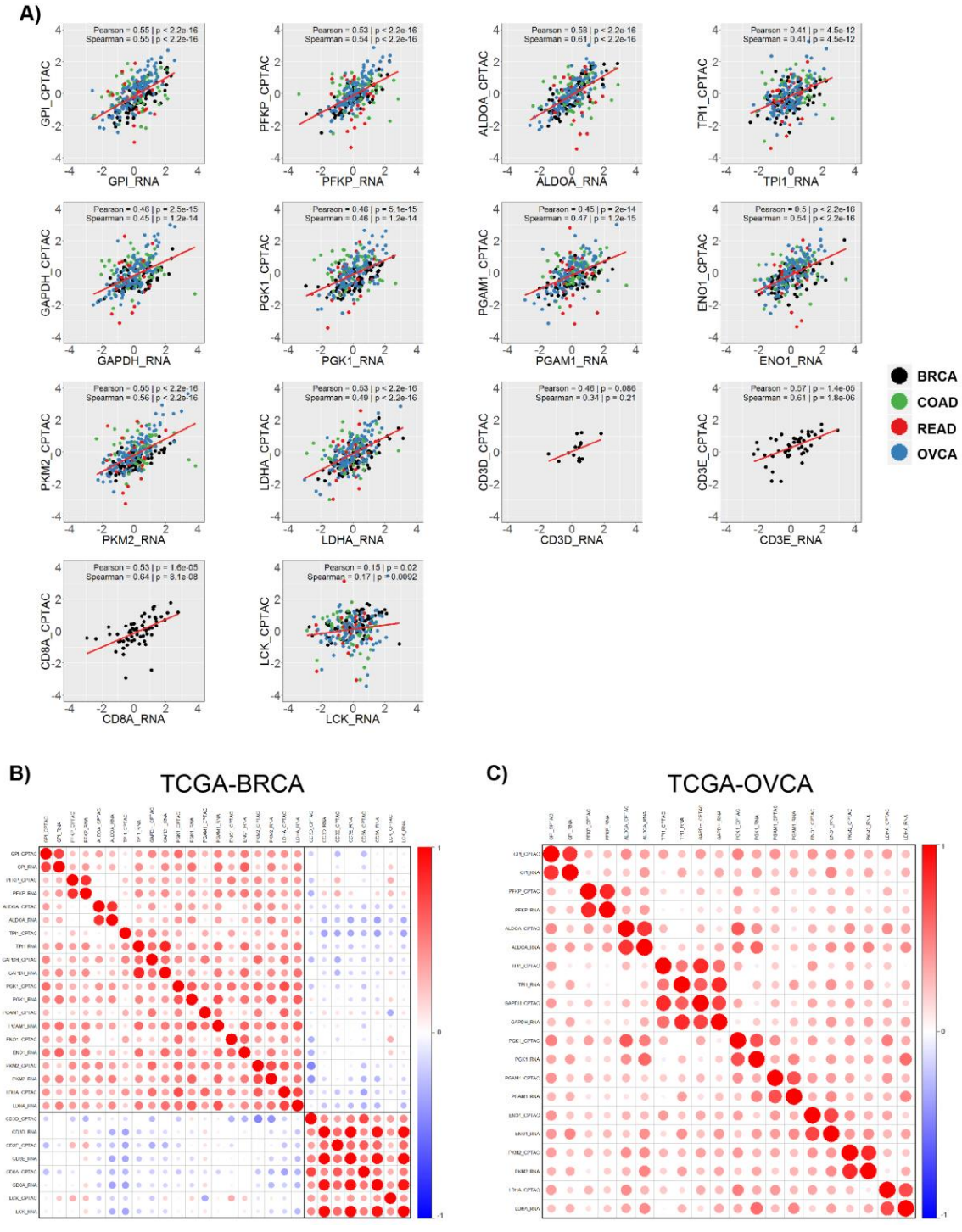
A)
GPI_CPTAC
GPI_RNA
Pearson = 0.55 | p < 2.2e-16
Spearman = 0.55 | p < 2.2e-16
PFKP_CPTAC
PFKP_RNA
Pearson = 0.53 | p < 2.2e-16
Spearman = 0.54 | p < 2.2e-16
ALDOA_CPTAC
ALDOA_RNA
Pearson = 0.58 | p < 2.2e-16
Spearman = 0.61 | p < 2.2e-16
TPI1_CPTAC
TPI1_RNA
Pearson = 0.41 | p = 4.5e-12
Spearman = 0.41 | p = 4.5e-12
GAPDH_CPTAC
GAPDH_RNA
Pearson = 0.46 | p = 2.5e-15
Spearman = 0.45 | p = 1.2e-14
PGK1_CPTAC
PGK1_RNA
Pearson = 0.46 | p = 5.1e-15
Spearman = 0.46 | p = 1.2e-14
PGAM1_CPTAC
PGAM1_RNA
Pearson = 0.45 | p = 2e-14
Spearman = 0.47 | p = 1.2e-15
ENO1_CPTAC
ENO1_RNA
Pearson = 0.5 | p < 2.2e-16
Spearman = 0.54 | p < 2.2e-16
PKM2_CPTAC
PKM2_RNA
Pearson = 0.55 | p < 2.2e-16
Spearman = 0.56 | p < 2.2e-16
LDHA_CPTAC
LDHA_RNA
Pearson = 0.53 | p < 2.2e-16
Spearman = 0.49 | p < 2.2e-16
CD3D_CPTAC
CD3D_RNA
Pearson = 0.46 | p = 0.086
Spearman = 0.34 | p = 0.21
CD3E_CPTAC
CD3E_RNA
Pearson = 0.57 | p = 1.4e-05
Spearman = 0.61 | p = 1.8e-06
CD8A_CPTAC
CD8A_RNA
Pearson = 0.53 | p = 1.6e-05
Spearman = 0.64 | p = 8.1e-08
LCK_CPTAC
LCK_RNA
Pearson = 0.15 | p = 0.02
Spearman = 0.17 | p = 0.0092
BRCA
COAD
READ
OVCA
B)
TCGA-BRCA
C)
TCGA-OVCA

Figure 4.3. Positive correlations between mRNA and protein expression. A) mRNA and protein expression data from 4 TCGA cancer types (breast, colon, rectal, ovarian); we downloaded and performed a correlation between mRNA and protein expression of the 10 genes selected for GlyScore and the 4 genes selected for ImmScore. The data was plotted across the 260 samples for which both types of data were available. **B)** The same data was plotted for two selected cancer types (BRCA and OVCA) using a cross-correlation plot.

We posited that tumors with a high GlyScore would also display increased glucose uptake and metabolic activity. To test this hypothesis we conducted gene expression analysis of 20 breast tumors of patients who underwent FDG-PET imaging at our Institution between 2001 and 2004 (56). Our analyses revealed a strong correlation between GlyScore expression and fluorodeoxyglucose (FDG) uptake, as measured by maximum Standarized Uptake Value (SUVmax) (Figure 4.1F).

4.2.3 Relationships between GlyScore and ImmScore in select tumor types

Next, we sought to determine whether expression of glycolysis-related genes would correlate with tumor immune infiltration. We focused our analysis on tumors with currently-approved immune checkpoint blockade (ICB) by the FDA, given that he typical response rate to ICB in these tumor types is ~25% (Table 1), leaving the majority of patients without clinical benefit from ICB. We assessed he relationship between GlyScore and ImmScore in a number of ways. We first tested for direct linear correlations between GlyScore and ImmScore in the selected cancer types. Due to the inherent heterogeneity of cancer types with multiple subtypes, we analyzed each subtype separately and plotted the subtypes with the most significant changes. Our analyses revealed significant negative correlations between GlyScore and ImmScore in triple negative breast cancer (TNBC) and HER2-positive breast cancer, lung squamous carcinoma, cervical carcinoma and melanoma (Figure 4.2E-F).

Next, we modified our analysis to reflect the potential mutual exclusivity between tumor glycolysis and immune infiltration. We hypothesized that the linear correlations between tumor glycolysis and immune infiltration may be weak due to (i) the inherent caveats in measuring gene expression rather than true metabolic activity and immune infiltration; and (ii) the possibility that tumor glycolysis might only affect immune infiltration once a threshold of metabolic activity/expression is reached. To address these issues, we set a threshold for each signature at half a standard deviation away from the mean of each signature within each cancer type. We categorized tumors as displaying 'increased tumor glycolysis' if its GlyScore was >half a standard deviation away from the mean within that cancer type (Z-score >0.5). Likewise, a tumor was considered to show 'robust immune infiltration' if its ImmScore expression value was >half a standard deviation away from the mean within that cancer type. We chose this cutoff because it separated tumors roughly into those with the top third highest expression level vs. those with lower 2/3's of expression. This allowed sufficient number of tumors in both the 'top third' vs. 'bottom two thirds' groups to allow meaningful statistical analysis. We ran mutual exclusivity analysis, which revealed that many cancer types showed statistically significant mutual exclusivity (Odds Ratio (OR) lower than 1) between GlyScore and ImmScore (Figure 4.1G-H).

4.2.4 Association of GlyScore and Immune Cluster 3

The Immune Landscape article from the TCGA revealed a clustering of all ~10,000 tumors into 6 immune-related clusters/subtypes, associated with

different immune-related gene expression patterns (53). These are associated with expression of (1) wound healing, (2) IFN-gamma signaling, (3) active inflammation, (4) lymphocyte depleted, (5) immunologically quiet, and (6) TGF-beta dominant (immune suppressive) gene expression patterns. In this article, the authors showed that cluster 3 is highly associated with an active inflammatory response and prolonged survival of patients across different cancer types. We found that expression of our ImmScore signature was highest in the immunologically dominant clusters (Clusters 2, 3, and 6), in agreement with our results from (Figure 4.1I). Interestingly, expression of our glycolysis signature, GlyScore, was significantly decreased in Cluster 3 – the cluster that was associated with the most active inflammatory phenotype and improved patient survival (Figure 4.1I-J).

4.2.5 GlyScore expression is associated with lower-than-expected ImmScore

A major goal of this analysis was to determine if glycolysis was associated with immune exclusion from solid tumors. The degree of immune infiltration, however, depends on many factors that were not taken into account in our analysis thus far. We hypothesized that two main factors that may contribute to immune infiltration are the number of neoantigens arising from the tumor, and the antigen-presentation capacity of tumors. Exploratory analysis into this hypothesis revealed that, as previously reported (57, 58), mutation or neoantigen load did not correlate with ImmScore expression across most cancer types (**Figure 4.4A-B**). To determine if expression of antigen processing and presentation genes was associated with ImmScore, we took an approach similar to the one we undertook

for GlyScore. We extracted all genes within pathways involved in antigen processing and presentation of endogenous peptide antigens on class I MHC and plotted their cross-correlation across all tumors in the cohort of 30 tumor types (n = 9,715). We found that a cluster of genes directly involved in antigen processing (TAP1, TAP2, TAPBP, PSMB8, PSMB9, PSMB10) and presentation (HLA-A, HLA-B, HLA-C, B2M) were highly correlated with each other across all tumor samples, so we chose these genes as our Antigen Presentation Capacity signature (APCScore). We chose this cluster of genes because of the well characterized role of these genes in antigen processing and presentation, as well as due to their inclusion in an antigen-presentation previously shown to associate with immune infiltration in renal cell carcinoma (58) (Figure 4.4C).

APCScore expression showed a strong correlation to ImmScore (Pearson coefficient = 0.66), indicating that increased antigen presentation was associated with increased immune infiltration (**Figure 4.5A**). However, among tumors with similar levels of APCScore expression, some tumors showed increased (red) or decreased (blue) immune infiltration, suggesting that other factors besides antigen processing and presentation could be affecting immune infiltration. To determine if glycolysis was associated with higher or lower than expected ImmScore expression, we plotted the same data as in Fig 2A but color-coded to GlyScore expression. We found that tumors that showed an immune-enriched phenotype (red tumors in Figure 4.5A) had lower levels of GlyScore expression, while tumors with an immune-depleted phenotype (blue tumors in Figure 4.5A) showed increased GlyScore expression (Figure 4.5B). We quantified this effect

by measuring GlyScore expression in the 3 immune phenotypes from Figure 4.5A and found that tumors with an immune-enriched phenotype had significantly lower levels of GlyScore expression across all 13 cancer types in our analysis (**Figure 4.6A**). We further separated patients into 10 categories based on their immune phenotype, from highly immune depleted (“1”) to highly immune enriched (“10”) and plotted the expression of GlyScore across all categories. We found a step-wise reduction in GlyScore expression as tumors become increasingly immune enriched (Figure 4.6B). Further, we visualized this effect in individual cancer types and found that increased GlyScore expression was associated with lower than expected immune infiltration across all 13 cancer types tested, except hepatocellular and rectal carcinomas (LIHC and READ; Figure 4.5D and Figure 4.6C).

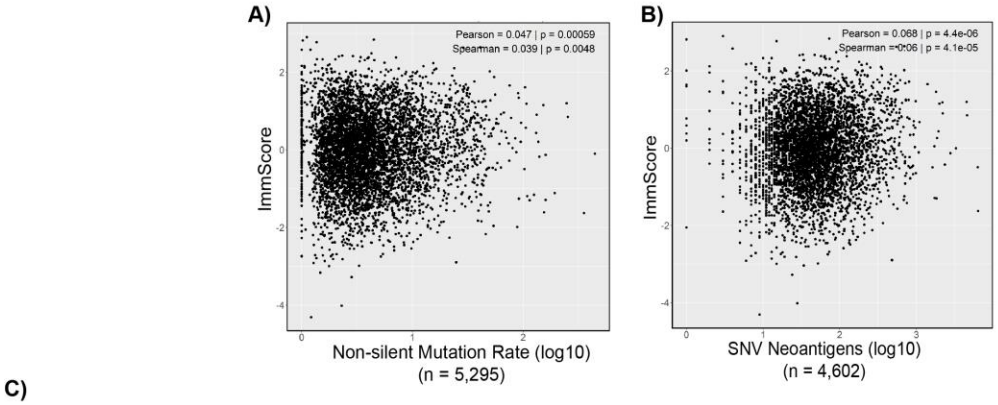
A)
Pearson = 0.047 | p = 0.00059
Spearman = 0.039 | p = 0.0048
ImmScore
Non-silent Mutation Rate (log10)
(n = 5,295)
B)
Pearson = 0.068 | p = 4.4e-06
Spearman =0.06 | p = 4.1e-05
ImmScore
SNV Neoantigens (log10)
(n = 4,602)

C)

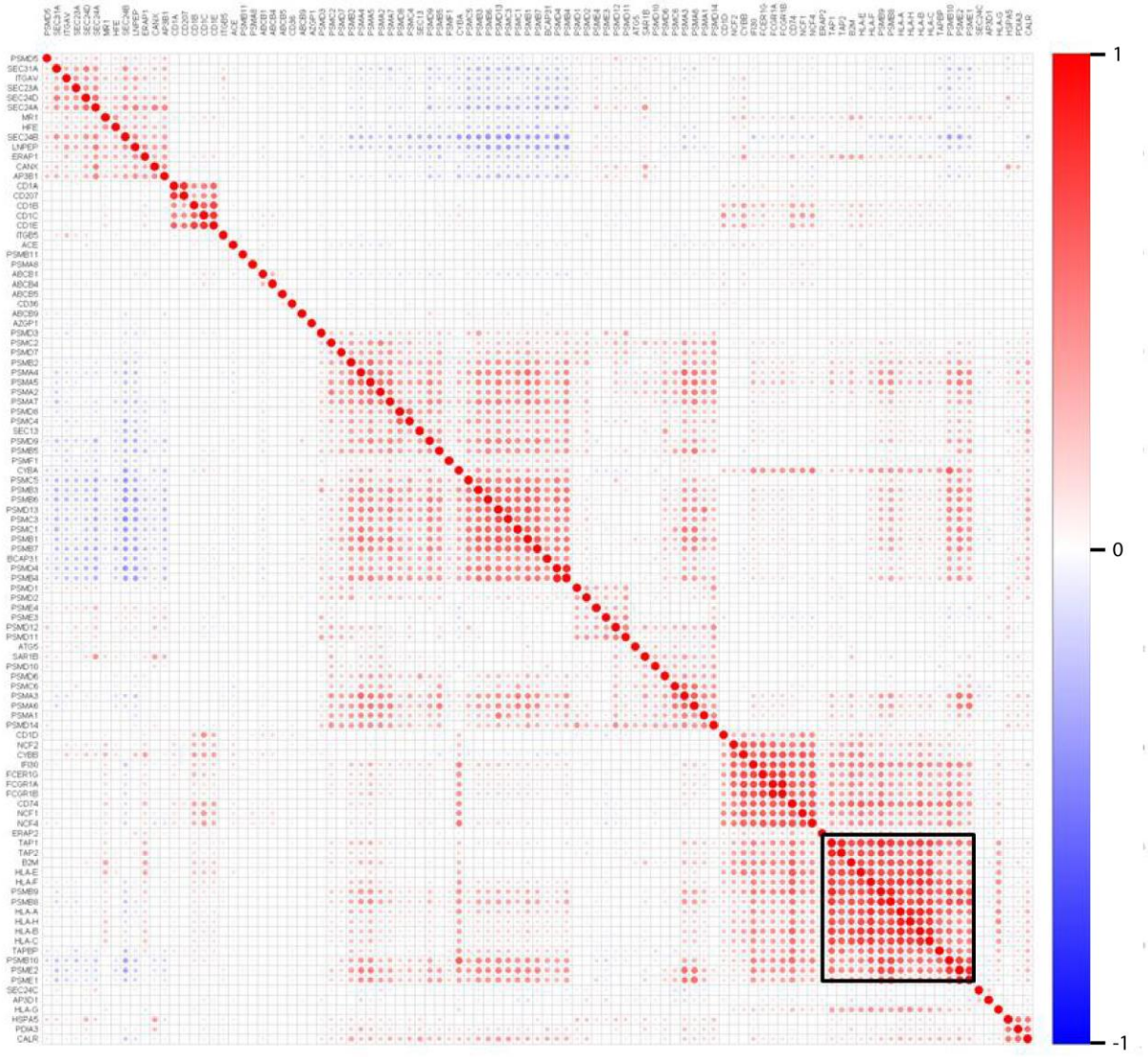
1
0
-1

Figure 4.4. Mutation rate and Antigen Presentation Capacity. A) ImmScore expression plotted against the log10 of Nonsilent Mutations. **B)** ImmScore expression plotted against the log10 of Single Nucleotide Variant (SNV)-derived neoantigens. **C)** Cross correlation plot (Pearson) from all 9,715 tumors in our dataset, with all genes from pathways relating to antigen presentation (see Methods). The black box shows high levels of cross-correlation between classical genes involved in antigen processing and presentation.

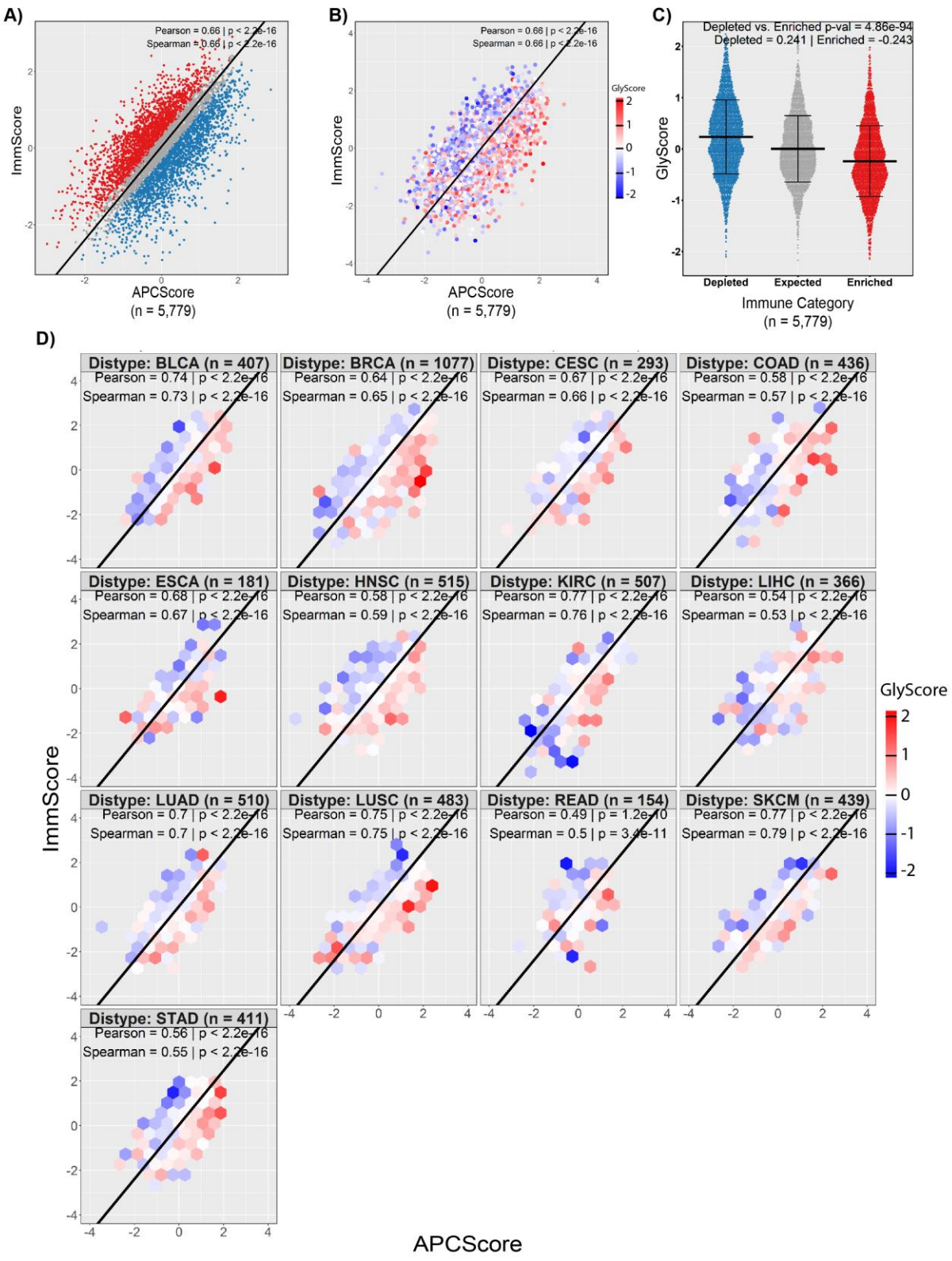
A)
Pearson = 0.66 | p < 2.2e-16
Spearman = 0.66 | p < 2.2e-16
ImmScore
APCScore
(n = 5,779)
B)
Pearson = 0.66 | p < 2.2e-16
Spearman = 0.66 | p < 2.2e-16
ImmScore
APCScore
(n = 5,779)
GlyScore
C)
Depleted vs. Enriched p-val = 4.86e-94
Depleted = 0.241 | Enriched = -0.243
GlyScore
Depleted
Expected
Enriched
Immune Category
(n = 5,779)
D)
Distype: BLCA (n = 407)
Pearson = 0.74 | p < 2.2e-16
Spearman = 0.73 | p < 2.2e-16
Distype: BRCA (n = 1077)
Pearson = 0.64 | p < 2.2e-16
Spearman = 0.65 | p < 2.2e-16
Distype: CESC (n = 293)
Pearson = 0.67 | p < 2.2e-16
Spearman = 0.66 | p < 2.2e-16
Distype: COAD (n = 436)
Pearson = 0.58 | p < 2.2e-16
Spearman = 0.57 | p < 2.2e-16
Distype: ESCA (n = 181)
Pearson = 0.68 | p < 2.2e-16
Spearman = 0.67 | p < 2.2e-16
Distype: HNSC (n = 515)
Pearson = 0.58 | p < 2.2e-16
Spearman = 0.59 | p < 2.2e-16
Distype: KIRC (n = 507)
Pearson = 0.77 | p < 2.2e-16
Spearman = 0.76 | p < 2.2e-16
Distype: LIHC (n = 366)
Pearson = 0.54 | p < 2.2e-16
Spearman = 0.53 | p < 2.2e-16
Distype: LUAD (n = 510)
Pearson = 0.7 | p < 2.2e-16
Spearman = 0.7 | p < 2.2e-16
Distype: LUSC (n = 483)
Pearson = 0.75 | p < 2.2e-16
Spearman = 0.75 | p < 2.2e-16
Distype: READ (n = 154)
Pearson = 0.49 | p = 1.2e-10
Spearman = 0.5 | p = 3.4e-11
Distype: SKCM (n = 439)
Pearson = 0.77 | p < 2.2e-16
Spearman = 0.79 | p < 2.2e-16
Distype: STAD (n = 411)
Pearson = 0.56 | p < 2.2e-16
Spearman = 0.55 | p < 2.2e-16
ImmScore
APCScore
GlyScore

Figure 4.5 Effect of GlyScore on observed vs. predicted ImmScore. A) Immune infiltration (ImmScore) was plotted against antigen presentation capacity (APCScore) for each tumor. The graph is colored by immune phenotype (*red*: enriched; *gray*: expected; *blue*: depleted). **B)** The same data is plotted as in A, but color-coded by expression of GlyScore. **C)** Expression of GlyScore in the three categories described in A. **D)** The data from B was separated into individual cancer types and plotted. In each graph, the hexagon colors represent the mean expression of GlyScore of tumors within each individual hexagon.

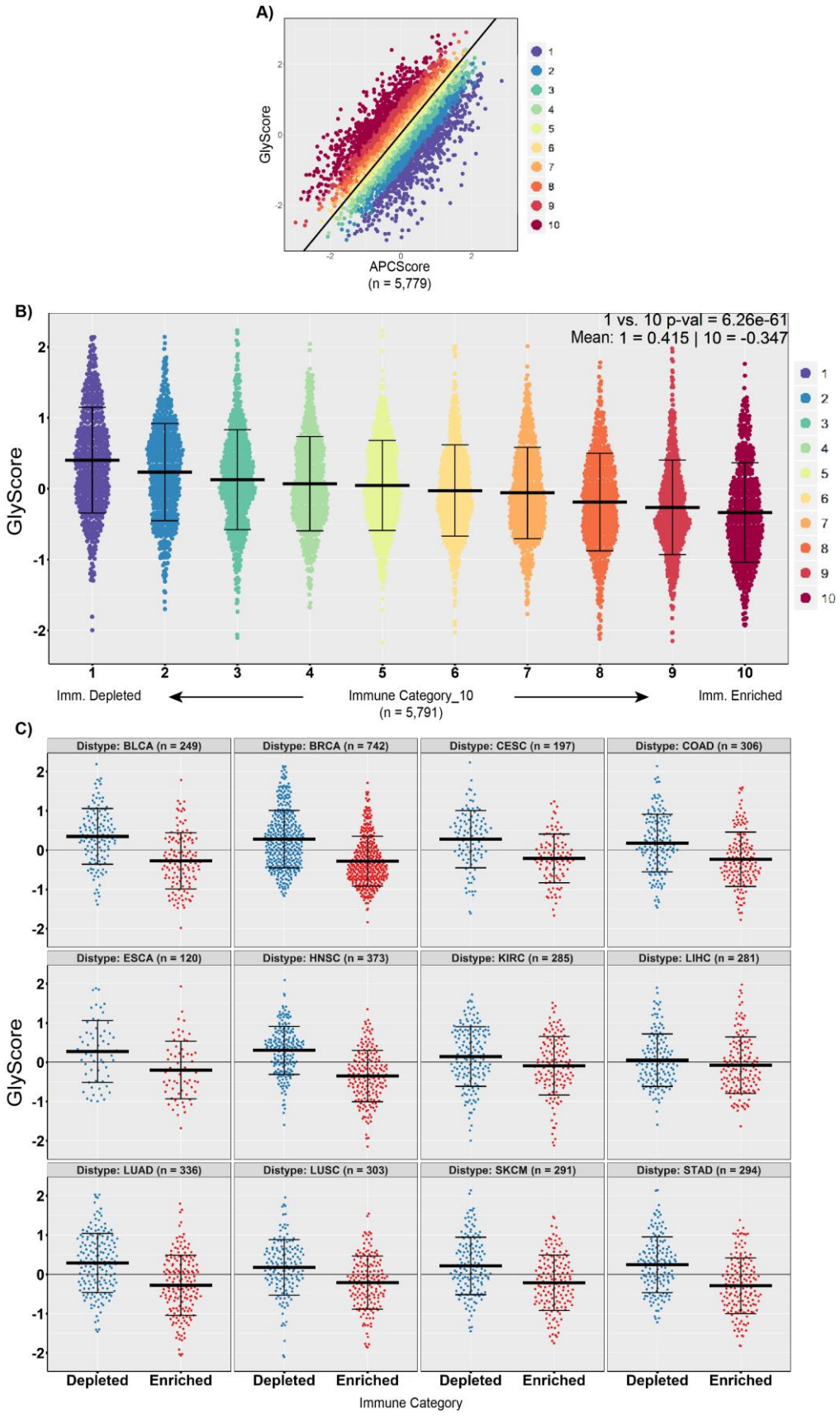
A)
GlyScore
APCScore
(n = 5,779)
1
2
3
4
5
6
7
8
9
10
B)
1 vs. 10 p-val = 6.26e-61
Mean: 1 = 0.415 | 10 = -0.347
GlyScore
Imm. Depleted
Immune Category_10
(n = 5,791)
Imm. Enriched
C)
Distype: BLCA (n = 249)
Distype: BRCA (n = 742)
Distype: CESC (n = 197)
Distype: COAD (n = 306)
Distype: ESCA (n = 120)
Distype: HNSC (n = 373)
Distype: KIRC (n = 285)
Distype: LIHC (n = 281)
Distype: LUAD (n = 336)
Distype: LUSC (n = 303)
Distype: SKCM (n = 291)
Distype: STAD (n = 294)
GlyScore
Depleted
Enriched
Immune Category

Figure 4.6 GlyScore and ImmScore relationship. A) ImmScore plotted against the APCScore for each tumor as in Fig 4.5A, but tumors were divided into 10 immune-related phenotypes, ranging from highly depleted (“1”; purple) to highly immune enriched (“10”; deep red). **B)** Expression of GlyScore in each of the 10 immune-related categories described in C. **C)** Expression of GlyScore in the immune Depleted and Enriched tumors (from Figure 4.5A) for each of the cancer types analyzed (except Rectal Adenocarcinoma, READ).

4.2.6 Unbiased approach reveals glycolysis/gluconeogenesis as the top pathways associated with immune depletion

We took advantage of the immune phenotype we described above to understand how glycolysis ranks among other pathways that may contribute to immune exclusion from solid tumors. We performed traditional differential gene expression analysis followed by Gene Set Enrichment Analysis (GSEA) between immune 'Depleted' vs. 'Enriched' tumors within individual cancer types ('blue' vs. 'red' tumors in Figure 4.3A). This resulted in 13 tables of biological pathways enriched in immune depleted tumors, one for each of the tumor types with FDA-approved immunotherapies described above. We combined all 13 GSEA tables into a single table that combined all the enriched pathways using Fisher's method (to combine multiple p-values into a single 'meta p-value' for each pathway) and obtained a list of pathways enriched in immune depleted tumors across all cancer types. We found that the gluconeogenesis and glycolysis pathways were ranked #11 and #12 from a list of more than 5,000 pathways. We also found that many pathways in this list were highly redundant, with many of the same genes being part of the 'leading edge' of the pathways. Given the large number of pathways enriched in these tumors below an FDR of 0.05 (n = 293) and their redundancy, we performed network analysis to reduce the dimensionality of this data. We found that among the 23 networks of biological pathways enriched in immune depleted tumors, the top differentially enriched network was defined by glucose catabolism. Pathways involved in glycolysis, protein glycosylation and the TCA cycle were all found within this top network **Figure 4.7**). To determine

which genes were most responsible for these observations, we tabulated all the genes that were found in

Biological networks enriched in the 'Immune Depleted' phenotype

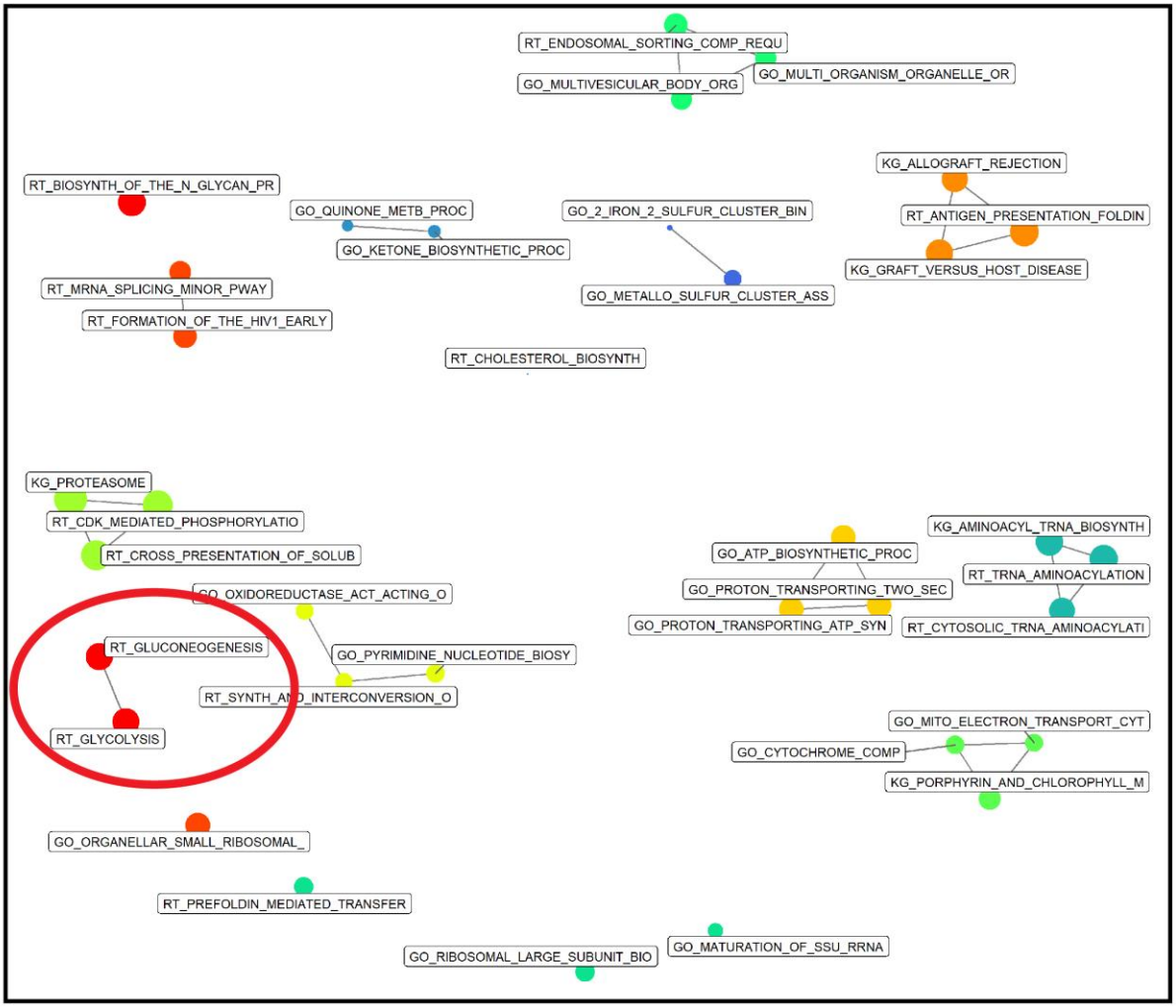

Network terms

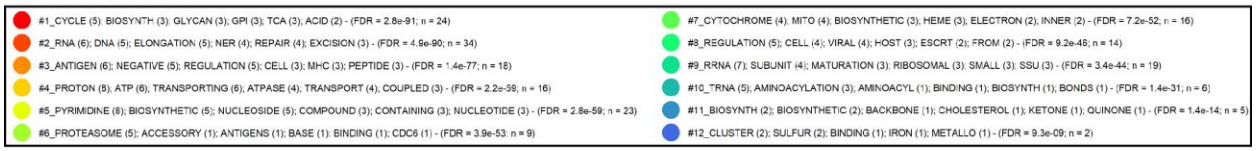

Network genes

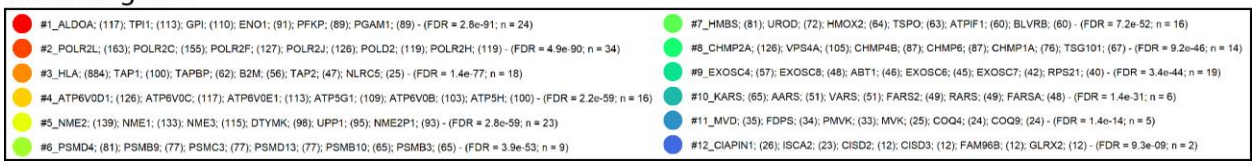

Figure 4.7 Unbiased gene expression analysis reveals glycolysis/gluconeogenesis is enriched in immune-depleted samples. A) Following traditional differential gene expression and gene set enrichment analysis comparing ‘Depleted’ vs. ‘Enriched’ tumors, network analysis was performed to show biological networks enriched specifically in immune-depleted tumors. Shown are the top 3 pathways within each color-coded network (*top*), as well as the biological terms and genes most associated with each network (*bottom*).

the ‘leading edge’ of the pathways across all 13 cancer types, and we found that the enrichment of this sugar metabolism network with immune depletion was mostly driven by the glycolysis genes found in our GlyScore signature.

A potential caveat to our approach is that GlyScore expression may be simply correlated with tumor purity. It is possible that immune-depleted tumors show increased expression of glycolysis genes simply due to the increased purity of these tumor samples. Given the importance of glycolysis for tumor proliferation, it is possible that a simple increase in tumor purity may lead to increased abundance of glycolytic mRNAs in the immune-depleted tumors. To address this concern, we analyzed the association between GlyScore and tumor purity. Sample purity estimates have been published for a large portion of TCGA samples, based on a consensus between 4 different measures of purity: DNA methylation analysis, somatic copy-number variations, stromal- and immune-gene expression, and H&E staining and quantification of tumor slides (59). Based on these measures, the authors developed a Consensus Purity Estimate (CPE). We plotted the CPE and GlyScore expression for each tumor, and found no correlation at all between these two parameters when analyzing the entire dataset (**Figure 4.8A**). When we separated the data into individual cancer types, we found weak correlations between GlyScore and CPE in a small subset of cancer types (Figure 4.8B), but these were not sufficient to account for our observations. We also tested the correlation between expression of a proliferation signature and GlyScore. We found a statistically significant and modest positive correlation between these variables, both in the entire dataset

and when subdivided into individual cancer types (**Figure 4.9A-B**). These results indicate that expression of our glycolysis signature is associated with

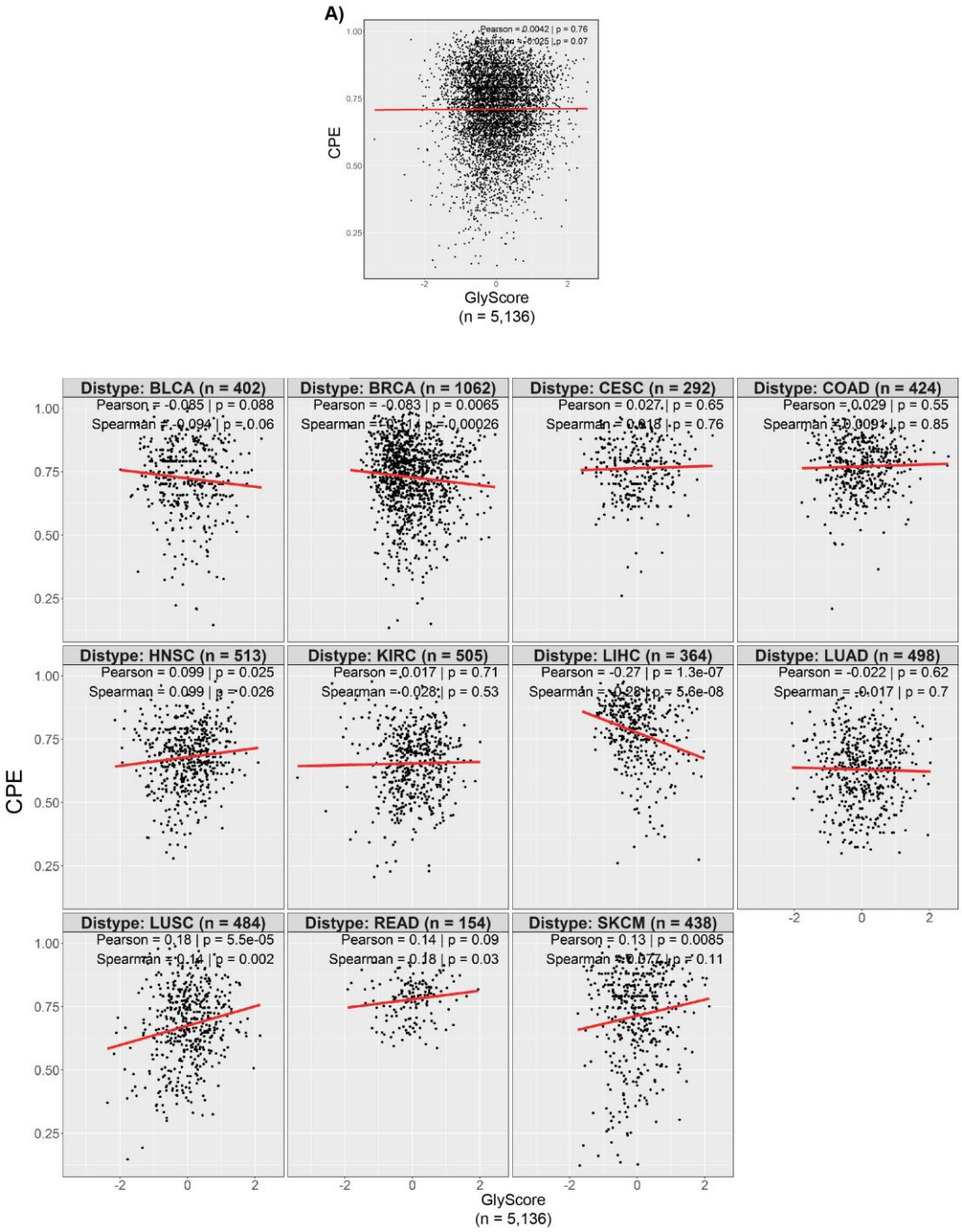

Figure 4.8 Addressing the potential association of tumor purity to GlyScore. A,B) Correlation between GlyScore expression and tumor purity for the entire cohort (A) and each individual cancer type (B).

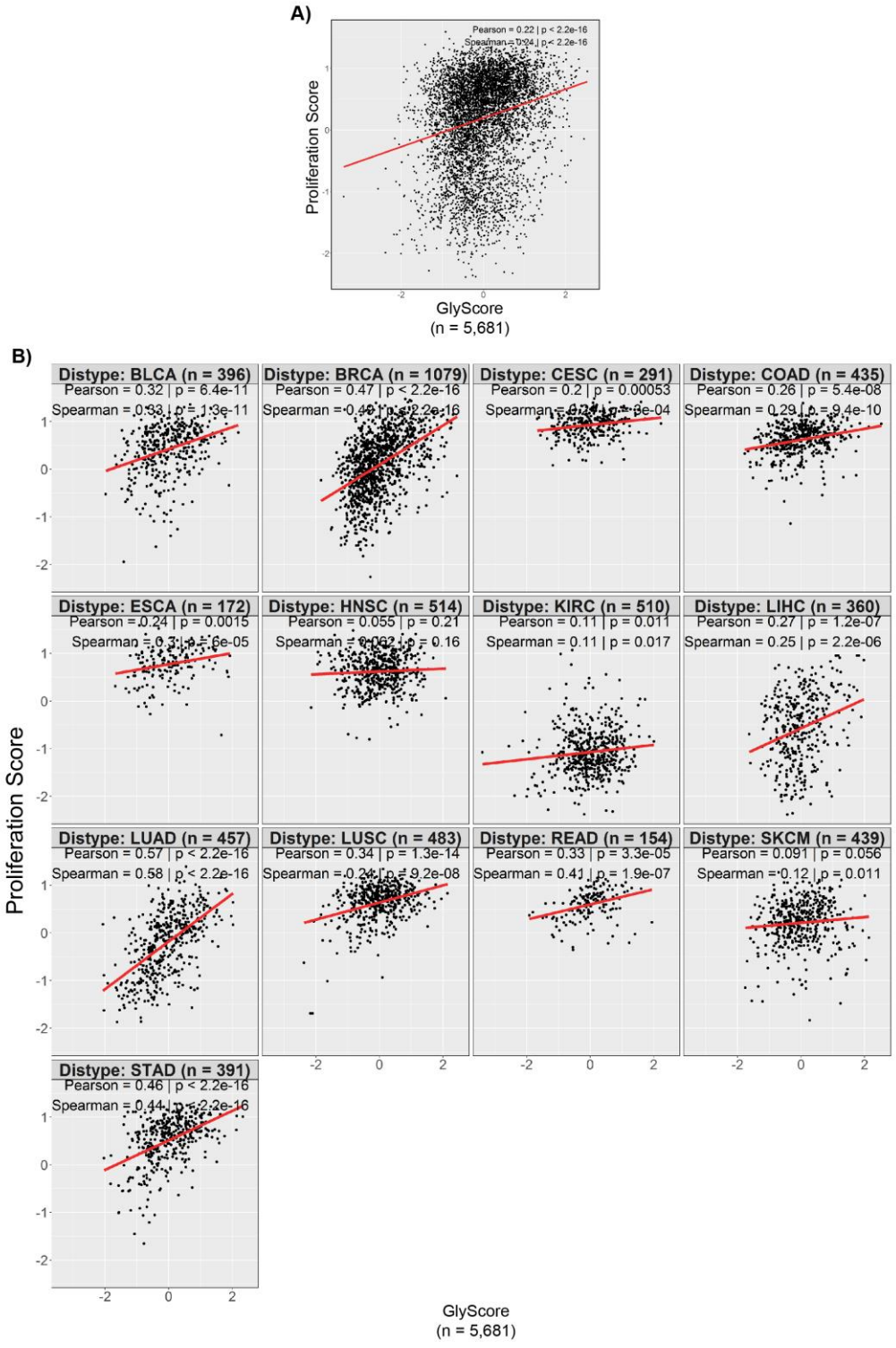
A)
Pearson = 0.22 | p < 2.2e-16
Spearman = 0.24 | p < 2.2e-16
Proliferation Score
GlyScore
(n = 5,681)
B)
Distype: BLCA (n = 396)
Pearson = 0.32 | p = 6.4e-11
Spearman = 0.33 | p = 1.3e-11
Distype: BRCA (n = 1079)
Pearson = 0.47 | p < 2.2e-16
Spearman = 0.49 | p < 2.2e-16
Distype: CESC (n = 291)
Pearson = 0.2 | p = 0.00053
Spearman = 0.24 | p = 9e-04
Distype: COAD (n = 435)
Pearson = 0.26 | p = 5.4e-08
Spearman = 0.29 | p = 9.4e-10
Distype: ESCA (n = 172)
Pearson = 0.24 | p = 0.0015
Spearman = 0.3 | p = 1.6e-05
Distype: HNSC (n = 514)
Pearson = 0.055 | p = 0.21
Spearman = 0.062 | p = 0.16
Distype: KIRC (n = 510)
Pearson = 0.11 | p = 0.011
Spearman = 0.11 | p = 0.017
Distype: LIHC (n = 360)
Pearson = 0.27 | p = 1.2e-07
Spearman = 0.25 | p = 2.2e-06
Distype: LUAD (n = 457)
Pearson = 0.57 | p < 2.2e-16
Spearman = 0.58 | p < 2.2e-16
Distype: LUSC (n = 483)
Pearson = 0.34 | p = 1.3e-14
Spearman = 0.34 | p = 9.2e-08
Distype: READ (n = 154)
Pearson = 0.33 | p = 3.3e-05
Spearman = 0.41 | p = 1.9e-07
Distype: SKCM (n = 439)
Pearson = 0.091 | p = 0.056
Spearman = 0.12 | p = 0.011
Distype: STAD (n = 391)
Pearson = 0.46 | p < 2.2e-16
Spearman = 0.44 | p < 2.2e-16
Proliferation Score
GlyScore
(n = 5,681)

Figure 4.9 Addressing the potential association of tumor proliferation to GlyScore. A,B) Correlation between GlyScore expression and tumor proliferation score for the entire cohort (A) and each individual cancer type (B).

decreased immune infiltration of solid tumors, and that this effect is independent of tumor purity, but associated in part with tumor proliferation.

4.2.7 GlyScore, ImmScore, and patient survival

Next, we sought to determine whether GlyScore and ImmScore correlate with patient survival. For this, we combined the GlyScore and ImmScore into a single 'Tumor Microenvironment Score' (TMEScore) signature, that would be reflective of the glycolytic activity and degree of immune infiltration of a given tumor. To do this, we simply substracted GlyScore from ImmScore. Thus, tumors with an increased TMEScore show increased immune infiltration and low glycolytic gene expression, while those with decreased TMEScore show decreased immune infiltration and high GlyScore expression. We plotted Kaplan-Meier survival plots for all patients in our dataset of solid tumors with FDA-approved . We observed that a high GlyScore predicted short survival (Hazard Ratio (HR) = 1.3), whereas a high ImmScore was associated with better outcomes (HR = 0.92; **Figure 4.10**). Interestingly, TMEScore was associated with improved prognosis, as expected, and it also performed better than either GlyScore or ImmScore alone in predicting patient survival (HR = 0.22). This effect might be due to the combined effect of GlyScore (which separates patients better at early time points) and ImmScore (which separates patients better at later time points). We next looked at how these 3 signatures associated with patient survival in individual datasets and found that TMEScore was significantly associated with improved prognosis in all cancer types except KIRC, LUAD and LUSC (Figure 4.10). We confirmed our results by performing uni- and multi-

variate analysis of TMEScore and survival in our dataset. In agreement with our hypothesis, increased TMEScore was associated with improved prognosis, and this was an independent effect as shown by multi-variate analysis in the entire dataset and when divided into individual cancer types (Tables 2 and 3).

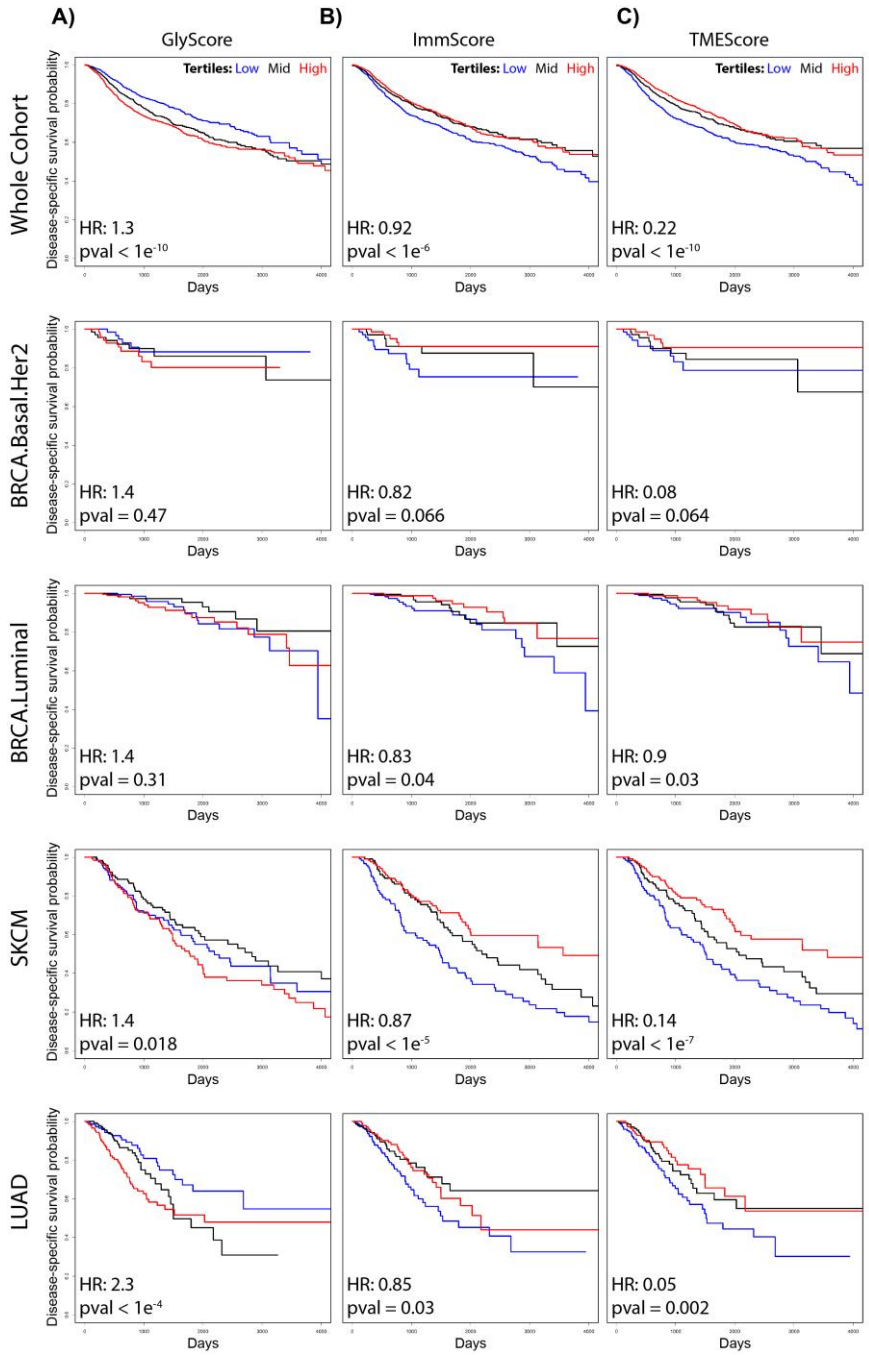

Figure 4.10. Survival by GlyScore, ImmScore and TMEScore in solid tumors. A-C) Kaplan-Meier disease-specific survival analysis was performed for the entire cohort, as well as individually for Basal/HER2 and Luminal breast cancer, skin cutaneous melanoma (SKCM) and lung adenocarcinoma (LUAD). The disease-specific survival probability of patients was measured in the bottom, middle and top tertile of expression of either GlyScore (A), ImmScore (B) and TMEScore (C) for each cancer type, and the Hazard Ratio (HR) was calculated.

TABLE 1	Whole-HR	Whole-sig	BLCA-HR	BLCA-sig	BRCA-HR	BRCA-sig	CESC-HR	CESC-sig	COAD-HR	COAD-sig	ESCA-HR	ESCA-sig	HNSC-HR	HNSC-sig	KIRC-HR	KIRC-sig	LIHC-HR	LIHC-sig	LUAD-HR	LUAD-sig	LUSC-HR	LUSC-sig	READ-HR	READ-sig	SKCM-HR	SKCM-sig	STAD-HR	STAD-sig
Age	1.01	***	1.02	*	1.01	ns	1.01	ns	1.01	ns	1.00	ns	1.01	ns	1.01	ns	1.01	ns	0.98	ns	0.99	ns	1.08	*	1.01	**	1.01	ns
Gender	1.69	***	0.90	ns	1.30	ns	NA	NA	1.13	ns	4.45	*	0.95	ns	1.24	ns	0.82	ns	0.96	ns	1.36	ns	1.93	ns	0.93	ns	1.63	*
Stage	3.08	***	2.44	***	3.92	***	NA	NA	6.22	***	5.74	***	2.15	**	10.21	***	3.56	***	2.46	***	2.72	***	5.16	*	1.29	ns	2.26	***
CPE	1.51	ns	1.10	ns	2.00	ns	15.67	*	0.70	ns	NA	NA	2.29	ns	0.13	**	1.56	ns	3.16	ns	1.88	ns	#####	ns	4.86	***	NA	NA
Proliferation	1.34	***	1.25	ns	1.44	*	0.89	ns	0.52	ns	1.34	ns	1.06	ns	4.57	***	1.93	***	1.91	***	1.04	ns	1.29	ns	1.31	ns	0.76	ns
lGlyScore	1.30	***	1.42	*	1.67	**	2.11	**	1.09	ns	1.15	ns	2.11	***	1.04	ns	1.56	**	2.30	***	1.00	ns	1.74	ns	1.40	*	0.83	ns
lImmScore	0.92	***	0.88	*	0.88	*	0.72	***	1.07	ns	1.09	ns	0.83	**	1.16	*	0.85	*	0.85	*	0.97	ns	0.72	ns	0.87	***	1.03	ns
TMEScore	0.22	***	0.15	**	0.15	*	0.01	***	2.62	ns	2.44	ns	0.06	***	8.74	*	0.08	**	0.05	**	0.65	ns	0.01	ns	0.14	***	1.78	ns

Table 4.1

TABLE 2	Whole-HR	Whole-sig	BLCA-HR	BLCA-sig	BRCA-HR	BRCA-sig	CESC-HR	CESC-sig	COAD-HR	COAD-sig	ESCA-HR	ESCA-sig	HNSC-HR	HNSC-sig	KIRC-HR	KIRC-sig	LIHC-HR	LIHC-sig	LUAD-HR	LUAD-sig	LUSC-HR	LUSC-sig	READ-HR	READ-sig	SKCM-HR	SKCM-sig	STAD-HR	STAD-sig
IGlyScore--IGlyScore	1.23	***	1.31	ns	1.71	*	2.20	**	1.22	ns	1.30	ns	2.22	**	0.87	ns	1.12	ns	1.82	*	0.91	ns	1.39	ns	1.26	ns	1.07	ns
IGlyScore--Age	1.01	***	1.02	ns	1.02	*	1.01	ns	1.02	ns	1.01	ns	1.01	ns	1.01	ns	1.01	ns	1.00	ns	0.99	ns	1.11	**	1.01	*	1.02	ns
IGlyScore--Gender	1.29	***	0.91	ns	0.67	ns	NA	NA	1.04	ns	4.51	ns	0.96	ns	1.12	ns	0.94	ns	0.91	ns	1.35	ns	4.04	ns	0.83	ns	1.63	ns
IGlyScore--Stage	2.76	***	2.34	***	4.62	***	NA	NA	6.61	***	5.11	***	2.17	**	7.53	***	2.77	***	1.92	**	2.72	***	9.09	**	1.44	*	2.63	***
IGlyScore--CPE	1.48	ns	1.84	ns	1.43	ns	19.39	*	0.48	ns	NA	NA	0.78	ns	2.25	ns	2.22	ns	4.48	ns	1.88	ns	######	ns	5.03	**	NA	NA
IGlyScore--Proliferation	1.27	***	1.05	ns	1.42	ns	0.56	ns	0.74	ns	1.88	ns	1.15	ns	3.19	***	1.91	***	1.63	*	0.82	ns	2.76	ns	1.31	ns	0.69	ns
IImmScore--IImmScore	0.86	***	0.82	**	0.74	**	0.71	**	1.02	ns	1.12	ns	0.77	**	0.92	ns	0.77	**	0.90	ns	1.04	ns	1.08	ns	0.82	***	1.01	ns
IImmScore--Age	1.01	***	1.01	ns	1.02	*	1.01	ns	1.02	ns	1.01	ns	1.01	ns	1.01	ns	1.01	ns	1.00	ns	0.99	ns	1.11	**	1.01	*	1.02	ns
IImmScore--Gender	1.38	***	0.82	ns	0.74	ns	NA	NA	1.03	ns	4.66	ns	0.93	ns	1.11	ns	0.93	ns	0.91	ns	1.35	ns	3.85	ns	0.80	ns	1.63	ns
IImmScore--Stage	2.81	***	2.32	***	4.73	***	NA	NA	6.63	***	4.83	***	2.09	*	7.66	***	2.68	***	2.06	**	2.70	***	9.07	**	1.40	*	2.61	***
IImmScore--CPE	0.35	**	0.36	ns	0.07	*	0.86	ns	0.53	ns	NA	NA	0.17	ns	1.16	ns	0.26	ns	1.71	ns	2.37	ns	######	ns	0.58	ns	NA	NA
IImmScore--Proliferation	1.26	***	1.24	ns	1.89	**	0.74	ns	0.79	ns	2.14	ns	1.37	ns	3.08	***	2.27	***	2.08	***	0.77	ns	3.31	ns	1.33	ns	0.72	ns
TMEScore--TMEScore	0.09	***	0.06	**	0.02	***	0.01	**	1.10	ns	3.01	ns	0.02	***	0.39	ns	0.03	**	0.13	ns	1.77	ns	2.20	ns	0.07	***	1.14	ns
TMEScore--Age	1.01	***	1.01	ns	1.02	*	1.01	ns	1.02	ns	1.01	ns	1.01	ns	1.01	ns	1.01	ns	1.00	ns	0.99	ns	1.11	**	1.01	*	1.02	ns
TMEScore--Gender	1.33	***	0.83	ns	0.74	ns	NA	NA	1.03	ns	4.63	ns	0.95	ns	1.11	ns	0.93	ns	0.91	ns	1.35	ns	3.86	ns	0.81	ns	1.63	ns
TMEScore--Stage	2.77	***	2.32	***	4.77	***	NA	NA	6.63	***	4.89	***	2.09	*	7.65	***	2.56	***	2.02	**	2.71	***	8.96	**	1.39	*	2.61	***
TMEScore--CPE	0.31	***	0.36	ns	0.07	*	0.70	ns	0.48	ns	NA	NA	0.12	ns	1.29	ns	0.26	ns	1.25	ns	2.40	ns	######	ns	0.56	ns	NA	NA
TMEScore--Proliferation	1.26	***	1.19	ns	1.79	**	0.69	ns	0.79	ns	2.14	ns	1.36	ns	3.10	***	2.21	***	2.02	***	0.78	ns	3.35	ns	1.31	ns	0.72	ns

Table 4.2

4.2.8 Glycolysis and immune infiltration in ER-negative breast cancer

ER-negative breast cancer showed statistically significant negative correlations with immune infiltration in all types of analysis we performed. Indeed, we observed a negative correlation between the GlyScore and ImmScore (Figure 4.2E-F). A high GlyScore and 'robust' immune infiltration were mutually exclusive (Figure 4.1G-H), and GlyScore was significantly associated with lower-than-expected observed ImmScore (Figure 4.5A).

We sought to determine immunohistochemical surrogates for increased metabolic activity in breast cancer. Our series included 49 treatment naïve primary breast tumors - including 39 TNBCs and 10 ER-negative/HER2-positive breast cancers. The median age of the patients was 47 years old (range, 25-71) and the median size of the tumors was 2.4 cm (range, 0.9 – 5 cm). Fifty-one percent (25/49) and 45% (22/49) of tumors were of T1 and T2 stage, respectively, whilst one tumor was of T3 and another one T4 (1/49; 2% each). Fifty-six percent (27/48) of patients had nodal positivity, whilst 44% (21/48) were node-negative (one patient was missing nodal positivity records) (Table 4). We conducted the immunohistochemical analysis of the glycolytic enzymes GLUT1 and LDHA using the H-score, which is a semiquantitative method that takes into account the percentage of tumor cells that are positive and the intensity of immunoreactivity (**Figure 4.11A**). We also computed a composite score of both markers (Mean Glycolysis H-score) by simply averaging the H-score for both GLUT1 and LDHA. We quantified the correlation between each individual glycolytic marker (and the composite H-Score) and the degree of FDG uptake as

measured by SUV Peak calculations from FDG-PET scans (Figure 4.11B). The SUV_Peak of a lesion is defined as the average SUV in a 1ml sphere, which is positioned such that the average is maximal within a given lesion. Our analysis revealed a strong positive correlation between FDG uptake and GLUT1 expression (Pearson r = 0.67; p = 0.002) that was further enhanced in the Mean Glycolysis H-Score (Pearson r = 0.70; p = 0.001). These results suggest that the expression of glycolytic markers can be used as a marker of glycolytic activity in breast tumors. We also studied how expression of glycolytic enzymes and immune infiltration affects patient recurrence-free survival (RFS), and found that increased expression of glycolytic markers was associated with poor prognosis (HR 3.3, p = 0.06), while increased stromal immune infiltration was associated with better prognosis (HR = 1.2e-8, p = 0.99), although this analysis did not reach statistical significance, possibly due to low patient numbers (Figure 4.11C, D).

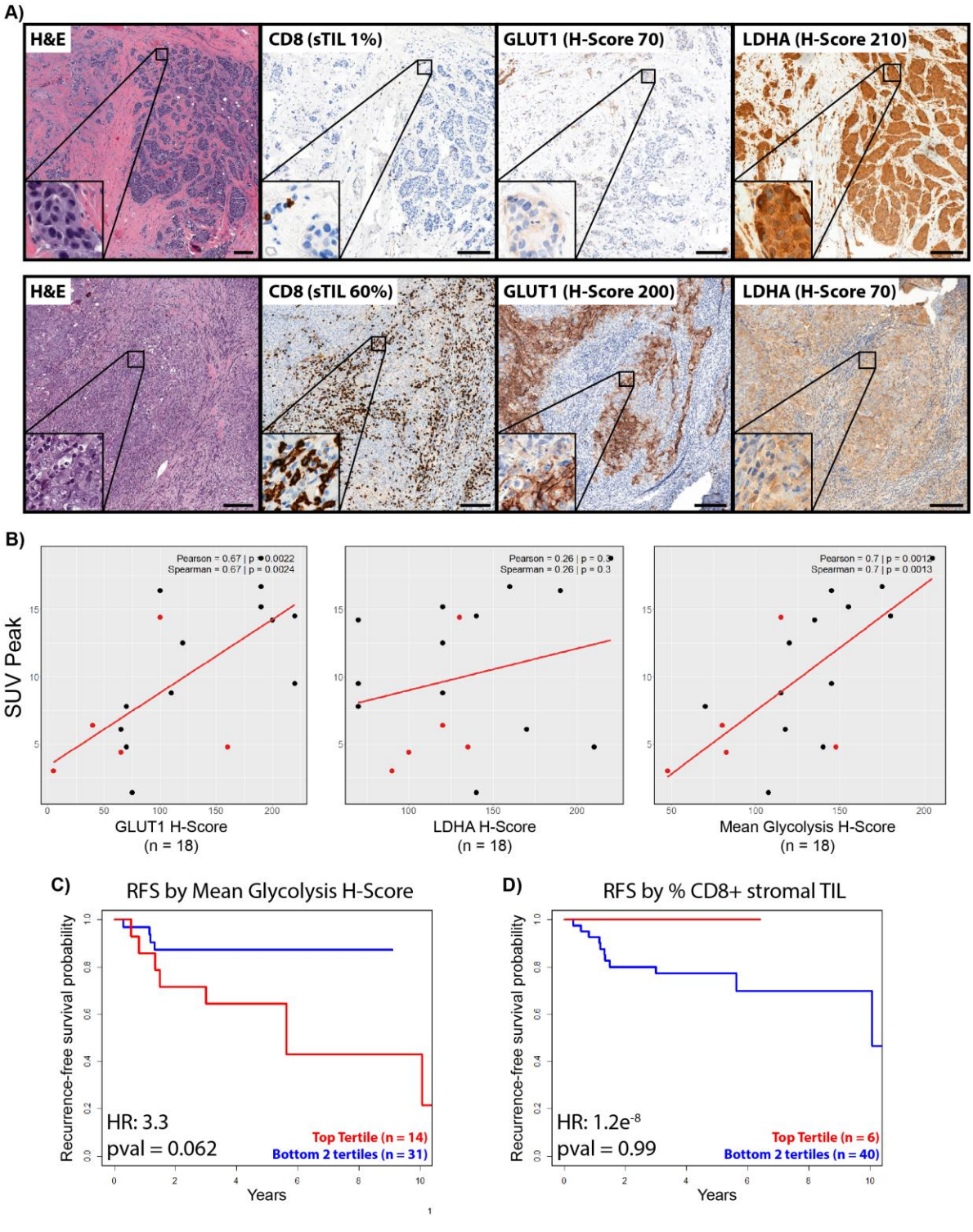
A)
H&E
CD8 (sTIL 1%)
GLUT1 (H-Score 70)
LDHA (H-Score 210)
H&E
CD8 (sTIL 60%)
GLUT1 (H-Score 200)
LDHA (H-Score 70)
B)
SUV Peak
Pearson = 0.67 | p = 0.0022
Spearman = 0.67 | p = 0.0024
GLUT1 H-Score
(n = 18)
Pearson = 0.26 | p = 0.3
Spearman = 0.26 | p = 0.3
LDHA H-Score
(n = 18)
Pearson = 0.7 | p = 0.0012
Spearman = 0.7 | p = 0.0013
Mean Glycolysis H-Score
(n = 18)
C)
RFS by Mean Glycolysis H-Score
Recurrence-free survival probability
HR: 3.3
pval = 0.062
Top Tertile (n = 14)
Bottom 2 tertiles (n = 31)
Years
D)
RFS by % CD8+ stromal TIL
Recurrence-free survival probability
HR: 1.2e-8
pval = 0.99
Top Tertile (n = 6)
Bottom 2 tertiles (n = 40)
Years

Figure 4.11. Expression of glycolytic and immune markers in primary breast tumors. A) Representative images of immunohistochemical staining for CD8, GLUT1 and LDHA. Shown are selected sections of tumors with high LDHA expression and low stromal CD8+ T-cell infiltrate (top), and with low LDHA expression and high stromal CD8+ T-cell infiltration (bottom). **B)** Volumetric Regions of Interest (ROIs) were drawn on FDG-PET scans for 18 pts with available scans, and the SUV Peak was calculated and plotted against expression of the glycolytic markers. Mean Glycolysis H-Score is the geometric mean of the GLUT1 and LDHA H-Scores. **C)** Recurrence-free survival was calculated and Kaplan-Meyer plots were plotted for the 'top' vs. 'bottom' tertiles of Mean Glycolysis H-Score expression (left) and CD8+ stromal infiltration (right).

PT_ID	Age	DxYear	Histologic_Type	Size	Subtype	T	N	M	SUV_Max	SUV_Peak	DxDate	LDHA	GLUT1	TILs	CD3	CD8	RFS_Time	RFS_Event	REC_Site	OS_Time	OS_Event
1	52	2014	IDC NOS	3.8	TNBC	T2	N0	M	NA	NA	5/28/2014	120	120	80	40	30	20	3.7589041	0		3.9945205	0
2	45	2014	IDC NOS	2.2	TNBC	T2	N0	M	21.1	16.4	1/30/2014	190	190	100	10	NA	2	4.2082192	0		4.3178082	0
3	46	2015	IDC NOS	5	TNBC	T2	N1	M	18	15.2	2/11/2015	120	120	190	5	2	1	3.1561644	0		3.2849315	0
4	59	2015	IDC NOS	1.6	TNBC	T1	N0	M	7.6	6.1	5/16/2015	170	170	65	10	10	5	2.8	0		3.0273973	0
5	71	2014	IDC NOS	3.4	TNBC	T2	N1	M	9.2	7.8	1/10/2014	70	70	70	10	10	5	0.3013699	1	Ipsilateral b	4.3726027	0
6	70	2015	IDC NOS	0.9	TNBC	T1	N0	M	1.5	1.4	##########	140	140	75	10	10	5	2.3780822	0		0.5808219	1
7	35	2014	IDC NOS	2.5	TNBC	T2	N1	M	6	4.8	##########	210	210	70	1	1	1	3.4328767	0		3.5123288	0
8	37	2014	IDC with mic	1.1	HER2	T1	N3	M	2.3	4.4	9/29/2014	100	100	65	80	70	60	3.539726	0		3.6547945	0
9	31	2013	IDC NOS	1.2	TNBC	T1	N0	M	17	14.2	2/7/2013	70	70	200	80	70	60	5.2575342	0		5.2958904	0
10	47	2013	IDC NOS	1.5	TNBC	T1	N0	M	10.4	8.8	7/30/2013	120	120	110	50	40	20	4.7643836	0		4.8219178	0
11	39	2013	IDC NOS	1.5	TNBC	T1	N2	M	14.6	12.5	2/7/2013	120	120	120	20	10	5	5.2219178	0		5.2958904	0
12	37	2013	IDC with foc	2.1	TNBC	T2	N0	M	17.6	NA	1/18/2013	250	170	5	3	2	5	5.2356164	0		5.3506849	0
13	34	2013	IDC NOS	2.7	TNBC	T2	N1	M	NA	NA	2/1/2013	120	170	2	2	1	5	5.2273973	0		5.3123288	0
14	36	2011	IDC NOS	1.7	TNBC	T1	N1	M	10.8	9.5	6/6/2011	70	220	10	10	10	5	6.9123288	0		6.9726027	0
15	37	2013	IDC NOS	3.5	TNBC	T2	N0	M	17.3	14.5	6/11/2013	140	220	70	60	20	4	4.8794521	0		4.9561644	0
16	35	2012	IDC NOS	4.2	TNBC	T2	N3	M	19.5	16.7	8/9/2012	160	190	5	5	2	5	5.6986301	0		5.7945205	0
17	56	2012	IDC NOS	3	TNBC	T2	N1	M	25.7	18.8	9/14/2012	220	190	30	20	5	5	5.6054795	0		5.6958904	0
19	30	2013	IDC NOS	2.6	TNBC	T2	N0	M	3.4	NA	1/25/2013	110	85	70	70	NA		5.2410959	0		5.3315068	0
20	51	2011	IDC NOS	1.8	HER2	T2	N3	M	18	14.4	7/27/2011	130	100	40	30	10	6	6.6164384	0		6.8328767	0
21	36	2011	IDC NOS	0.55	TNBC	T1	N0	M	NA		##########	130	110	50	40	30	6	6.4109589	0		6.5315068	0
22	61	2010	IDC NOS	4.2	HER2	T2	N1	M	3.5	3	9/14/2010	90	5	30	20	10	7	7.5616438	0		7.6986301	0
23	25	2010	Invasive mic	5	HER2	T2	N3	M	6.1	4.8	6/2/2010	135	160	10	5	5	1	1.1890411	1	Skin	7.9835616	0
24	59	2013	IDC NOS	2.5	HER2	T2	N3	M	NA		4/19/2013	110	80	40	30	20	4	4.9068493	0		5.1013699	0
25	36	2013	IDC NOS	4.3	HER2	T2	N2	M	7.8	6.4	9/12/2013	120	40	40	30	20	4	4.6027397	0		4.7013699	0
26	41	2012	IDC NOS	1.6	TNBC	T1	N0	M	NA		1/3/2012	120	260	10	10	5	1	1.4958904	1	Lymph	6.3945205	0
27	49	2010	IDC NOS	0.9	HER2	T2	N0	M	NA		10/5/2010	250	180	5	5	2	1	0.5534247	1	Ipsilateral b	7.6410959	0
28	46	2014	IDC NOS	2.2	TNBC	T2	N0	M	NA		3/25/2014	190	170	40	30	20	1	1.1589041	1	Lymph	4.169863	0
29	29	2015	IDC NOS	2.2	TNBC	T2	N0	M	NA		6/8/2015	130	180	90	90	70	2	2.8575342	0		2.9643836	0
30	43	2012	IDC NOS	2	TNBC	T1	N1	M	NA		##########	190	200	5	5	2	5	5.3506849	0		5.430137	0
31	50	2012	IDC NOS	2	TNBC	T1	N2	M	NA		##########	140	270	10	5	5	1	1.3369863	1	Ipsilateral b	3.7917808	1
32	54	2013	IDC NOS	1.6	TNBC	T1	N1	M	NA		3/8/2013	140	210	10	5	5	1	1.3287671	1	Ipsilateral b	3.4520548	1
33	69	2013	IDC NOS	1.7	TNBC	T1	N0	M	NA		5/7/2013	90	140	50	40	30	4	4.9726027	0		5.0520548	0
34	46	2013	IDC NOS wit	2.5	TNBC	T2	N2	M	NA		5/8/2013	100	190	30	30	10	4	4.8410959	0		5.0493151	0
35	65	2013	IDC NOS	0.5	HER2	T1	N0	M	NA		4/29/2013	100	NA	80	70	60	5	5.0082192	0		5.0739726	0
36	67	2011	IDC NOS	1.3	TNBC	T1	N0	M	NA		3/4/2011	180	290	2	2	1	3	3.0109589	1	Ipsilateral b	5.3561644	1
37	47	2014	IDC NOS	1.6	TNBC	T1	N2	M	NA		##########	150	280	10	5	5	3	3.309589	0		3.4054795	0
38	37	2010	IDC NOS	1.6	TNBC	T1	N0	M	NA		##########	10	200	50	40	20	7	7.5260274	0		7.6164384	0
39	41	2013	IDC NOS	2.1	TNBC	T2	N2	M	NA		1/18/2013	160	200	20	10	10	5	5.2849315	0		5.3506849	0
40	47	2013	IDC NOS	2.7	HER2	T1	N2	M	NA		4/17/2013	130	170	40	30	20	5	5.0054795	0		5.1068493	0
41	47	2013	IDC NOS wit	1	HER2	T1	N1	M	NA		1/16/2013	180	190	40	30	10	5	5.2931507	0		5.3561644	0
42	61	2013	IDC NOS	2.4	TNBC	T2	N1	M	NA		3/27/2013	190	200	30	20	20	5	5.0657534	0		2.8931507	1
43	51	2013	IDC NOS	7.5	TNBC	T3	N3	M	NA		9/12/2013	200	270	10	10	5	5	0.8054795	1	Liver	1.0191781	1
44	62	2001	IDC with foc	1.4	TNBC	T1	N1	M0	NA		3/8/2001	280	10	5	5	5	5	17.032877	0		17.224658	0
46	60	2006	IDC NOS	0.7	TNBC	T1	NA	M	NA		2/28/2006	230	180	5	5	5	0	12.20274	0		12.243836	0
49	52	2007	IDC with ap	4	TNBC	T4	N3	M0	NA		11/7/2007	220	180	10	10	5	5	5.6410959	1	Lymph	7.0246575	1
50	54	2006	IDC NOS	0.6	TNBC	T1	N0	M0	NA		12/4/2006	290	NA	10	5	5	5	11.243836	0		11.479452	0
51	57	2000	IDC NOS	0.25	TNBC	T1	N0	M	NA		5/5/2000	240	260	30	30	20	20	18.049315	0		18.065753	0
52	64	2009	IDC with ap	0.2	TNBC	T1	N0	MX	NA		2/9/2009	250	20	2	2	1	1	9.0958904	0		9.2931507	0
54	60	2006	IDC NOS	1.7	TNBC	T1	N1	0	NA		8/3/2006	280	170	30	30	20	20	10.076712	1	Lymph	11.816438	0

Table 4.3

Next, we assessed the relationship between expression of glycolytic markers and immune infiltration in breast cancer. For this we sought to determine the relationship between the expression of the glycolytic enzyme LDHA and the extent of lymphocytic infiltration. As a preliminary step, we plotted the correlation between glycolytic and immune protein expression from our CPTAC dataset, and found that there was a significant negative correlation between expression of the glycolytic markers LDHA and TPI1, and the immune markers CD8 and CD3 (**Figure 4.12A**). To determine whether increased LDHA expression in our IHC-stained cohort was associated with decreased immune infiltration, we separated our samples into either the top tertile of LDHA expression vs. the bottom 2 tertiles of LDHA expression. We found that tumors with the highest levels of tumor-cell LDHA expression displayed a significantly lower infiltration of TILs (left), and of CD3+ (middle) and CD8+ (right) stromal lymphocytes (Figure 4.12B; p = 0,001, 0.003 and 0.015, respectively). Moreover, the extent of CD8+ sTILs inversely correlated with the LDHA expression, when used as a continuous variable (Figure 4.12C). Based on 12C, three clusters with different magnitudes of CD8-positive sTILs and LDHA expression levels were identified. Lastly, we sought to determine whether patients in these three clusters would have differences in survival. Our analysis revealed that patients of cluster 3, whose tumors displayed high CD8-positive TILs and low LDHA expression level, tended to have a better overall survival (Figure 4.12D). Although statistical significance was not achieved (probably reflecting the low number of patients in the cohort), no patients in cluster 3 had a recurrence event so far. In contrast, patients in

clusters 1 and 2 had high and moderate LDHA levels and low CD8+ TILs, respectively; up to 20-40% of patients in these clusters have experienced tumor recurrence. Taken together, these findings show that increased metabolic tumor activity is associated with immune exclusion and a worse clinical outcome.

4.3 Summary

A limited number of studies have shown the inverse correlations between expression of select glycolytic and immune markers in a limited number of tumor types. In this study, however, we took a more comprehensive approach to develop a glycolysis signature and study its correlations to immune markers across multiple tumor types. We found that increased expression of GlyScore was associated with decreased immune infiltration, and decreased patient survival across multiple solid tumor types. Further, we showed a similar effect in primary breast tumor samples stained for glycolytic and immune markers using IHC.

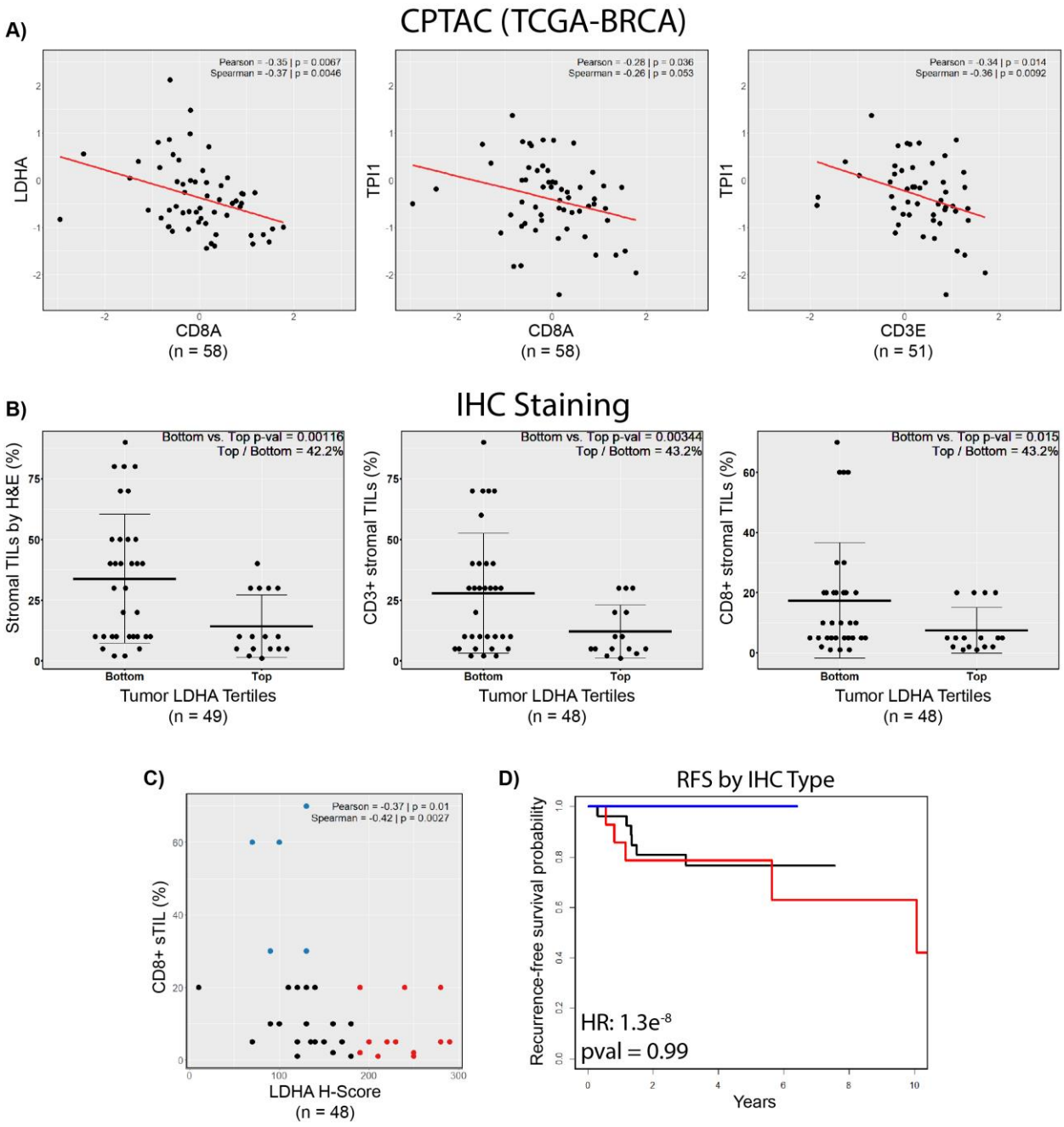

Figure 4.12. Inverse relationship between glycolytic and immune marker protein expression in primary breast tumors. A) Protein expression data were downloaded from the CPTAC and plotted for LDHA, TPI1, CD8A and CD3E (Z-scores). **B)** Stromal lymphocytic infiltration was quantified and plotted in tumors in the top tertile of LDHA expression vs. tumors in the bottom 2 tertiles of LDHA expression, as measured by the H-Score. **C)** The percentage of stromal CD8+ TILs was plotted against the LDHA H-Score, and data was color according to whether the sample was in the top tertile for either CD8+ sTIL (blue), LDHA H-Score (red) or neither (black). **D)** Recurrence-free survival was calculated and Kaplan-Meyer plots were plotted for all tumors according to their phenotype as described in C.

CHAPTER 5

SUMMARY

5.1 Conclusions

The overarching goal of my thesis was to demonstrate the immune suppressive role of lactic acid, which can preclude the host from mounting a successful anti-tumor immune response. This effort began with *in-vitro* studies showing how increasing concentrations of lactic acid can strongly inhibit the T-cell phenotype, and was followed by *in-vivo* studies demonstrating how inhibition of lactate synthesis and transport can lead to the development of a stronger anti-tumor immune response. Finally, to determine whether our findings in the lab using mouse models of cancer were also relevant in human solid tumors, we performed a large-scale study of the relationships between markers of tumor glycolysis and of immune infiltration. In short, this thesis provides evidence that the Warburg effect (increased tumor glycolysis) is a mechanism used by multiple solid tumors to escape immune attack.

The role of metabolites in regulating cellular function and signaling (in both normal or cancer cells, or within an immune context) is becoming increasingly clear. Specific metabolites have been implicated in directly regulating cell survival and function. Specifically, multiple metabolites in different glycolytic steps have been shown to directly regulate specific signaling pathways. For example, fructose-1-6-bisphophate (FBP) was shown to directly bind and activate EGFR in cancer cells (105), as well as to regulate AMPK activity through Aldolase (106);

glyceraldehyde-3-phosphate is known to bind its glycolytic enzyme GAPDH and release RheB to allow mTORC1 activation (107), and GAPDH was also shown to directly regulate IFN-g production by T-cells in response to changing glycolytic flux (108). Further, phosphoenol-pyruvate (PEP) was shown to directly regulate Ca^{2+} release from the endoplasmic reticulum in T-cells and thus regulate their activation under different metabolic conditions (109), and lactate was shown to stabilize HIF1-a in macrophages and fuel oxidative phosphorylation in regulatory T-cells (104, 110). In addition, multiple glycolytic enzymes have been long known to have other non-metabolic functions in cells (111, 112). Furthermore, recent studies show that glycolytic enzymes are rapidly turning over during periods of increased glycolysis, and are stabilized during periods of low glycolysis (113). This suggests that cellular metabolic rates can strongly affect not just energy and nutrient availability, but also multiple cellular processes.

Thus, the notion that glycolytic enzymes and metabolites serve simply to provide nutrients to cells and tumors vastly underestimates their function. In this study, we hypothesized that in addition to allowing high rates of glycolysis within tumor cells, upregulation of LDHA in tumor cells may also serve to promote immune escape.

Herein, we provide multiple lines of evidence supporting this main hypothesis. We clearly show that addition of lactic acid to cultures of T-cells *in-vitro* strongly inhibits their proliferation, activation, and cytokine secretion (Figures 3.1, 3.2, 3.7). We also show, using an anti-PSMA CAR T-cell model developed by the Ponomarev lab, that CAR T-cells kill PSMA-expressing tumor

cells more efficiently when either LDHA or lactate transport is inhibited (Figure 3.8). Using *in-vivo* mouse models of breast and prostate cancers, we further show that depletion of LDHA from tumor cells leads to a dramatically altered TME. LDHA-depleted tumors show a “normalization” of the tumor vasculature and with increased infiltration by CD4 and CD8 T-cells (Figures 3.9, 3.10).

Given these *in-vivo* and *in-vitro* findings, we next focused our attention on immunotherapy. Multiple types of immunotherapy are revolutionizing cancer care today, including immune checkpoint blockade and CAR T-cell therapy. While an unprecedented number of patients are obtaining clinical benefits from these therapies, a large percentage receive little or no benefit, particularly patients with solid tumors. Immune checkpoint blockade shows very high response rates in melanoma and lung cancer, especially in combination with checkpoint inhibitors. Nevertheless, the average response rate to immunotherapy across multiple cancer types is roughly 20-25%. CAR T-cell therapy has shown very good results in several hematological cancers (~80 % respond), but the response rate in solid tumors is much less and there is no currently FDA-approved CAR T-cell therapy for solid tumors.

Given our *in-vitro* findings and the robust increase in immune infiltration observed in our LDHA-depleted tumors, we hypothesized that combining immunotherapy with tumor-cell LDHA depletion may serve to improve responses to immunotherapy. We observed that combination of LDHA depletion and anti-CTLA4 treatment led to a dramatic improvement in the proportion of mice showing long-term survival in a very aggressive mouse model of TNBC (4T1;

Figure 3.11). In addition, we also found that anti-PSMA CAR T-cells showed increased trafficking to and localization within LDHA-depleted prostate tumors, although the therapeutic efficacy was modest (Figure 3.12). Finally, to determine whether inhibiting lactate accumulation in a more clinically relevant setting was feasible, we tested two inhibitors of lactate transport, NGY-008 and NGY-066. We found that NGY-066 reliably and strongly inhibited glycolytic rates in tumor cells while being tolerated by T-cells (Figure 3.6, 7). After finding that this compound effectively rescued the immune-suppressive effects of lactic acid (likely by inhibiting lactate import into T-cells), we found that this compound modestly enhanced the efficacy of CAR T-cell killing (Figure 3.8). As with genetic LDHA depletion, we determined whether combination therapy with MCT1/4 inhibition (NGY-066) improved the efficacy of immune checkpoint blockade in our 4T1 surgical model. We found a modest improvement in the control of metastatic disease and long-term overall survival (Figure 3.11).

Thus, we saw multiple lines of evidence that supported the hypothesis that increased rates of tumor glycolysis and lactate accumulation are in fact highly immune suppressive. This was true in our *in-vitro* and *in-vivo* experiments, and it was observed in multiple models of cancer, including breast and prostate cancer. Thus, while there was an abundance of evidence supporting our hypothesis, based on our studies and other published research (see Introduction, Section 1.2.2), there was only scant evidence showing that this effect was widely observed in human tumors. For instance, Brand, et. al. showed a weak negative correlation between LDHA and the immune-related genes CD25 and Granzyme

K in 470 melanoma samples from the TCGA (85). Cascone, et. al., recently performed a similar analysis of melanoma samples from TCGA and lung cancer samples from the PROSPECT trial. However, this analysis was again limited to only two tumor types, and to a “manual” selection of glycolysis and immune-related genes (114).

In this study, we sought to determine the role of tumor glycolysis in affecting T-cell infiltration of solid tumors across a variety of cancer types. Our hypothesis was that tumor glycolysis and T-cell infiltration would be negatively correlated. To test this hypothesis, we developed an immune signature (ImmScore) as a surrogate, that would specifically reflect T-cell infiltration. By selecting genes for CD3 (E/D), CD8 and LCK, this provided us with a good measure of T-cell infiltration exclusively, compared to other signatures that incorporate activation/exhaustion markers, B-cells or NK cells, such as the TIS, TIL, and a Cytolytic signature, respectively (97, 115, 116). In fact, this simple signature correlated to similar degrees as the other signatures to measures of immune cell infiltration such as leukocyte fraction calculations (measured by analyzing DNA methylation) and quantification of H&E-stained tumor slides (Figures 4.1, 4.2).

In order to study the role of tumor glycolysis in affecting T-cell infiltration of tumors, we also developed a novel glycolytic signature. We chose to develop a new signature because currently existing gene sets, such as those found in Gene Ontology or Reactome pathway databases, are typically very broad and do not necessarily represent core glycolytic genes. In fact, when we plotted the

correlation of all genes involved in glucose catabolism or glycolysis across all 9,715 tumor samples, we found a robust cross correlation between all 10 genes involved in the step-wise breakdown of glucose to lactate. Therefore we chose these 10 genes to represent the glycolysis signature GlyScore. Interestingly, in a cohort of 20 primary breast cancer patients for which we had available microarray expression data and ^{18}F-FDG PET scans, we found a strong positive correlation between the GlyScore and ^{18}F-FDG uptake (Figure 4.1).

Using these 2 signatures, we found that their expression was negatively correlated and mutually exclusive across many (but not all) cancer types. The negative correlation was most notable in basal and HER2-enriched breast cancer subtypes, lung cancer, and melanoma (Figure 4.1, 4.2). Using the full spectrum of the data reported by Thorsson et. al. in their Immune Landscape article (117), we found that the ImmScore was strongly associated with the most immune-reactive clusters. Cluster 2 (IFN-g dominant), Cluster 3 (active inflammation) and Cluster 6 (TGF-beta dominant) had significantly higher ImmScore compared to the other clusters. Interestingly, Cluster 3, characterized by Thorsson et. al. by having the most active inflammatory phenotype, the highest Th17 signaling, and the longest median disease-specific survival across cancer types, showed a significantly lower GlyScore compared to the other clusters (Figure 4.1). Together, these data support the hypothesis that increased expression of glycolytic genes can inhibit the establishment of robust and active T-cell infiltration in solid tumors.

We also wanted to take into account the role of antigen presentation machinery (APM) genes in promoting immune infiltration into solid tumors, since expression of this gene class has been associated with increased T cell infiltration. We found a strong correlation between the expression of APCScore and ImmScore, as expected, but there was a significant portion of tumors that deviated from the expected ImmScore in both directions (positive and negative). Some tumors showed a greater-than-expected ImmScore while others showed lower-than-expected immune infiltration. Interestingly, tumors with an immune-depleted phenotype (i.e., those showing a lower-than-expected ImmScore) had a significantly higher GlyScore when compared with the GlyScore of immune-enriched tumors. This indicated that after taking into account other factors that can affect immune infiltration, such has expression of APM genes, GlyScore was strongly associated with decreased immune infiltration across multiple solid tumor types (Figure 4.5).

Finally, we corroborated our findings in a cohort of 49 patients from our institution by performing IHC staining for glycolytic and immune markers in primary breast tumor tissue. We found that expression of GLUT1 and LDHA correlated strongly with FDG uptake as measured by SUV Peak (Figure 4.11). Further, in agreement with our bioinformatic findings, there was a strong negative correlation and mutual exclusivity between expression of LDHA and all 3 immune variables (CD3, CD8 and total lymphocyte counts by H&E; Figure 4.12).

Based on the clearly established importance of glycolysis in multiple signaling pathways, and on the role of glucose abundance and lactate

accumulation in regulating immune cell function, we hypothesized that increased tumor glycolysis may be a widespread mechanism of immune evasion across multiple solid tumor types. We were able to demonstrate significant negative associations between our surrogate measures of tumor glycolysis (GlyScore) and immune infiltration (ImmScore) across multiple tumor types. Given the potential role of tumor glycolysis in promoting resistance to immunotherapy (114, 118), targeting tumor metabolism in combination with immunotherapy should be explored further. An inhibitor of the lactate transporter MCT1 (AZD3965) has entered phase I clinical trials, and shows safety and on-target effects, as measured by changes in urinary lactate (119). The question remains as to whether inhibiting tumor glycolysis (or lactate transport) in combination with immunotherapy will increase the response to immunotherapy in patients. The answer to this question remains to be determined.

BIBLIOGRAPHY

1. Postow MA, Chesney J, Pavlick AC, Robert C, Grossmann K, McDermott D, et al. Nivolumab and Ipilimumab versus Ipilimumab in Untreated Melanoma. New England Journal of Medicine. 2015;372:2006-17.
2. Joffre OP, Segura E, Savina A, Amigorena S. Cross-presentation by dendritic cells. Nat Rev Immunol. 2012;12:557-69.
3. Fehres CM, Unger WWJ, Garcia-Vallejo JJ, van Kooyk Y. Understanding the Biology of Antigen Cross-Presentation for the Design of Vaccines Against Cancer. Frontiers in Immunology. 2014;5:149.
4. Hadrup S, Donia M, Thor Straten P. Effector CD4 and CD8 T cells and their role in the tumor microenvironment. Cancer microenvironment : official journal of the International Cancer Microenvironment Society. 2013;6:123-33.
5. Zhang Y, Schreiber TH, Rosenblatt JD. The Role of B Cells in Shaping the Antitumor Immune Response. In: Rosenblatt JD, Podack ER, Barber GN, Ochoa A, editors. Advances in Tumor Immunology and Immunotherapy. New York, NY: Springer New York; 2014. p. 19-35.
6. Marcus A, Gowen BG, Thompson TW, Iannello A, Ardolino M, Deng W, et al. Recognition of tumors by the innate immune system and natural killer cells. Advances in immunology. 2014;122:91-128.
7. Kumar V, Patel S, Tcyganov E, Gabrilovich DI. The Nature of Myeloid-Derived Suppressor Cells in the Tumor Microenvironment. Trends in Immunology.37:208-20.
8. Nghiem P, Bhatia S, Lipson EJ, Sharfman WH, Kudchadkar RR, Brohl AS, et al. Durable Tumor Regression and Overall Survival in Patients With Advanced Merkel Cell Carcinoma Receiving Pembrolizumab as First-Line Therapy. Journal of Clinical Oncology.0:JCO.18.01896.
9. Le DT, Durham JN, Smith KN, Wang H, Bartlett BR, Aulakh LK, et al. Mismatch repair deficiency predicts response of solid tumors to PD-1 blockade. Science. 2017;357:409-13.
10. Grothey A, Cutsem EV, Sobrero A, Siena S, Falcone A, Ychou M, et al. Regorafenib monotherapy for previously treated metastatic colorectal cancer (CORRECT): an international, multicentre, randomised, placebo-controlled, phase 3 trial. The Lancet. 2013;381:303-12.
11. Reck M, Rodriguez-Abreu D, Robinson AG, Hui R, Csoszi T, Fulop A, et al. Pembrolizumab versus Chemotherapy for PD-L1-Positive Non-Small-Cell Lung Cancer. The New England journal of medicine. 2016;375:1823-33.
12. Brahmer J, Rodríguez-Abreu D, Robinson A, Hui R, Csőszi T, Fülöp A, et al. OA 17.06 Updated Analysis of KEYNOTE-024: Pembrolizumab vs Platinum-Based Chemotherapy for Advanced NSCLC With PD-L1 TPS ≥50%. Journal of Thoracic Oncology. 2017;12:S1793-S4.
13. Motzer RJ, Tannir NM, McDermott DF, Arén Frontera O, Melichar B, Choueiri TK, et al. Nivolumab plus Ipilimumab versus Sunitinib in Advanced Renal-Cell Carcinoma. New England Journal of Medicine. 2018;378:1277-90.
14. Antonia SJ, López-Martin JA, Bendell J, Ott PA, Taylor M, Eder JP, et al. Nivolumab alone and nivolumab plus ipilimumab in recurrent small-cell lung cancer (CheckMate 032): a multicentre, open-label, phase 1/2 trial. The Lancet Oncology. 2016;17:883-95.
15. Hodi FS, Chiarion-Sileni V, Gonzalez R, Grob J-J, Rutkowski P, Cowey CL, et al. Nivolumab plus ipilimumab or nivolumab alone versus ipilimumab alone in advanced

melanoma (CheckMate 067): 4-year outcomes of a multicentre, randomised, phase 3 trial. The Lancet Oncology. 2018;19:1480-92.
16. Patel PM, Suciu S, Mortier L, Kruit WH, Robert C, Schadendorf D, et al. Extended schedule, escalated dose temozolomide versus dacarbazine in stage IV melanoma: Final results of a randomised phase III study (EORTC 18032). European journal of cancer. 2011;47:1476-83.
17. Chapman PB, Lorigan PC, Dummer R, Sosman JA, Flaherty KT, Chang I, et al. Vemurafenib in patients with BRAFV600 mutation-positive metastatic melanoma: final overall survival results of the randomized BRIM-3 study. Annals of Oncology. 2017;28:2581-7.
18. Borghaei H, Langer CJ, Gadgeel S, Papadimitrakopoulou VA, Patnaik A, Powell SF, et al. 24-Month Overall Survival from KEYNOTE-021 Cohort G: Pemetrexed and Carboplatin with or without Pembrolizumab as First-Line Therapy for Advanced Nonsquamous Non–Small Cell Lung Cancer. Journal of Thoracic Oncology. 2019;14:124-9.
19. Gandhi L, Rodríguez-Abreu D, Gadgeel S, Esteban E, Felip E, De Angelis F, et al. Pembrolizumab plus Chemotherapy in Metastatic Non–Small-Cell Lung Cancer. New England Journal of Medicine. 2018;378:2078-92.
20. Socinski MA, Jotte RM, Cappuzzo F, Orlandi F, Stroyakovskiy D, Nogami N, et al. Atezolizumab for First-Line Treatment of Metastatic Nonsquamous NSCLC. New England Journal of Medicine. 2018;378:2288-301.
21. Horn L, Mansfield AS, Szczęsna A, Havel L, Krzakowski M, Hochmair MJ, et al. First-Line Atezolizumab plus Chemotherapy in Extensive-Stage Small-Cell Lung Cancer. New England Journal of Medicine. 2018;379:2220-9.
22. Jerome KR, Barnd DL, Bendt KM, Boyer CM, Taylor-Papadimitriou J, McKenzie IFC, et al. Cytotoxic T-Lymphocytes Derived from Patients with Breast Adenocarcinoma Recognize an Epitope Present on the Protein Core of a Mucin Molecule Preferentially Expressed by Malignant Cells. Cancer research. 1991;51:2908-16.
23. Beckhove P, Feuerer M, Dolenc M, Schuetz F, Choi C, Sommerfeldt N, et al. Specifically activated memory T cell subsets from cancer patients recognize and reject xenotransplanted autologous tumors. Journal of Clinical Investigation. 2004;114:67-76.
24. Feuerer M, Rocha M, Bai L, Umansky V, Solomayer EF, Bastert G, et al. Enrichment of memory T cells and other profound immunological changes in the bone marrow from untreated breast cancer patients. International journal of cancer Journal international du cancer. 2001;92:96-105.
25. Whitford P, George WD, Campbell AM. Flow cytometric analysis of tumour infiltrating lymphocyte activation and tumour cell MHC Class I and II expression in breast cancer patients. Cancer letters. 1992;61:157-64.
26. Mensdorff-Pouilly Sv, Verstraeten AA, Kenemans P, Snijdewint FGM, Kok A, Kamp GJV, et al. Survival in Early Breast Cancer Patients Is Favorably Influenced by a Natural Humoral Immune Response to Polymorphic Epithelial Mucin. Journal of Clinical Oncology. 2000;18:574-.
27. Fremd C, Stefanovic S, Beckhove P, Pritsch M, Lim H, Wallwiener M, et al. Mucin 1-specific B cell immune responses and their impact on overall survival in breast cancer patients. Oncoimmunology. 2016;5:e1057387.
28. Goodell V, Waisman J, Salazar LG, dela Rosa C, Link J, Coveler AL, et al. Level of HER-2/neu protein expression in breast cancer may affect the development of endogenous HER-2/neu-specific immunity. Molecular cancer therapeutics. 2008;7:449-54.

29. Tabuchi Y, Shimoda M, Kagara N, Naoi Y, Tanei T, Shimomura A, et al. Protective effect of naturally occurring anti-HER2 autoantibodies on breast cancer. Breast Cancer Res Treat. 2016;157:55-63.
30. Sistrunk WE, MacCarty WC. LIFE EXPECTANCY FOLLOWING RADICAL AMPUTATION FOR CARCINOMA OF THE BREAST: A CLINICAL AND PATHOLOGIC STUDY OF 218 CASES. Annals of Surgery. 1922;75:61-9.
31. Naito Y, Saito K, Shiiba K, Ohuchi A, Saigenji K, Nagura H, et al. CD8⁺ T Cells Infiltrated within Cancer Cell Nests as a Prognostic Factor in Human Colorectal Cancer. Cancer research. 1998;58:3491-4.
32. Denkert C, Loibl S, Noske A, Roller M, Muller BM, Komor M. Tumor-associated lymphocytes as an independent predictor of response to neoadjuvant chemotherapy in breast cancer. Journal of clinical oncology : official journal of the American Society of Clinical Oncology. 2010;28.
33. Ono M, Tsuda H, Shimizu C, Yamamoto S, Shibata T, Yamamoto H, et al. Tumor-infiltrating lymphocytes are correlated with response to neoadjuvant chemotherapy in triple-negative breast cancer. Breast Cancer Res Treat. 2012;132.
34. Mao Y, Qu Q, Zhang Y, Liu J, Chen X, Shen K. The Value of Tumor Infiltrating Lymphocytes (TILs) for Predicting Response to Neoadjuvant Chemotherapy in Breast Cancer: A Systematic Review and Meta-Analysis. PloS one. 2014;9:e115103.
35. Adams S, Gray RJ, Demaria S, Goldstein LJ, Perez EA, Shulman LN. Prognostic Value of Tumor-Infiltrating Lymphocytes (TILs) in Triple Negative Breast Cancers (TNBC) from two Phase III Randomized Adjuvant Breast Cancer Trials: ECOG 2197 and ECOG 1199. Journal of clinical oncology : official journal of the American Society of Clinical Oncology. 2014;32.
36. Loi S, Sirtaine N, Piette F, Salgado R, Viale G, Eenoo FV, et al. Prognostic and Predictive Value of Tumor-Infiltrating Lymphocytes in a Phase III Randomized Adjuvant Breast Cancer Trial in Node-Positive Breast Cancer Comparing the Addition of Docetaxel to Doxorubicin With Doxorubicin-Based Chemotherapy: BIG 02-98. Journal of Clinical Oncology. 2013;31:860-7.
37. Patel SP, Kurzrock R. PD-L1 Expression as a Predictive Biomarker in Cancer Immunotherapy. Molecular cancer therapeutics. 2015;14:847-56.
38. Vonderheide RH, LoRusso PM, Khalil M, Gartner EM, Khaira D, Soulieres D, et al. Tremelimumab in combination with exemestane in patients with advanced breast cancer and treatment-associated modulation of inducible costimulator expression on patient T cells. Clinical cancer research : an official journal of the American Association for Cancer Research. 2010;16:3485-94.
39. Rugo H, Delord J-P, Im S-A, Ott P, Piha-Paul S, Bedard P, et al. Abstract S5-07: Preliminary efficacy and safety of pembrolizumab (MK-3475) in patients with PD-L1–positive, estrogen receptor-positive (ER+)/HER2-negative advanced breast cancer enrolled in KEYNOTE-028. Cancer research. 2016;76:S5-07-S5-.
40. Nanda R, Chow LQM, Dees EC, Berger R, Gupta S, Geva R, et al. Pembrolizumab in Patients With Advanced Triple-Negative Breast Cancer: Phase Ib KEYNOTE-012 Study. Journal of Clinical Oncology. 2016;34:2460-7.
41. Emens LA, Braiteh FS, Cassier P, DeLord J-P, Eder JP, Shen X, et al. Abstract PD1-6: Inhibition of PD-L1 by MPDL3280A leads to clinical activity in patients with metastatic triple-negative breast cancer. Cancer research. 2015;75:PD1-6-PD1-6.
42. Vonderheide RH, LoRusso PM, Khalil M, Gartner EM, Khaira D, Soulieres D, et al. Tremelimumab in Combination with Exemestane in Patients with Advanced Breast Cancer and Treatment-Associated Modulation of Inducible Costimulator Expression on Patient T Cells. Clinical Cancer Research. 2010;16:3485-94.

43. McArthur HL, Page DB. Immunotherapy for the treatment of breast cancer: checkpoint blockade, cancer vaccines, and future directions in combination immunotherapy. Clin Adv Hematol Oncol. 2016;14:922-33.
44. McArthur HL, Diab A, Page DB, Yuan J, Solomon SB, Sacchini V, et al. A Pilot Study of Preoperative Single-Dose Ipilimumab and/or Cryoablation in Women with Early-Stage Breast Cancer with Comprehensive Immune Profiling. Clinical Cancer Research. 2016;22:5729-37.
45. de la Cruz-Merino L, Chiesa M, Caballero R, Rojo F, Palazón N, Carrasco FH, et al. Chapter One - Breast Cancer Immunology and Immunotherapy: Current Status and Future Perspectives. In: Lorenzo G, editor. International Review of Cell and Molecular Biology: Academic Press; 2017. p. 1-53.
46. Disis ML, Stanton SE. Immunotherapy in breast cancer: An introduction. The Breast.
47. Schmid P, Adams S, Rugo HS, Schneeweiss A, Barrios CH, Iwata H, et al. Atezolizumab and Nab-Paclitaxel in Advanced Triple-Negative Breast Cancer. The New England journal of medicine. 2018;379:2108-21.
48. Ribas A, Wolchok JD. Cancer immunotherapy using checkpoint blockade. Science. 2018;359:1350-5.
49. Tumeh PC, Harview CL, Yearley JH, Shintaku IP, Taylor EJM, Robert L, et al. PD-1 blockade induces responses by inhibiting adaptive immune resistance. Nature. 2014;515:568.
50. Rizvi NA, Hellmann MD, Snyder A, Kvistborg P, Makarov V, Havel JJ, et al. Mutational landscape determines sensitivity to PD-1 blockade in non–small cell lung cancer. Science. 2015;348:124-8.
51. Snyder A, Makarov V, Merghoub T, Yuan J, Zaretsky JM, Desrichard A, et al. Genetic Basis for Clinical Response to CTLA-4 Blockade in Melanoma. New England Journal of Medicine. 2014;371:2189-99.
52. Muenst S, Läubli H, Soysal SD, Zippelius A, Tzankov A, Hoeller S. The immune system and cancer evasion strategies: therapeutic concepts. Journal of Internal Medicine. 2016;279:541-62.
53. Warburg O. The Metabolism of Carcinoma Cells. The Journal of Cancer Research. 1925;9:148-63.
54. Ward PS, Thompson CB. Metabolic reprogramming: a cancer hallmark even warburg did not anticipate. Cancer cell. 2012;21:297-308.
55. Shim H, Dolde C, Lewis BC, Wu C-S, Dang G, Jungmann RA, et al. c-Myc transactivation of LDH-A: Implications for tumor metabolism and growth. Proceedings of the National Academy of Sciences. 1997;94:6658-63.
56. Dang CV. MYC, Metabolism, Cell Growth, and Tumorigenesis. Cold Spring Harbor Perspectives in Medicine. 2013;3:a014217.
57. Saltiel AR, Kahn CR. Insulin signalling and the regulation of glucose and lipid metabolism. Nature. 2001;414:799-806.
58. Elstrom RL, Bauer DE, Buzzai M, Karnauskas R, Harris MH, Plas DR, et al. Akt Stimulates Aerobic Glycolysis in Cancer Cells. Cancer research. 2004;64:3892-9.
59. Zeigerer A, McBrayer MK, McGraw TE. Insulin Stimulation of GLUT4 Exocytosis, but Not Its Inhibition of Endocytosis, Is Dependent on RabGAP AS160. Molecular Biology of the Cell. 2004;15:4406-15.
60. Simons A, Orcutt K, Madsen J, Scarbrough P, Spitz D. The Role of Akt Pathway Signaling in Glucose Metabolism and Metabolic Oxidative Stress. In: Spitz DR, Dornfeld KJ, Krishnan K, Gius D, editors. Oxidative Stress in Cancer Biology and Therapy: Humana Press; 2012. p. 21-46.

61. Matoba S, Kang J-G, Patino WD, Wragg A, Boehm M, Gavrilova O, et al. p53 Regulates Mitochondrial Respiration. Science. 2006;312:1650-3.
62. Bensaad K, Tsuruta A, Selak MA, Vidal MN, Nakano K, Bartrons R, et al. TIGAR, a p53-inducible regulator of glycolysis and apoptosis. Cell. 2006;126:107-20.
63. Hall A, Meyle KD, Lange MK, Klima M, Sanderhoff M, Dahl C, et al. Dysfunctional oxidative phosphorylation makes malignant melanoma cells addicted to glycolysis driven by the (V600E)BRAF oncogene. Oncotarget. 2013;4:584-99.
64. Brahimi-Horn MC, Pouysségur J. HIF at a glance. Journal of cell science. 2009;122:1055-7.
65. Soga T. Cancer metabolism: Key players in metabolic reprogramming. Cancer Science. 2013;104:275-81.
66. Yang N, Liu C, Peck AR, Girondo MA, Yanac AF, Tran TH, et al. Prolactin-Stat5 signaling in breast cancer is potently disrupted by acidosis within the tumor microenvironment. Breast Cancer Research. 2013;15:R73.
67. Wike-Hooley JL, van den Berg AP, van der Zee J, Reinhold HS. Human tumour pH and its variation. European Journal of Cancer and Clinical Oncology. 1985;21:785-91.
68. Ziebart T, Walenta S, Kunkel M, Reichert TE, Wagner W, Mueller-Klieser W. Metabolic and proteomic differentials in head and neck squamous cell carcinomas and normal gingival tissue. Journal of cancer research and clinical oncology. 2011;137:193-9.
69. Brizel DM, Schroeder T, Scher RL, Walenta S, Clough RW, Dewhirst MW, et al. Elevated tumor lactate concentrations predict for an increased risk of metastases in head-and-neck cancer. International journal of radiation oncology, biology, physics. 2001;51:349-53.
70. Walenta S, Wetterling M, Lehrke M, Schwickert G, Sundfor K, Rofstad EK, et al. High lactate levels predict likelihood of metastases, tumor recurrence, and restricted patient survival in human cervical cancers. Cancer research. 2000;60:916-21.
71. Saraswathy S, Crawford FW, Lamborn KR, Pirzkall A, Chang S, Cha S, et al. Evaluation of MR markers that predict survival in patients with newly diagnosed GBM prior to adjuvant therapy. Journal of Neuro-Oncology. 2009;91:69-81.
72. Végran F, Boidot R, Michiels C, Sonveaux P, Feron O. Lactate Influx through the Endothelial Cell Monocarboxylate Transporter MCT1 Supports an NF-κB/IL-8 Pathway that Drives Tumor Angiogenesis. Cancer research. 2011;71:2550-60.
73. Porporato PE, Payen VL, De Saedeleer CJ, Preat V, Thissen JP, Feron O, et al. Lactate stimulates angiogenesis and accelerates the healing of superficial and ischemic wounds in mice. Angiogenesis. 2012;15:581-92.
74. Goetze K, Walenta S, Ksiazkiewicz M, Kunz-Schughart LA, Mueller-Klieser W. Lactate enhances motility of tumor cells and inhibits monocyte migration and cytokine release. Int J Oncol. 2011;39:453-63.
75. Migneco G, Whitaker-Menezes D, Chiavarina B, Castello-Cros R, Pavlides S, Pestell RG, et al. Glycolytic cancer associated fibroblasts promote breast cancer tumor growth, without a measurable increase in angiogenesis: evidence for stromal-epithelial metabolic coupling. Cell cycle. 2010;9:2412-22.
76. Pavlides S, Whitaker-Menezes D, Castello-Cros R, Flomenberg N, Witkiewicz AK, Frank PG, et al. The reverse Warburg effect: aerobic glycolysis in cancer associated fibroblasts and the tumor stroma. Cell cycle. 2009;8:3984-4001.
77. Buck MD, Sowell RT, Kaech SM, Pearce EL. Metabolic Instruction of Immunity. Cell.169:570-86.
78. Marchiq I, Pouyssegur J. Hypoxia, cancer metabolism and the therapeutic benefit of targeting lactate/H(+) symporters. Journal of molecular medicine. 2016;94:155-71.

79. Dietl K, Renner K, Dettmer K, Timischl B, Eberhart K, Dorn C, et al. Lactic Acid and Acidification Inhibit TNF Secretion and Glycolysis of Human Monocytes. The Journal of Immunology. 2010;184:1200-9.
80. Puig-Kroger A, Pello OM, Selgas R, Criado G, Bajo MA, Sanchez-Tomero JA, et al. Peritoneal dialysis solutions inhibit the differentiation and maturation of human monocyte-derived dendritic cells: effect of lactate and glucose-degradation products. J Leukoc Biol. 2003;73:482-92.
81. Gottfried E, Kunz-Schughart LA, Ebner S, Mueller-Klieser W, Hoves S, Andreesen R, et al. Tumor-derived lactic acid modulates dendritic cell activation and antigen expression. Blood. 2006;107:2013-21.
82. Markowitz J, Wesolowski R, Papenfuss T, Brooks TR, Carson WE. Myeloid-derived suppressor cells in breast cancer. Breast Cancer Res Treat. 2013;140:13-21.
83. Husain Z, Huang Y, Seth P, Sukhatme VP. Tumor-derived lactate modifies antitumor immune response: effect on myeloid-derived suppressor cells and NK cells. J Immunol. 2013;191:1486-95.
84. Colegio OR, Chu NQ, Szabo AL, Chu T, Rhebergen AM, Jairam V, et al. Functional polarization of tumour-associated macrophages by tumour-derived lactic acid. Nature. 2014;513:559-63.
85. Brand A, Singer K, Koehl GE, Kolitzus M, Schoenhammer G, Thiel A, et al. LDHA-Associated Lactic Acid Production Blunts Tumor Immunosurveillance by T and NK Cells. Cell metabolism. 2016;24:657-71.
86. Fischer K, Hoffmann P, Voelkl S, Meidenbauer N, Ammer J, Edinger M, et al. Inhibitory effect of tumor cell–derived lactic acid on human T cells; 2007.
87. Mendler AN, Hu B, Prinz PU, Kreutz M, Gottfried E, Noessner E. Tumor lactic acidosis suppresses CTL function by inhibition of p38 and JNK/c-Jun activation. International Journal of Cancer. 2012;131:633-40.
88. Haas R, Smith J, Rocher-Ros V, Nadkarni S, Montero-Melendez T, D'Acquisto F, et al. Lactate Regulates Metabolic and Pro-inflammatory Circuits in Control of T Cell Migration and Effector Functions. PLoS biology. 2015;13:e1002202.
89. Diem S, Kasenda B, Spain L, Martin-Liberal J, Marconcini R, Gore M, et al. Serum lactate dehydrogenase as an early marker for outcome in patients treated with anti-PD-1 therapy in metastatic melanoma. British Journal of Cancer. 2016;114:256-61.
90. Chang CH, Qiu J, O'Sullivan D, Buck MD, Noguchi T, Curtis JD, et al. Metabolic Competition in the Tumor Microenvironment Is a Driver of Cancer Progression. Cell. 2015;162:1229-41.
91. Ho PC, Bihuniak JD, Macintyre AN, Staron M, Liu X, Amezquita R, et al. Phosphoenolpyruvate Is a Metabolic Checkpoint of Anti-tumor T Cell Responses. Cell. 2015;162:1217-28.
92. Keating ST, El-Osta A. Epigenetics and Metabolism. Circulation Research. 2015;116:715-36.
93. Wong CC, Qian Y, Yu J. Interplay between epigenetics and metabolism in oncogenesis: mechanisms and therapeutic approaches. Oncogene. 2017.
94. Aslakson C, Miller F. Selective events in the metastatic process defined by analysis of the sequential dissemination of subpopulations of a mouse mammary tumor. Cancer research. 1992;52:1399 - 405.
95. Serganova I, Cohen IJ, Vemuri K, Shindo M, Maeda M, Mane M, et al. LDH-A regulates the tumor microenvironment via HIF-signaling and modulates the immune response. PloS one. 2018;13:e0203965.
96. Serganova I, Moroz E, Cohen I, Moroz M, Mane M, Zurita J, et al. Enhancement of PSMA-Directed CAR Adoptive Immunotherapy by PD-1/PD-L1 Blockade. Molecular Therapy - Oncolytics. 2017;4:41-54.

97. Rooney Michael S, Shukla Sachet A, Wu Catherine J, Getz G, Hacohen N. Molecular and Genetic Properties of Tumors Associated with Local Immune Cytolytic Activity. Cell. 2015;160:48-61.
98. Lehmann BD, Jovanović B, Chen X, Estrada MV, Johnson KN, Shyr Y, et al. Refinement of Triple-Negative Breast Cancer Molecular Subtypes: Implications for Neoadjuvant Chemotherapy Selection. PloS one. 2016;11:e0157368.
99. Elston CW, Ellis IO. Pathological prognostic factors in breast cancer. I. The value of histological grade in breast cancer: experience from a large study with long-term follow-up. Histopathology. 1991;19:403-10.
100. Hammond ME, Hayes DF, Dowsett M, Allred DC, Hagerty KL, Badve S, et al. American Society of Clinical Oncology/College Of American Pathologists guideline recommendations for immunohistochemical testing of estrogen and progesterone receptors in breast cancer. Journal of clinical oncology : official journal of the American Society of Clinical Oncology. 2010;28:2784-95.
101. Wolff AC, Hammond MEH, Allison KH, Harvey BE, Mangu PB, Bartlett JMS, et al. Human Epidermal Growth Factor Receptor 2 Testing in Breast Cancer: American Society of Clinical Oncology/College of American Pathologists Clinical Practice Guideline Focused Update. Journal of clinical oncology : official journal of the American Society of Clinical Oncology. 2018;36:2105-22.
102. Salgado R, Denkert C, Demaria S, Sirtaine N, Klauschen F, Pruneri G, et al. The evaluation of tumor-infiltrating lymphocytes (TILs) in breast cancer: recommendations by an International TILs Working Group 2014. Ann Oncol. 2015;26:259-71.
103. Rizwan A, Serganova I, Khanin R, Karabeber H, Ni X, Thakur S, et al. Relationships between LDH-A, lactate, and metastases in 4T1 breast tumors. Clinical cancer research : an official journal of the American Association for Cancer Research. 2013;19:5158-69.
104. Colegio OR, Chu N-Q, Szabo AL, Chu T, Rhebergen AM, Jairam V, et al. Functional polarization of tumour-associated macrophages by tumour-derived lactic acid. Nature. 2014;513:559-63.
105. Lim SO, Li CW, Xia W, Lee HH, Chang SS, Shen J, et al. EGFR Signaling Enhances Aerobic Glycolysis in Triple-Negative Breast Cancer Cells to Promote Tumor Growth and Immune Escape. Cancer research. 2016;76:1284-96.
106. Zhang C-S, Hawley SA, Zong Y, Li M, Wang Z, Gray A, et al. Fructose-1,6-bisphosphate and aldolase mediate glucose sensing by AMPK. Nature. 2017;548:112.
107. Lee MN, Ha SH, Kim J, Koh A, Lee CS, Kim JH, et al. Glycolytic flux signals to mTOR through glyceraldehyde-3-phosphate dehydrogenase-mediated regulation of Rheb. Molecular and cellular biology. 2009;29:3991-4001.
108. Chang C-H, Curtis Jonathan D, Maggi Leonard B, Faubert B, Villarino Alejandro V, O'Sullivan D, et al. Posttranscriptional Control of T Cell Effector Function by Aerobic Glycolysis. Cell. 2013;153:1239-51.
109. Ho PC, Bihuniak JD, Macintyre AN, Staron M, Liu X, Amezquita R. Phosphoenolpyruvate Is a Metabolic Checkpoint of Anti-tumor T Cell Responses. Cell. 2015;162.
110. Angelin A, Gil-de-Gómez L, Dahiya S, Jiao J, Guo L, Levine MH, et al. Foxp3 Reprograms T Cell Metabolism to Function in Low-Glucose, High-Lactate Environments. Cell metabolism. 2017;25:1282-93.e7.
111. Boukouris AE, Zervopoulos SD, Michelakis ED. Metabolic Enzymes Moonlighting in the Nucleus: Metabolic Regulation of Gene Transcription. Trends in biochemical sciences. 2016;41:712-30.
112. Wang Y-P, Lei Q-Y. Metabolite sensing and signaling in cell metabolism. Signal Transduction and Targeted Therapy. 2018;3:30.

113. Garcia-Aguilar A, Martinez-Reyes I, Cuezva JM. Changes in the Turnover of the Cellular Proteome during Metabolic Reprogramming: A Role for mtROS in Proteostasis. Journal of proteome research. 2019;18:3142-55.
114. Cascone T, McKenzie JA, Mbofung RM, Punt S, Wang Z, Xu C, et al. Increased Tumor Glycolysis Characterizes Immune Resistance to Adoptive T Cell Therapy. Cell metabolism. 2018;27:977-87.e4.
115. Danaher P, Warren S, Lu R, Samayoa J, Sullivan A, Pekker I, et al. Pan-cancer adaptive immune resistance as defined by the Tumor Inflammation Signature (TIS): results from The Cancer Genome Atlas (TCGA). Journal for ImmunoTherapy of Cancer. 2018;6:63.
116. Calabrò A, Beissbarth T, Kuner R, Stojanov M, Benner A, Asslaber M, et al. Effects of infiltrating lymphocytes and estrogen receptor on gene expression and prognosis in breast cancer. Breast Cancer Res Treat. 2009;116:69-77.
117. Thorsson V, Gibbs DL, Brown SD, Wolf D, Bortone DS, Ou Yang T-H, et al. The Immune Landscape of Cancer. Immunity. 2018;48:812-30.e14.
118. Huang L, Malu S, McKenzie JA, Andrews MC, Talukder AH, Tieu T, et al. The RNA-binding Protein MEX3B Mediates Resistance to Cancer Immunotherapy by Downregulating HLA-A Expression. Clinical Cancer Research. 2018;24:3366-76.
119. Halford SER, Jones P, Wedge S, Hirschberg S, Katugampola S, Veal G, et al. A first-in-human first-in-class (FIC) trial of the monocarboxylate transporter 1 (MCT1) inhibitor AZD3965 in patients with advanced solid tumours. Journal of Clinical Oncology. 2017;35:2516-.